Metals and Materials International (2021) 27:1–39
https://doi.org/10.1007/s12540-020-00931-2

Heterogeneous Aspects of Additive Manufactured Metallic Parts: A Review

G. M. Karthik[1] · Hyoung Seop Kim[2]

Received: 7 October 2020 / Accepted: 16 November 2020 / Published online: 2 January 2021

Abstract
Metal additive manufacturing (MAM) is an emerging technology to produce complex end-use metallic parts. To adopt MAM for manufacturing numerous engineering parts used in critical applications, a thorough understanding of the relationship between the complex thermal cycles in MAM and the unique heterogeneous microstructures of MAM parts need to be established. This review article provides a comprehensive overview of the evolution of heterogeneous microstructures in MAM parts, including melt pool boundaries, heterogeneous grain structure, sub-grain cellular structure, matrix supersaturation, segregation, phase transformation, oxides formation, and texture. The evolution of residual stresses and the anisotropy in MAM parts and the post-MAM heat treatment effects on the microstructural evolution are also discussed. This review covers the microstructural aspects of most engineering materials in particular steels, high entropy alloys, aluminum alloys, titanium alloys, nickel-base superalloys, and copper alloys, with a primary focus on the parts manufactured using selective laser melting, direct energy deposition, and electron beam melting processes.

Keywords Metal additive manufacturing · Selective laser melting · Direct energy deposition · Electron beam melting · Microstructure · Heat treatment

1 Introduction

According to ISO/ASTM 52900:2015, additive manufacturing (AM) is described as the manufacturing process where the material is deposited or fused layer-by-layer until a net- or near-net-shape part is achieved [1]. The first AM processes are limited to the rapid manufacturing of prototypes, and with the advancement of technology, parts with improved quality and reliability are realized. Today, AM has transformed more into a rapid manufacturing process capable of manufacturing complex end-use metallic parts. The metal additive manufacturing (MAM) technology has revolutionized how the metallic parts are designed and manufactured in the digital industrial era [2]. A few examples include fuel injectors in a LEAP turbine engine [3], γ-TiAl turbine blades in the GEnX engine [4], landing gear parts, tool inserts with conformal cooling channels [5], and medical implants such as dental prosthesis and bone replacements for jaws and hips [6].

Many studies establish the benefits of MAM technology over conventional manufacturing processes. The microstructures, mechanical and functional properties, and the printability of several metals and alloys have been extensively studied [7–9]. The distinct thermal cycles due to the layer-by-layer and track-by-track part fabrication, the high-temperature gradients, and rapid cooling rates associated with the MAM processes create unique microstructures in the manufactured parts. Deeper insights into the mechanisms of microstructure evolution would enable us to take full advantage of the microstructures possible with MAM.

The current review article focuses on establishing the different microstructural aspects of MAM parts produced with various engineering materials. Further, the influence of the typical processing conditions on the microstructural evolution and the role of these microstructures on the mechanical properties are presented. The effect of post-deposition heat treatment on the microstructures is also covered.

✉ Hyoung Seop Kim
hskim@postech.ac.kr

[1] Department of Materials Science and Engineering, Pohang University of Science and Technology (POSTECH), Pohang 37673, Republic of Korea

[2] Graduate Institute of Ferrous Technology, Pohang University of Science and Technology (POSTECH), Pohang 37673, Republic of Korea

The classification of MAM processes is shown in Fig. 1. Among numerous MAM processes developed so far, selective laser melting (SLM), powder-fed direct energy deposition (DED), and electron beam melting (EBM) processes are the most widely used techniques for MAM part fabrication. In particular, this review focuses on the microstructural aspects of the parts produced with these fusion-based metal MAM processes. Therefore, unless explicitly specified, the term MAM refers to the parts produced with DED, SLM, and EBM processes.

2 MAM Processes

2.1 Direct Energy Deposition (DED)

DED covers all the processes in which the melt pool is created by an energy source (laser, arc, and electron beam), and the feedstock (powder or wire) is fed into the melt pool. Laser heat source with powder feedstock is the widely used process, developed in the 1980s at Sandia National Laboratories and originally patented as the LENS process [17, 18]. In the LENS process, the parts are built on a substrate fixed on a machine bed having a 3- or a 5-axis motion. Pure elemental or alloy powders are filled in separate hoppers, and the powder feeding rate from the hopper is precisely controlled. The laser creates a melt pool, and the powders are fed into the melt pool co-axially with the aid of carrier gas (Ar). The build chamber is filled with inert gas (Ar) or maintained under a low vacuum during the processing of reactive materials such as Ti. No special atmosphere is maintained during the processing of non-reactive materials because the carrier gas Ar itself covers the molten pool and prevent any oxidation. After depositing a track, a new track is deposited on the side with an overlap with the previous track for realizing good inter-track. Similarly, while depositing a new layer on the top, the previously deposited layer is remelted by some amount for achieving good inter-layer bonding (Fig. 2a). The spacing between the individual tracks is known as hatch-spacing, and the height of each deposited layer is known as layer thickness. The process is repeated until an aimed near net-shaped part is realized [10, 14].

A layer height of ~ 250 µm and the deposition rate of ~ 230 cm^3/h are typically achieved during DED. Compared the DED to the SLM process, the feedstock powder particle size is relatively coarse (60–150 µm) to facilitate the smoother flow of the powder. Thus the resulting melt pool size is relatively bigger, and the parts are typically near-net shape with a relatively rough surface finish. After part fabrication, post-processing steps involving removal of the loose powders and supporting structures, finish machining, and post-deposition heat treatment, are carried out based on the specific requirement. The most significant advantage of the DED process over SLM and EBM processes is that it can produce functionally graded parts, multi-material parts. Also, in situ tailoring of the alloy composition and the repair of worn-out parts is facilitated with DED [14, 19, 20].

2.2 Selective Laser Melting (SLM)

The first powder-bed fusion (PBF) process is selective laser sintering (SLS) developed by the DTM Corporation, USA,

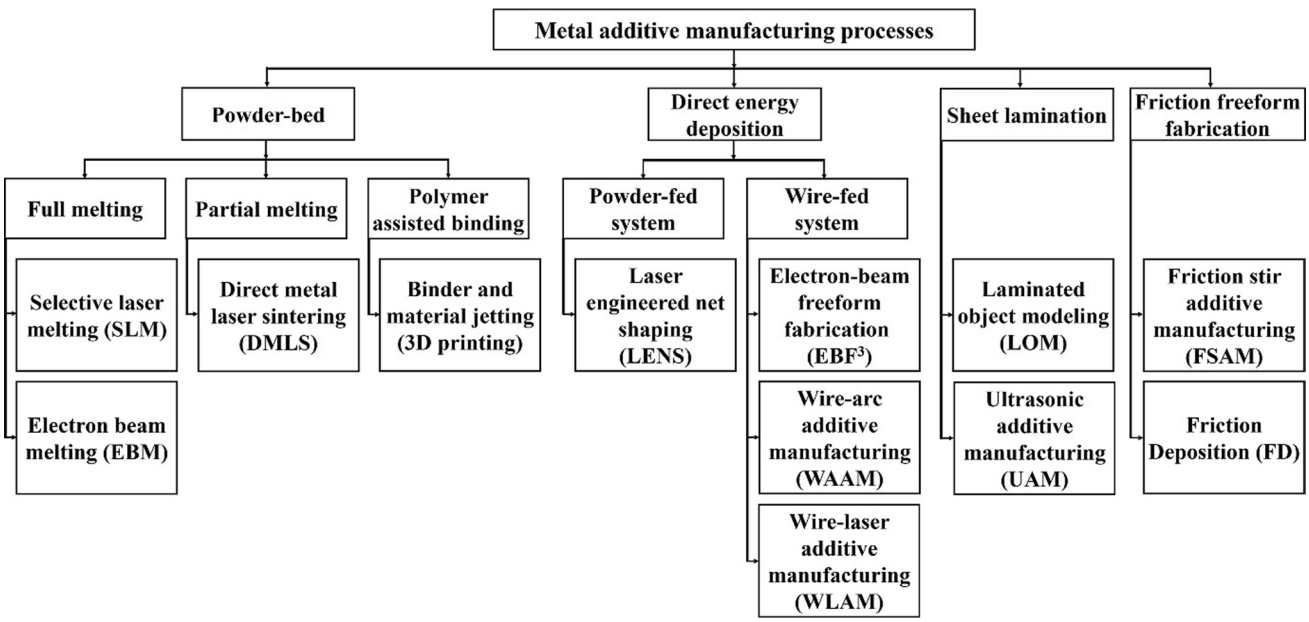

Fig. 1 Classification of metal additive manufacturing processes [8, 10–16]. Reproduced with permission from Elsevier

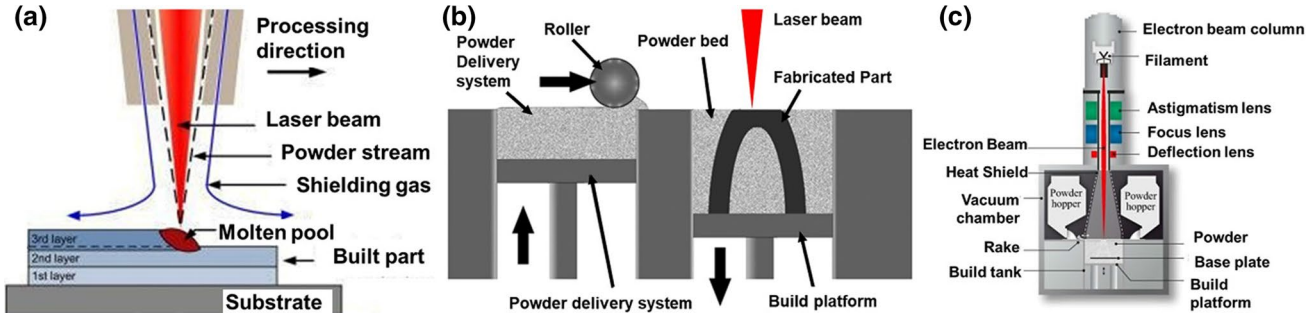

Fig. 2 Schematic illustrations of **a** DED [24], **b** SLM [25], and **c** EBM [26] processes. Reproduced with permission from John Wiley and Sons, and Elsevier

in 1992 [21]. SLS involves part fabrication by partial melting of the powder followed by sintering at high temperatures in a furnace. The process is best suited for ceramics and porous structures. For dense metal parts, complete melting is preferred over the sintering of the powders, and technologies involving the complete melting of the powder are developed in the early 2000s. The process is called selective laser melting (SLM). The SLM process takes place in an enclosed chamber filled with inert gas (Ar, N_2). The oxygen content inside the build chamber is maintained to be below ~ 1–2 wt%. Pre-alloyed powders with a size range of 20–40 µm were used as a feedstock. The feedstock powder is filled in a powder dispenser present inside the build chamber. The base plate is fixed to the build platform, and a thin layer of the powder matching the layer thickness is precisely spread on the substrate using a roller. The typical layer height in SLM is ~ 10–50 µm. A finely focused laser beam with a diameter of ~ 0.13 mm melts the powder selectively on the powder-bed as per the slice couture.

After depositing a layer, the build platform is lowered by layer height, and the powder carrying dispenser is raised by layer height. Subsequently, the roller spreads the powder uniformly, and the focused laser beam selectively melts the powder. These steps of powder spreading and laser melting are repeated until a final part is realized, as shown in Fig. 2b. Similar to the DED processes, for achieving good inter-track and inter-layer bonding, some remelting of the previous track or layer is ensured. The typical deposition rates achieved during SLM part fabrication is ~ 5–20 cm^3/h. The surface finish of the SLM parts is much finer than the DED and EBM processed parts because of the small layer height and less powder sintering adjacent to the part. After the part is built, the loose powder surrounding the part is removed, and the parts are subjected to post-processing based on application requirements [14, 22, 23].

2.3 Electron Beam Melting (EBM)

EBM is also classified as a PBF process, similar to the SLM process (Fig. 2c). The major difference between these processes is the energy source used and the respective hardware. In the EBM process, a high energy electron gun is used as an energy source, and the process takes place in a vacuum. During EBM, a typical layer thickness of ~ 50 µm, deposition rates of ~ 60 cm^3/h, beam diameter ~ 0.2–0.3 mm, and powders of the size range of ~ 40–120 µm are used. The processing steps are very similar to those of the SLM process. However, in EBM, a preheating run precedes the actual melting run [10, 14].

The primary purpose of the preheating run in EBM is to improve the beam-matter interaction efficiency and achieve sintering between the individual powder granules. When a high power electron beam falls on the powder-bed, the thin oxide film on the powder surface acts as an insulator, and the powder granules get charged. Because of this charging, the powder particles repel with each other, commonly referred to as "smoke," which hinders the electron beam and forces the build to stop. To overcome this problem, a preheating run with a defused electron beam before the melting run is carried out for each layer to reduce the charging effect by some powder sintering because of incipient melting. Further, an optimized preheating run would effectively reduce the as-built residual stresses and lower the beam current required for the melting run. However, it would increase the overall build time and also call for an extra post-processing step to remove the sintered powder particles on the sample surface.

3 Heterogeneous Microstructures

In the recent past, there is a lot of interest in developing heterogeneous microstructures in materials because of their unprecedented combination of high strength and ductility

[27]. In traditional strengthening mechanisms, with the increase in the strength, one has to compromise on ductility. However, the heterostructured materials exhibit synergy in strength and ductility because of the generation of back stress during deformation [28].

The microstructures in heterostructured materials are divided into two domains, a soft and a hard domain. During deformation, because of the strain gradient at the interface between the soft and hard domains, geometrically necessary dislocations (GNDs) develop at the domain interface and lead to the generation of back-stress, i.e., higher effective stress is required to generate new dislocations. These back stresses make the soft domain stronger and result in an increase in the global yield strength of the material. Further, the back-stress work hardening effectively delays the necking during tensile loading and improves the ductility of the material. Therefore, the back stresses are the primary reason for the synergy in strength and ductility in heterogeneous microstructures.

During MAM part fabrication, because of the complex thermal cycles, heterogeneous microstructures develop [29, 30], and these heterogeneous microstructures are the reason for the improved strength and ductility in the MAM parts compared to the conventionally processed counterparts. Therefore, a thorough understanding of the evolution of these heterogeneous microstructures in the MAM parts would help develop materials with an excellent combination of high strength and ductility.

4 Microstructures of Fusion-Based MAM Parts

The microstructural aspects of MAM parts are discussed individually in detail in this chapter. The microstructures obtained using various characterization techniques such as optical microscopy, scanning electron microscope (SEM) with both secondary electron (SE) and backscattered electron (BSE) mode, energy-dispersive X-ray spectroscopy (EDS), electron backscatter diffraction (EBSD), transmission electron microscope (TEM) with high resolution (HR), selected area electron diffraction (SAED), and atom probe tomography (APT), are presented wherever it is required.

4.1 Melt Pool

During MAM, the parts are built by depositing several melt pools layer-by-layer (to build the height) and track-by-track (to fill an area). When depositing a new track, overlap with the previous track is maintained, and while depositing a new layer, sufficient penetration with the previous layer is ensured to avoid any lack of fusion defects. The lack of fusion (LF) index expressed as the ratio of melt pool depth to the layer thickness was used to ensure adequate fusion and interlayer bonding [31]. LF > 1 ensures a larger melt pool with sufficient penetration with the previous layer. LF index of ~ 1.15 was shown to result in full density (over 99.9% relative density) in DED processed Ti–6Al–4: i.e., ~ 15% penetration with the previous layer signifies good interlayer bonding [32]. Most recently, Johnson et al. [33] proposed a methodology for predicting the printability of alloys with melt pool geometry-based criteria. The melt pool dimensions, length (L), width (W), depth (D), and powder layer thickness (t), were used to define the process parameter space. The criteria for balling, which causes instabilities in melt pools, is given as $L/W > 2.3$. The criteria for keyhole formation and the lack of fusion defects are given as $W/D < 1.5$ and $D/t < 1.5$, respectively.

It is important to note that the melt pool shape not only depends on the MAM processing condition, but also depends on the thermo-physical properties of the material. In identical MAM processing conditions, different alloys can present different melt pool depths based on their thermo-physical properties. Therefore, the ideal processing conditions can vary for different alloys and need to be individually optimized.

The melt pool can be divided into three regions (1) core of the melt pool, (2) melt pool boundary (MPB), and (3) heat-affected zone (HAZ).

The MPBs are identified as two types, as shown in Fig. 3 [34]. The boundaries that exist between layers are called as inter-layer or layer-layer MPBs. The boundaries that are present between tracks are called as inter-track or track-track MPBs. The primary difference between these two boundaries is the grain orientation. The inter-layer MPBs have the same grain orientation on both sides because of the epitaxial growth of grains from the previously deposited layer. However, the grain orientations on both sides of the inter-track MPBs are significantly different. The intersection region of both these boundaries caused a sharp angle. The layer-layer MPBs with continuous or similar grain orientation on both sides are shown to have more uniform force distribution than the track-track MPBs with different orientations [35].

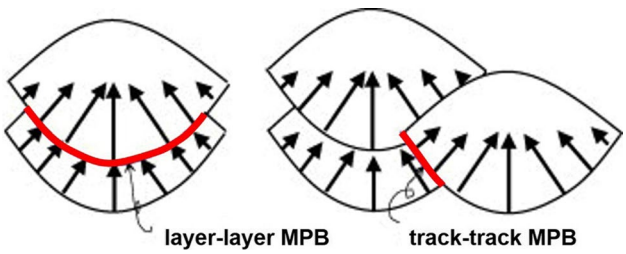

Fig. 3 Two types of MPBs in the fusion-based MAM parts [34]. Reproduced with permission from Elsevier

The microstructures close to the MPBs are quite different compared to those of the core of the melt pool because it contains the re-melted and re-heated regions of the previous layer. In some aluminum alloys, Al–11.28Si [36] and Al–Cu–Mg [37], planar solidification was reported in the re-melted regions close to the MPBs (Fig. 4) because of the high thermal gradients (G) and very low growth rates (R). However, the solidification progresses as columnar into the melt pool because of the rapid cooling rates [38].

Just below the re-melted region, a thin region of the previous layer, called HAZ, is re-heated to high temperatures close to the melting point. Dilip et al. [39] have shown that a thin region adjacent to the MPB is reheated twice during part fabrication. These reheating cycles result in the development of different microstructures in the HAZ regions compared to the bulk of the layer. In the SLM processed Al–12Si alloy [40] and DED processed Al–11.3Si alloy [41], while the bulk of the layer showed fibrous Si particles, partial heat treatment and equiaxed coarse Si particles were reported in the HAZ regions. Grain coarsening was reported in the HAZ regions just below the MPBs in DED processed 316L [42]. In another work, on SLM processed high-strength low alloy steels HY100, tempering of the martensitic structure was reported in the HAZ regions close to the MPBs [43]. In the SLM processed Al–10Si–Mg alloy, an equiaxed grain zone devoid of the cellular sub-structure was reported adjacent to the MPBs. The authors reported that the reheating thermal cycle is enough to recrystallize the columnar grains and promote diffusion, eliminating the cellular substructure [44]. In another work on DED processed high Mn steel X30MnAl23, a microstructure devoid of dendrites and homogeneous composition was reported in the HAZ regions. The high temperatures in the HAZ caused homogenization of the dendritic structure in the previous layer and resulted in a homogeneous elemental distribution [45].

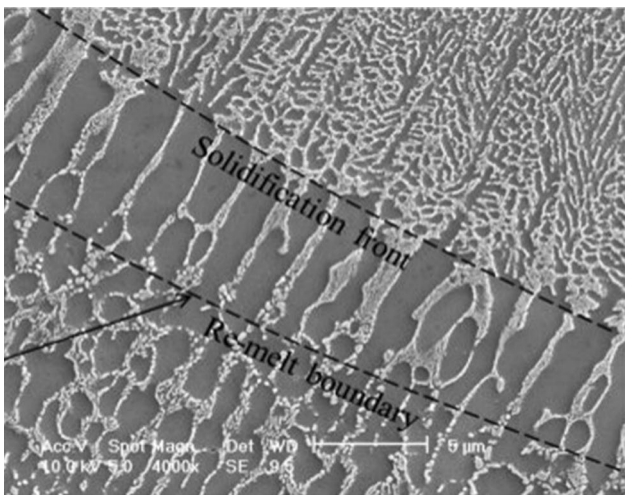

Fig. 4 SEM micrograph of the MPB in the DED processed Al–11.28Si alloy [36]. Reproduced with permission from Elsevier

The rapid cooling rates and higher temperature gradients close to the MPBs cause inhomogeneous solidification and non-uniform solute distribution [46, 47]. In the SLM processed Ti–6Al–4V, segregation of Al to the MPBs was reported [46], and it led to preferential precipitation of the intermetallic Ti_3Al phase at the MPBs. In the SLM processed IN718 samples, the non-uniform distribution of Nb was reported with MPBs having lower Nb concentration than the center of the pool [47]. Shifeng et al. [34] reported the depletion of impurity elements C, O, and Si at the MPBs in as-built 316L SLM samples. Zhao et al. [48] reported decarburization at the MPBs of the SLM processed martensitic stainless steel (AISI 420 SS). When a material layer is depositing, the MPB is exposed to the oxygen present in the build chamber, causing decarburization because of the high affinity of C for O at high temperatures. The authors reported carbon depletion ~ 21% at the MPBs compared to the core.

The MPBs have been seen in many alloy systems. However, in specific cases, these MPBs are not clearly revealed because of the masking effect from the subsequent solid-state phase transformation. Brandl et al. [49] studied the microstructures of wire-feed DED Ti–6Al–4V single beads and did not observe the MPBs. The solid-state phase transformation of β to α masks the MPBs. In the EBM processed γ-TiAl alloy Ti–48Al–2Cr–2Nb, while the bulk of the sample revealed the MPBs, the top few layers of the samples did not reveal any MPBs. The high preheat temperatures (~ 1100 °C) above the eutectoid temperature has led to phase transformation of lamellar α + γ formed during solidification to a duplex/near-γ microstructure in the bulk of the sample. This transformation is not complete in the top few layers because they experienced less time above the eutectoid temperature during part building [50].

It is important to note that the size and shape of the melt pool affect the grain orientation and texture in MAM parts [51]. The thermal gradient direction, i.e., grain growth direction, is primarily determined by the shape of the melt pool [52]. During solidification, grains grow epitaxially normal to the MPBs along the heat flow direction. Therefore, the local curvature of the melt pool plays a significant role in determining the grain orientation. In a deep and curved shape melt pool, e.g., in the DED process, the grains grow at an angle to the build direction from the sides because of the local curvature of the melt pool [53]. However, with a shallow and long melt pool, typically in SLM, the grains tend to grow along the build direction [46]. As texture and anisotropy of the parts are related to the grain orientation, the melt pool shape and size also control them [52, 54]. Sun et al. [51] demonstrated an approach to control the crystallographic texture by changing the melt pool shape. Shallow melt pools presented a crystallographic lamellar

microstructure having <110> and <001> textures. On the other hand, deeper melt pools resulted in a single crystalline-like microstructure with <110> texture.

The MPBs are generally considered the weakest regions in the MAM parts because of the presence of inhomogeneous microstructures and defects [34, 44, 55]. Although the defects can be reduced by careful process parameter optimization, de-cohesion of the MPBs at high strain levels is also reported [29, 54]. Shifeng et al. [34] reported that MPBs significantly affect the plastic deformation and fracture mode in 316L SS. It was attributed to the preferential concentration of most processing defects, such as lack of fusion, porosity, oxides, and cracks at the MPBs, as shown in Fig. 5. Xiong et al. [44] reported premature fractures along the MPBs in the as-built AlSi10Mg alloy SLM samples. The authors featured MPBs as the weakest regions in the SLM parts because of the inhomogeneous microstructures at the MPBs. Further, the authors showed the samples with a lower number of MPBs (horizontally build sample) showed higher strength and ductility compared to the samples with higher MPBs (vertically build samples). While it is intuitive to reduce the number of MPBs, the MAM processing conditions are generally optimized considering the complexity of the part geometry, productivity, and stress distribution. Therefore, a trade-off is always maintained.

4.2 Grain Structure

Additive parts experience a distinct thermal cycle due to the layer-by-layer and track-by-track material addition. Besides, the fast and directional cooling during the MAM processes creates unique grain structures in the parts.

The grain structure evolution during MAM can be explained from the solidification theory [57, 58]. The mode of solidification is determined by the thermal gradient (G), and the fineness of the microstructure is dependent on the growth rate (R). G is expressed as the temperature difference over a certain distance (dT/dx), and it varies over time and location inside the melt pool. R is expressed as the product of the speed of moving heat source (v) and cosine of θ, where θ is the angle between the growth direction and the direction of the moving source. The ratio G/R determines the resulting solidification mode: planar, cellular, columnar dendritic, or equiaxed dendritic structure (from high to low ratio). The product of G and R gives the growth rate (the diffusion length); therefore, it determines the fineness of the microstructure: the higher $G*R$, the finer the structure (Fig. 6).

As the heat source is continuously moving, the G and R vary spatially within the melt pool. As a result, the mode of solidification varies within the melt pool. Near the melt pool surface and near the center of the melt pool, fine equiaxed grains (because of low G/R and high $G*R$) form; and close to the MPBs, coarse columnar dendrites (high G/R and low $G*R$) develop**.** R strongly depends on the scan speed and location within the melt pool. At a very high scan speed ~ 1 m/s, such as in the SLM process, because the growth rate of the grains cannot match the scan speed, heterogeneous nucleation occurs closer to the surface of the melt pool and results in equiaxed grains [59, 60]. In an effort to produce single crystal superalloy CMSX-4 using DED, it was shown that the transition from columnar to equiaxed grains takes place only under certain solidification

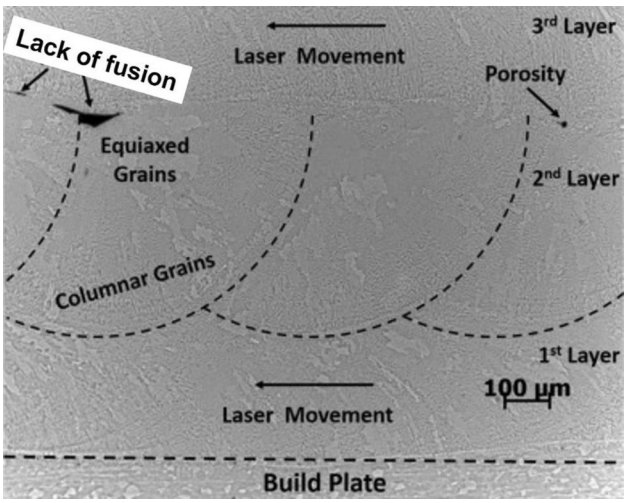

Fig. 5 SEM micrograph showing the preferential presence of processing defects at the melt pool boundaries in the DED processed 316L SS [56]. Reproduced with permission from Elsevier

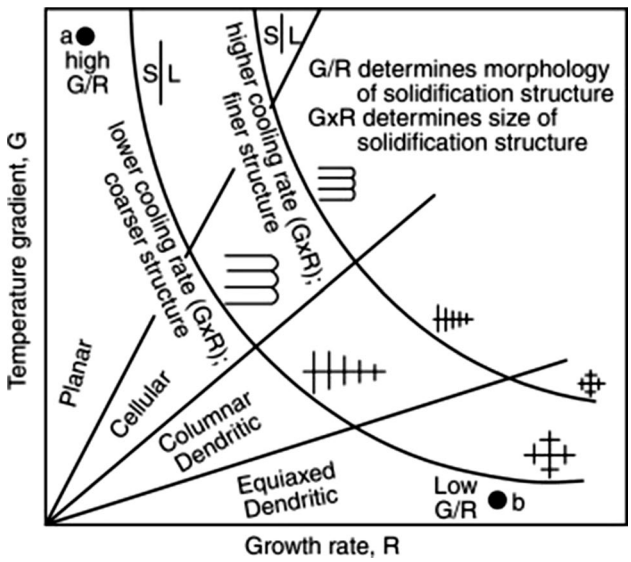

Fig. 6 Effects of growth rate (R) and temperature gradient (G) on the size and morphology of the solidification microstructure [54, 57]. Reproduced with permission from Elsevier

conditions with high constitutionally supercooled liquid at the dendrite front [61].

Liu et al. [62] proposed the underlying mechanisms that govern the columnar to equiaxed transition (CET) in the SLM processed IN718, using a well-tested multiscale phase-field model. The CET at the center of the melt pool was mainly attributed to the heterogeneous nucleation because of the constitutional supercooling at the tail of the melt pool and a lower ratio of *G*/*R*. Under rapid cooling conditions, because of limited diffusion and the solubility difference between the solid and liquid, solute concentration at the solid/liquid interface gets higher than the rest of the liquid. As a result, constitutional supercooling/undercooling, defined as the liquidus temperature difference at the solid/liquid interface and the bulk of the liquid, occurs. The mean undercooling (ΔT) required to promote heterogeneous nucleation for CET was considered ~ 33.6 ± 5 °C for IN718. At the melt pool bottom, the high ratio of *G*/*R* (10^8 °C s/m^2) and low undercooling ($\Delta T < 1$ °C) led to epitaxial columnar solidification. As the solidification progresses to the center of the melt pool, sufficient solute gets segregated in the terminal liquid, and high undercooling was measured ($\Delta T > 33.6$ °C), which promotes heterogeneous nucleation and equiaxed solidification (Fig. 7).

Although the very high temperature gradients during MAM ~ 10^6 °C/mm limit the solute segregation [63], both the fine grains at the melt pool center and columnar grains close to the boundaries within a single layer are reported in many alloys systems, e.g., DEDed IN718 [64], DEDed Ti–6.5Al–3.5Mon–1.5Zr–0.3Si [65], DEDed Waspaloy [66], and SLMed Cu-13Sn [30]. In the DED processed functionally graded materials, the CET was attributed to the constitutional supercooling rather than the cooling conditions. The mean grain size of the BCC-matrix close to the substrate is found ~ 2 µm for $Ti_{25}Zr_{50}Nb_0Ta_{25}$ and increased to ~ 60 µm for $Ti_{25}Zr_0Nb_{50}Ta_{25}$ at the top. To confirm that these effects are not due to the cooling rate differences, the authors have produced samples with reverse composition gradient with Nb-rich close to the substrate and Zr-rich close to the tip, and interestingly, the grain size spread was also reversed. The elemental segregation of Ta in Zr-rich regions has caused constitutional supercooling and led to heterogeneous nucleation and equiaxed solidification [19]. Similar observations were reported in the DED processed functionally graded $AlCrFeMoV_x$ high entropy alloy (HEA) parts, with fine grains in the V-rich regions on the top and coarse-grained in the V-lean regions close to the substrate. The authors attributed this grain size variation to the constitution supercooling, as the increase in the V concentration reduces the melting point of the alloy [67]. The widely studied Ti–6Al–4V alloy showed profound columnar grain growth along the build direction. The suppression of equiaxed solidification, although with ~ 10 wt% of the alloying elements and high solidification rates, is attributed to the high partition coefficients of Al and V in Ti, and the narrow

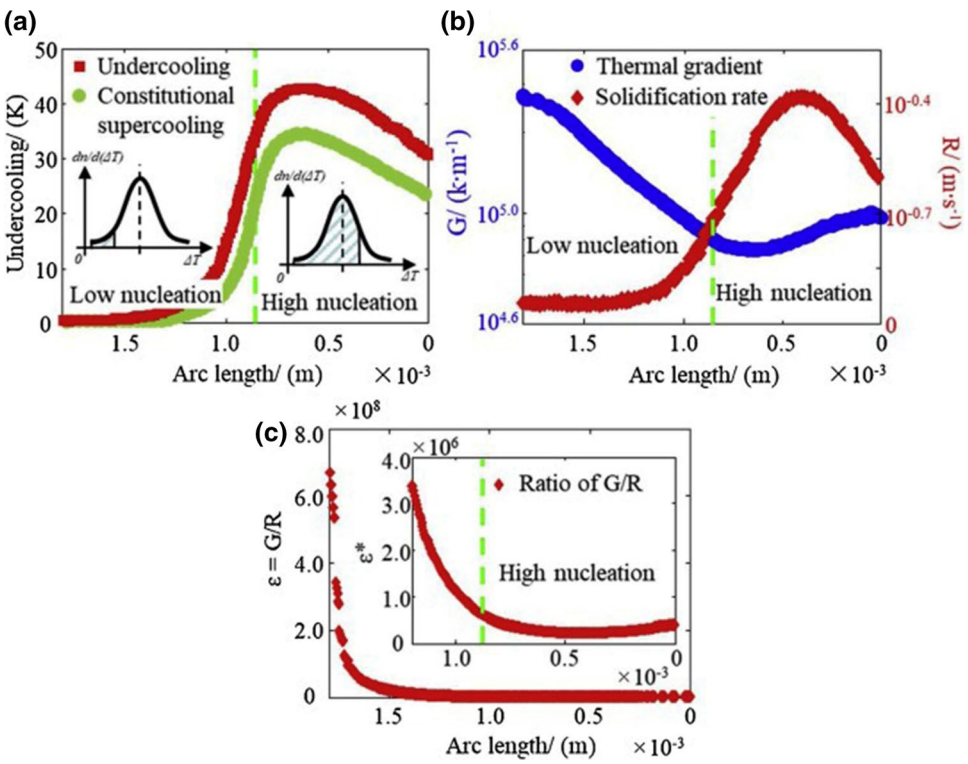

Fig. 7 Variations of undercooling and constitutional supercooling **a**, thermal gradient (*G*), and solidification rate (*R*), **b** from the surface to the bottom of the met pool, and **c** the ratio of *G*/*R* at the tail of the melt pool near the solid/liquid interface [62]. Reproduced with permission from Elsevier

solidification range which limits the segregation and degree of constitutional supercooling [60].

The profound epitaxial columnar grains in the build direction is due to the layer-by-layer part fabrication. When a new layer is deposited, the solidification begins from the MPBs. As the composition and crystal structure of the newly deposited layer matches with the previously deposited layer, the solidification occurs by epitaxial growth from the partially melted grains in the previous layer. The epitaxial growth occurs spontaneously in the new layer, without any nucleation barrier [57, 58]. However, when processing multi-materials, functionally graded materials, and the first layer on a dissimilar substrate, the new phase nucleation has to overcome an energy barrier for solidification [68]. While the epitaxial growth occurs close to the MPBs, competitive growth dominates the melt pool microstructure [69–72]. The grains tend to grow along the solidification front in the maximum temperature gradient direction, which is perpendicular to the MPBs (higher G) toward the pool surface (lower G). Therefore, in a polycrystalline material, several grains with different crystallographic orientations grow epitaxially into the melt pool. However, the growth direction of the columnar grains is also dependent on the crystal structure of the material. The easy growth direction for different crystal structures is given in Table 1 [57, 73]. Therefore, the grains whose easy growth direction, for instance, <100> for FCC materials, is along the maximum heat flow direction would grow faster than the other grains. This phenomenon is known as competitive growth [57]. Competitive growth results in a heterogeneous grain structure with a few columnar grains outgrow over the slower growing misaligned dendrites [57]. In many FCC metals, competitive unidirectional columnar grain growth is the typical microstructure observed along the build direction [16, 74]. In SLM processed Cu-13Sn alloy [30], heterogeneous grain structure with alternate layers of fine and coarse grains are reported along the build direction and laser scan direction, as shown in Fig. 8. The spatial variations of the G and R within the melt pool and the competitive growth of columnar grains are attributed to the presence of heterogeneous grain structures.

It is important to note that the grain growth along the heat flow direction is dependent on the melt pool geometry and the thermophysical properties of the material. The melt pool geometry controls the grain orientation. The thermo-physical properties of the material (the easy-growth direction and the undercooling) control the crystal growth direction and the driving force during solidification [59].

As shown in Fig. 9, a deeper melt pool would result in a grain structure with a few columnar grains grown vertically from the bottom of the MPBs, and an angle to the heat flow direction from the sides depending on the local curvature of the MPB. However, when the melt pool is shallow and wide, the grains tend to grow vertically along the heat flow direction [52, 54]. Note that we see the longitudinal section of the melt pool in Fig. 9. The transverse section of the melt pool still shows a highly localized hemisphere shape melt pool with columnar grains growing perpendicular to the MPBs. Qi et al. [75] demonstrated the effect of melt pool geometry on the grain structure in SLM processed Al alloy AA7075. In the conduction mode, because the melt pool is shallow (~150 µm deep and ~100 µm wide), the G/R does not change significantly within the melt pool: predominantly columnar grain structure was observed. However, in the keyhole mode, the melt pools are deeper (~350 µm deep and ~200 µm wide), and fine equiaxed grains form at the center of the melt pool. Sun et al. [76] reported similar observations in the SLM processed 316L SS. The samples produced with lower laser power 350 W (shallow melt pool) revealed an entirely columnar grain structure. In contrast, the samples produced with higher laser power 950 W (deeper melt pool) showed a mixed microstructure with equiaxed grains at the melt pool center and columnar grains at the pool boundaries.

Almost always, irrespective of the alloy composition, MAM products show a fine-grained microstructure compared to the conventional castings. The small melt pool size (typical melt pool size ~150 µm × 80 µm) and a very high-temperature gradient (10^3–10^6 °C/mm [63]) result in the rapid solidification of the material. Further, the high heating and cooling rate would induce significant superheating and undercooling, which would enhance the nucleation rate and suppress the grain growth. The fineness of the solidification structure, i.e., dendrite arm spacing d, can be predicted in terms of the cooling rate $G*R$, which can be expressed as Eq. (1) [57].

$$d = at_f^n = b\left(\varepsilon_C\right)^{-n}, \tag{1}$$

Table 1 Easy growth direction for various crystal structures [54, 57]. Reproduced with permission from Elsevier

Crystal structure	Easy-growth direction	Examples
Face-centered cubic (FCC)	<100>	Al alloys, austenitic stainless steels, Cu alloys, Ni alloy
Body-centered cubic (FCC)	<100>	Carbon steels, ferritic stainless steels
Hexagonal close-packed (HCP)	<1 0 $\bar{1}$ 0>	Ti alloys, Mg alloys
Body-centered tetragonal (BCT)	<110>	Tin

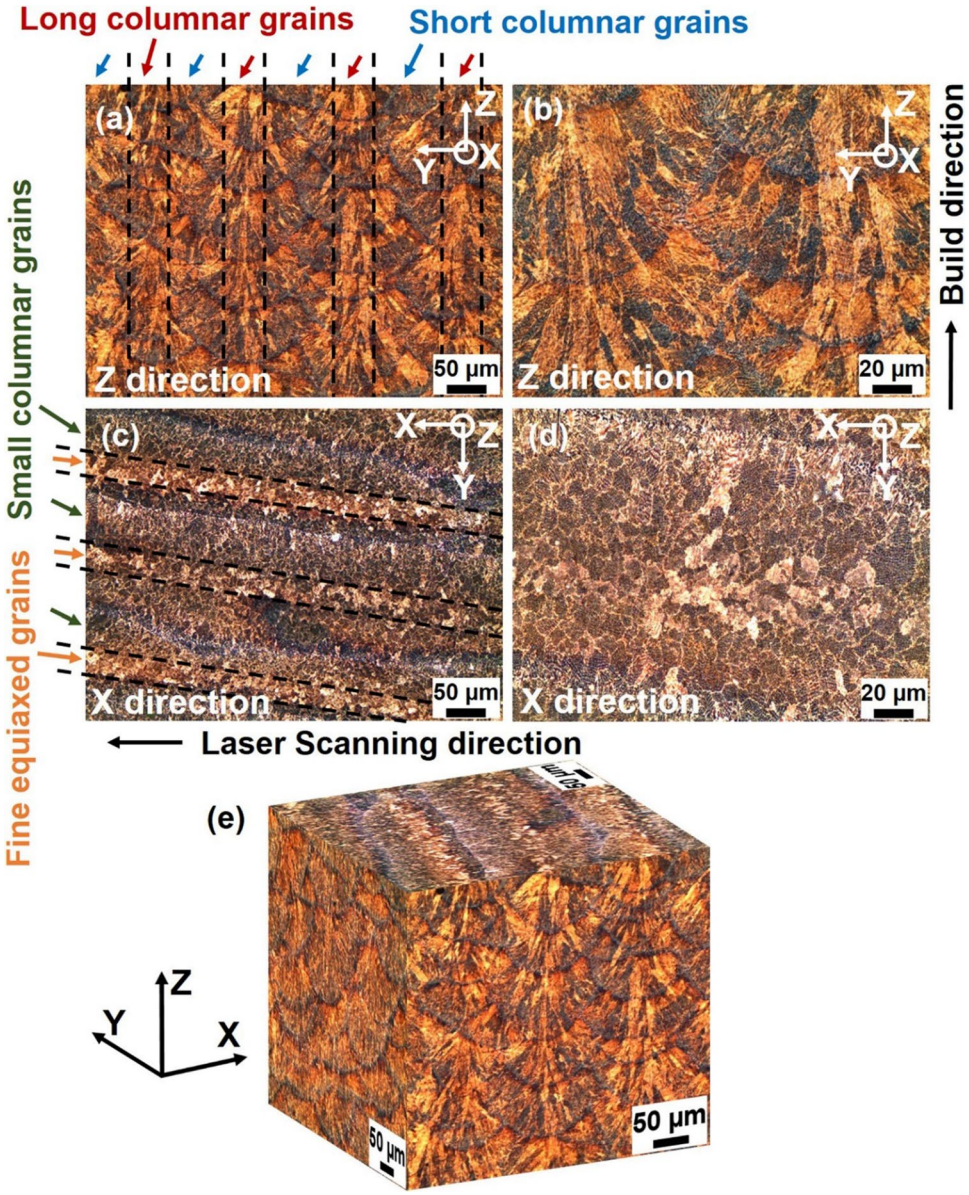

Fig. 8 Optical micrographs of the SLM processed as-built Cu–13Sn alloy **a**, **c** low and **b**, **d** high magnification images taken along build direction (Z-direction) and laser scan direction (X-direction), respectively. **e** Three-dimensional optical micrographs [30]. Reproduced with permission from Elsevier

where a, b, and n are material specific constants, t_f is local solidification time, and ε_C ($=G^*R$) is the cooling rate. The slower the cooling rate, the longer the time available for coarsening and the larger columnar grain spacing or width.

The grain size also depends on the MAM process used. The SLM processed Ti–6Al–4V showed a finer grain structure than the DED technique. Further, the SLM processed Ti–6Al–4V revealed acicular α'martensite, whereas the DED processed Ti–6Al–4V revealed fully laminar α-plates [77]. The smaller melt pool size and associated higher temperature gradient in the SLM samples are considered the primary cause for these microstructure differences. The EBM processed Ti–6Al–4V builds showed relatively coarse grain structure with lower α'martensite, compared to the SLM builds. Further, the degree of columnarization of EBM samples was found much higher than that of the SLM samples along the build direction. The high preheating temperatures in the EBM process lowers the cooling rates and provides sufficient time for the prior-β grains to grow. Also, it causes in situ heat treatment of the α'martensite formed during solidification and develops an α + β structure [78–80].

The processing parameters have a direct impact on the grain size. In the DED processed AlCoCrFeNi, an increase in the scanning speed from 2.5 to 40 mm/s is shown to change the cooling rate from 2.6×10^3 to 4.4×10^4 °C/s, which led to the decrease in the average grain size from 108.3 to 30.6 μm [81]. In another work, in the DED processed 316L SS, the samples produced with lower power showed a finer grain structure compared to the samples produced with higher laser power. This is because higher power

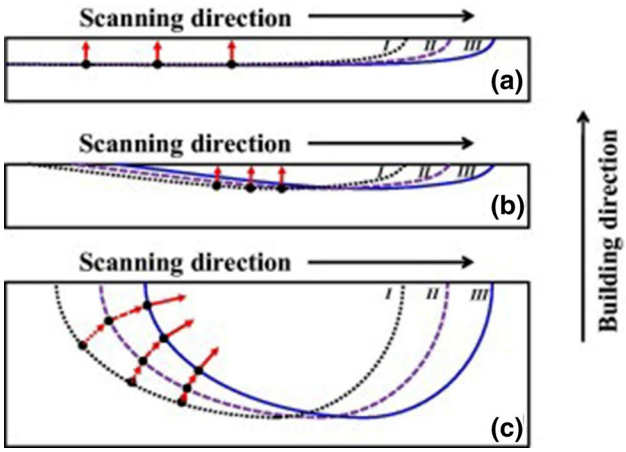

Fig. 9 Schematic illustration of the growth direction of the columnar grains in the longitudinal plane of the melt pool, **a** vertical grain orientation which is location dependent, **b** nearly vertical grain orientation from the long and shallow melt pool, **c** inclined grain orientation, which is location dependent for the deeper melt pool. The locations of the melt pool along the scan direction are represented by I, II, and III [54]. Reproduced with permission from Elsevier

results in a larger melt pool size and slower cooling rates than the samples built with the lower laser power [82]. The scanning strategy plays a major role in the grain orientation in the SLM processed Ti–6Al–4V alloy [46]. The grains tend to grow along the maximum heat flow direction, more specifically along the laser scan direction, causing orientation difference with change in the laser scan path. With unidirectional scan strategy, grains with identical orientation inclined at about 40° across the layer were obtained along the building direction. However, a bi-directional scan strategy resulted in a zig-zag herringbone pattern.

Grain size dependence with the sample height was reported: fine grains were near the base plate, and the grain size increased with the sample height. The heat build-up with the sample height resulted in grain coarsening. Yadollahi et al. [56] reported that the inter-layer time interval strongly influences the cooling rate, in turn, the grain size and mechanical properties. A longer time interval between layer depositions would allow the previously deposited material to cool down and overcome the problem of heat build during part fabrication, resulting in uniform fine-grain structure across the sample height [42]. The grain size was not significantly influenced by build geometry or distance from the base plate in the DED processed 304L SS [83].

Microstructural strategies, such as the addition of inoculants, have been shown very effective in achieving equiaxed grain structures in the melt pool. In a solidification crack susceptible aluminum alloy AA7075, an addition of 4% Si was shown to refine the grain size and modify the last solidifying eutectic liquid composition. A unique microstructure with equiaxed grains at the MPBs and columnar grains at the center of the melt pool was reported. The Si particles effectively acted as inoculants at the early stages of solidification at the MPBs, and as the solidification progresses to the center of the melt pool, some preferentially oriented grains start to outgrow others, resulting in a columnar grain structure. The modified eutectic composition (Mg_2Si) with Si addition is responsible for achieving a crack-free sample with a high relative density ~ 99% [84]. Similar microstructures were reported in another crack susceptible Al alloy (Al–Cu–Mg) with a 2% Zr addition. The formation of the Al_3Zr intermetallic phase with a similar lattice parameter (4.007 Å) as the Al matrix (~ 4.049 Å) resulted in the grain refinement [85]. A small amount of Zr addition to AA7075 alloy also resulted in an equiaxed grain structure [86].

Wang et al. [65] reported that by varying the specific powder deposition rate, the grain structure could be controlled during the DED processing of Ti alloy (Ti–6.5Al–3.5Mo–1.5Zr–0.3Si). Low specific mass deposition rate (< 15 g/min) promoted the formation of large columnar prior-β grains because of high melt superheating, large melt pool penetration, and high-temperature gradient. In contrast, a high specific mass deposition rate (> 50 g/min) favored the production of fine near equiaxed prior-β grains because of insufficient powder melting, resulting in heterogeneous nucleation within the melt pool. Further, a mixed grain structure with alternate layers of coarse and fine grains resulted in an intermediate specific mass deposition rate (15–50 g/min) because the penetration depth is not deep enough to re-melt the top equiaxed grains of the underlying deposited layer.

It is well known that the grain boundaries efficiently act as strong barriers to dislocation movement and contribute to the yield strength of the material obeying the Hall–Petch relationship Eq. (2)

$$\sigma_y = \sigma_o + \frac{k}{\sqrt{d}}, \tag{2}$$

where σ_y is the yield strength of the material, σ_o is a material constant, k is the strengthening coefficient, and d is the average circular diameter of the grains assuming equiaxed grain structure. However, the additive parts have a spatial heterogeneous grain structure with a mixture of equiaxed grain and highly elongated columnar grains. Direct usage of the Hall–Petch equation to additive parts is difficult. Therefore, to quantify the average grain size of the elongated columnar grains, Wang et al. [82] approximated the grains as elliptical and defined the average grain size as Eq. (3).

$$d_{avg} = \pi ab, \tag{3}$$

where d_{avg} is the average grain size, and a and b are the major and minor axes of the columnar grains, respectively. In another work, the average grain size in the DED [87] and

SLM [88] processed 316L SS is expressed as the distance between the adjacent columnar grain boundaries, which is denoted as the effective grain size ($d_{eff.}$). To estimate the combined effect of these spatial heterogeneous grain structure with equiaxed and elongated columnar grains in SLM processed 1%C-CoCrFeMnNi, Park et al. [29] employed a simple rule of mixtures approach. If the columnar and equiaxed grains are oriented parallel to the loading direction, the effective grain size ($d_{eff.\ parallel}$) is expressed as

$$\frac{1}{d_{eff.parallel}} = \frac{V_e}{d_e} + \frac{V_c}{d_c}. \tag{4}$$

On the other hand, if they are arranged in series to the loading direction, the effective grain size ($d_{eff.\ series}$) is expressed as,

$$d_{eff.series} = V_e d_e + V_c d_c, \tag{5}$$

where V_e and V_c are the volume fractions of the equiaxed and columnar grains, respectively; d_e and d_c effective grain sizes of equiaxed and columnar grains, respectively.

Wang et al. [89] produced 316L SS using SLM with different columnar grain sizes and showed that columnar grain size has a low influence on the mechanical properties. The samples with finer columnar grains (20 µm) showed lower strength than the coarse grain samples (45 µm), following Hall–Petch relation Eq. (2). This was attributed to the presence of the finer cell size in the latter compared to the former. The solute segregation and dislocation tangle at the cellular boundaries (low angle grain boundaries) had a more significant influence on the mechanical properties than the columnar grains (high angle grain boundaries).

4.3 Sub-grain Cellular Structure

The formation of sub-grain cellular structure in MAM parts is still an open question and an incompletely understood topic. Three possible governing mechanisms are proposed for cellular structure formation in the literature (1) cellular solidification [89–92], (2) geometrically necessary dislocations (GNDs) rendered by thermal heterogeneities, and (3) deformation-induced dislocations due to high residual stresses [93–95]. Irrespective of how the cellular structure forms, the cell walls are always decorated with dense dislocation tangles. Only a subset of them reports the segregation of solute elements to the cell walls.

The widely accepted mechanism for the sub-grain cellular structure is cellular solidification [89–91]. The high-temperature gradients of the order of 10^4–10^6 °C/s within the melt pool during MAM would develop strong surface tension driven Marangoni convection [63]. Further, the local differences in the heat transfer within the shallow melt pool would result in non-uniform heating and generation of thermo-capillary convection within the melt pool. Such a melting environment leads to the generation of a strong vertex in the melt pool, leading to a complex cellular structure.

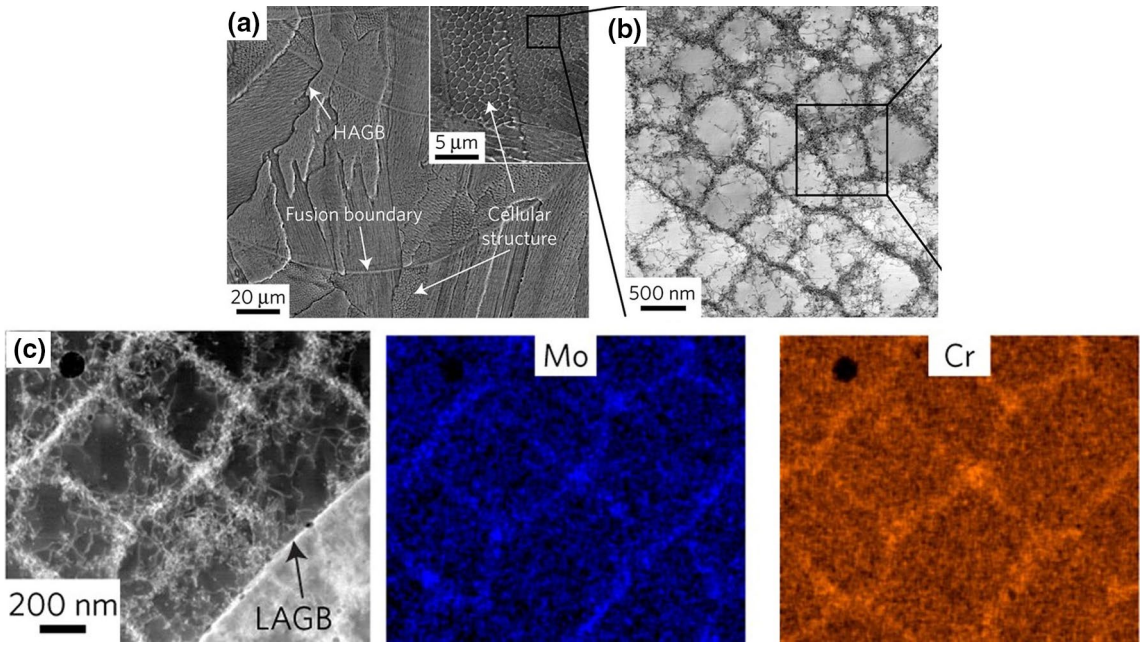

Fig. 10 Cellular structure in the SLM processed 316L SS samples in as-built condition **a** SEM-BSE micrograph showing sub-grain cellular structure inside the columnar grains. **b** TEM micrograph showing cellular boundaries with high dislocation density, **c** TEM-EDS maps revealing segregation of solute elements Mo and Cr to the cellular boundaries [89]. Reproduced with permission from Springer Nature

Besides, any rejected solute at the solid–liquid interface gets segregated to the cellular boundaries by surface tension, resulting in a cellular structure with distinct compositions at the core of the cell and along the cellular walls (Fig. 10). The solute atom segregation at the cellular walls is considered the reason for the high dislocation density at the cell walls than in the cell interiors.

In most Al alloys, the mode of solidification is proposed as cellular, irrespective of the MAM process used. Further, the solubility of the solute in the solidifying matrix reduces with temperature, and the solute rejected to the growing solid–liquid interface gets segregated to the cellular boundaries, leading to cellular sub-structure with a distinct composition at the cell interior and the cell wall [37]. Prasanth and Eckert [92] have studied cellular structure formation in four different SLM processed alloys: Al–12Si, AlSi10Mg, CoCrMo, and 316L. The authors compared the solidification process of the SLM process with the thin-film process because the melt pool dimensions in both the processes are similar. A criterion was proposed for cellular structure formation: (1) a binary or a multi-component system with only two phases, (2) the solute solubility should reduce in the solidifying solid with temperature, (3) the solute should possess a higher melting point than the matrix with a difference of at least 673 K.

Recently, Birnbaum [93] proposed the underlying mechanisms responsible for the cell structure formation in the SLM processed 316L by observations on single-beads. The combination of lower yield stress at high-temperature and thermal strain results in the dislocation cell structure during cooling. The segregation of solute elements at the cellular walls was attributed to the strain aging to lower the strain field around the dislocation cell structure. The authors proposed that, because the diffusion distances are small (~ 100 nm), strain aging by diffusion of substitutional elements Cr and Mo to the cell walls is feasible even at high cooling rates. In the DED processed 304L alloy [83], the dislocation cell structure was devoid of any segregation of the solute element. The authors noted that the dislocation cell formation is independent and not just associated with compositional micro-segregation.

Most recently, the origin of the high dislocation density in MAM parts was investigated [94, 95]. The SLM processed pure Cu samples showed a high fraction of low angle boundaries (~ 63%) with an estimated average dislocation density $\sim 10^{16}\ m^{-2}$, as high as that of severely deformed metals. The authors employed an integrated multi-physics modeling framework and proposed that thermal stress, which develops because of the localized heating/cooling heterogeneity during layer-wise part fabrication, is high enough to cause plastic deformation in the material. To minimize local strain energies, these deformation-induced dislocations self-align themselves into low-energy cells via dislocation cross-slip/climb. Further, the dislocation cell boundaries might facilitate solute diffusion and result in chemical segregation [94]. Murr et al. [95] report a high dislocation density of $\sim 5 \times 10^9\ cm^{-2}$ for EBM Ti–6Al–4V compared to wrought forged Ti–6Al–4V parts $\sim 2 \times 10^9\ cm^{-2}$. It was speculated to be perhaps the repeated reheating cycles through the β-transus temperature, and the high thermal stresses have resulted in irreversible plastic deformation of the weaker β phase in Ti–6Al–4V [78].

There are several questions unanswered in the reasons for the evolution of the sub-grain cellular structure with high dislocation density. Suppose it is related to the cellular solidification and elemental segregation, why the pure metals show high dislocation density at the cell walls, also, why the cellular walls are characterized by low angle boundaries [83, 94]? On the other hand, if it is due to the deformation-induced dislocations because of the high thermal stresses in MAM parts, why the cellular structure is seen in a few alloy systems [40, 92, 94]? Also, cellular structure is reported even in the EBM processed materials, in which the residual stresses are low [96, 97]. Further, if they are due to deformation-induced dislocations, why the cells maintain a specific orientation to the solidification front and thermal gradient direction, and why they are present as colonies with different orientations within the columnar grains [51, 98, 99]? Moreover, why the solute segregation is observed only at the cellular walls and not at the inter-dendritic regions (high-angle boundaries) [92]? Further, any high-temperature treatment would annihilate the deformation-induced dislocation. However, the cellular dislocation structure was shown to be stable even after high-temperature heat treatment [100]. In the SLM processed 316L, the traces of the cellular structures are present, even after heat treating the as-built sample at 1100 °C for 6 min, followed by furnace cooling, although with a lower dislocation density and a larger cell size [94].

From our understanding, we speculate the reasons for the cellular structure formation can be a combination of several factors, including cellular solidification and deformation-induced dislocation generation with strain-aging. Based on the alloy system, maybe one is dominating the other. In pure metals, the temperature gradient may be dominating, and in alloy systems with strong segregation, constitutional supercooling may be dominating. Also, material composition and crystal structure might play roles as they influence the solidification phenomena [101]. In Ti-alloys, although high dislocation densities are reported, they did not show cellular structure [102]; however, Al alloys [40] and steels [103] showed cellular structures. Theoretical models considering all the aspects of solidification, crystal structure, residual stresses, and sample location would give more insights.

The cellular structure within the columnar grains is present as several colonies with small misorientation [104, 105]. If the misorientation between two cellular colonies

is small, they merge and grow along the temperature gradient direction. While the columnar grains grow epitaxially perpendicular to the MPBs along the maximum temperature gradient direction [106], the cellular structure grows along the easy growth direction of the material (Table 1) [99]. The angle between the cellular structure and the MPBs varies from 0° to 54.7° [98, 99]. If the columnar grain grows in an epitaxial mode from the previous layer, the cellular colony in the previous grain maintains continuity in the new layer. However, if the columnar grains have a non-epitaxial mode of growth, the cellular colony would be restricted at a melt pool [104].

It is worthwhile to note that the MAM process parameters such as laser scan speed, laser scan strategy, hatch spacing, and layer thickness control the cellular structure formation [90, 107]. In the SLM processed 316L SS, it was shown that a 90° rotation of the laser scan path for each new layer results in a sharp change in the thermal gradient direction and restricts the epitaxial grain growth at the MPBs, thereby the continuity of the cellular colony is restricted. A continuous cellular colony across the MPBs strengthens the MPBs and exhibits better mechanical properties compared to the restricted cellular continuity [90, 107].

The MAM processing method can influence the cellular structure evolution during part building [96, 97]. The cellular structure was distinctly different in the SLM, and EBM processed 316L SS. The SLM processed 316L samples revealed fine regular-shaped cells (~ 500 nm) with elemental segregation and high dislocation density at the cellular boundaries. However, the EBM processed samples showed relatively coarse, irregular-shaped cells (1–9 µm) with negligible elemental segregation to the cellular boundaries and low dislocation density. These differences are attributed to the usage of high preheating temperature (700–800 °C) during EBM processing, which dramatically decreases the cooling rate and promotes diffusion, causing coarsening of the cellular structure and compositional homogenization [96, 97].

The presence of cellular structure affects the solid-state phase transformation. In the SLM processed precipitation-hardened martensitic stainless steel (17-4PH), Freeman et al. [103] showed complete suppression of thermal martensite formation. The laser PBF samples showed a hierarchical microstructure with coarse columnar grains (10–100 µm) containing sub-grain cellular structures (0.2–2 µm) with dense dislocation walls. The samples showed ~ 50 vol% martensite, but no further transformation occurred on cooling the as-built samples to − 196 °C/1 h in liquid nitrogen. It is known that the austenite grain size has a strong influence on the martensitic transformation. The presence of small cell size with dense dislocation walls is sufficient to stop thermal martensite formation.

The solidification cell size has a dependence on the part built height. In the DED processed 304L, the regions closer to the baseplate showed a finer cell size than the regions far from the baseplate [83]. At the start of the deposition, the base plate is at room temperature and acts as an effective heat sink, resulting in a higher cooling rate and a finer cellular structure. With the progress in the deposition, heat builds up, and the cooling rate reduces, resulting in the coarsening of the cellular structure. Further, the regions closer to the baseplate showed a higher dislocation density compared to the regions far from the base plate. The authors attributed it to the differences in the mechanical constraint offered by the base plate on the deposit. The deposited material closer to the baseplate experiences more constraint than the deposit far from the baseplate; therefore, it undergoes more plastic deformation and higher dislocation density [83]. This behavior is basically equivalent to the Saint–Venant's principle [108].

In a recent study on 316L SS, it was shown that the cell orientation could be tailored using the SLM processing parameters [51]. The samples fabricated with lower energy density showed cells grown along <110> direction at ~ ± 45° to the build direction, and along <100> direction parallel to the build direction. On the other hand, the specimen fabricated under higher energy density showed cells only along <110> direction. The laser scan speed influenced the solidification rate significantly, even when the energy density is kept constant. At a higher laser scan speed ~ 7000 mm/s, finer cellular structure with cell spacing of ~ 300 nm was obtained, and at a relatively lower scan speed ~ 566 mm/s, coarser cellular structure with cell spacing of ~ 660 nm was seen. Although the cell size is significantly refined at the higher scan speeds, the manufactured part showed very high porosity. Therefore, a trade-off should be maintained between strength and build quality [93]. In the SLM processed CoCrFeMnNi HEA, build orientation was shown to affect the grain size. However, it did not affect the size of the cellular structure and dislocation density [109].

The cellular structure plays a significant role in the strengthening of the MAM parts because the cell walls effectively trap or arrest the dislocation motion during plastic deformation. In the SLM processed 316L [89], to study the role of cellular structure on the strengthening behavior, post tensile fractured samples were analyzed at different strain levels. Although the cellular walls are low angle boundaries ~ 1°–2° (Fig. 11) [89, 103, 104], the dense dislocation and the segregation of solute elements around the walls make them sufficiently robust to contain the dislocation motion and strengthen the material in a manner generally attributed to grain boundaries. At a relatively low strain (~ 3%), dislocation slip was dominant, the cellular size, shape, and local misorientation across the walls remain unchanged (Fig. 11a), and the KAM value inside the cells increased

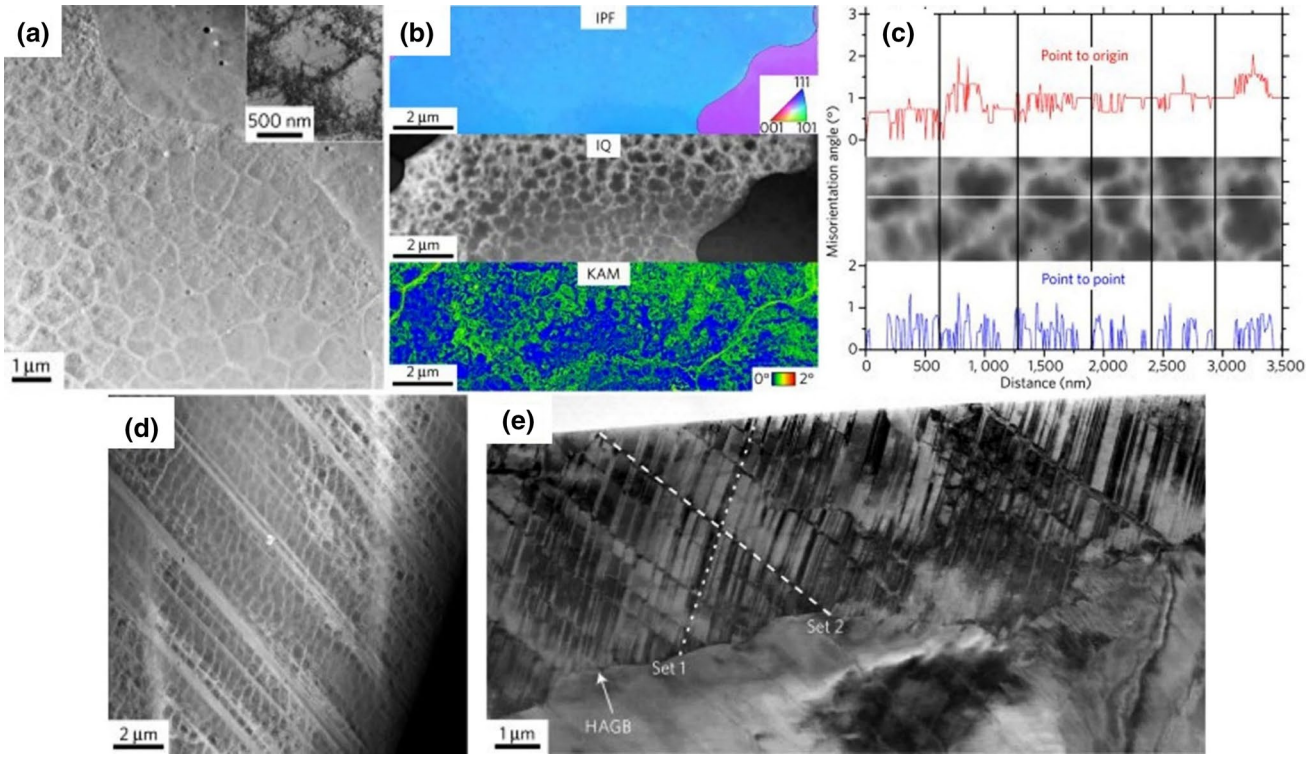

Fig. 11 Post-deformation tensile fracture sample micrographs of the SLM processed 316L SS. **a** TEM micrograph at ~3% tensile strain, the small change in shape and size of the cells are shown in the inset, **b** inverse-pole figure (IPF) map (top) with associated image quality (IQ) map (middle), and kernel-average misorientation (KAM) map (bottom) showing significant dislocations trapping at the cellular walls at 3% strain, **c** plots of the misorientation angle variation across multiple cells of the cellular structure after ~3% strain, **d** TEM micrographs at 12% tensile strain, showing intersections of deformation twins with the cellular walls. **e** TEM micrograph revealing the intersections of twin sets and grain boundaries acting as nucleation and blockage sites for twinning [89]. Reproduced with permission from Springer Nature

by 1.5° (Fig. 11b, c). Twinning played a dominant role at higher strain levels ~ 12% (Fig. 11d). Numerous events of twin sets crossing inside grain and twins crossing across the cells provide a unique three-dimensional network of twin-twin, twin-cellular walls, and twin-dislocation (Fig. 11e). Even at a higher strain level of ~ 36%, the cellular structure is retained. Therefore, the steady work hardening rate in the SLM samples is attributed to the presence of the sub-grain cellular structure, deformation twinning, and their interactions, which led to realizing high uniform tensile elongation [89].

Wu et al. [110] conducted in situ compression tests inside TEM to show the effect of cell boundaries in limiting the dislocation movement during deformation in the SLM processed AlSi10Mg alloy. The Si-segregation and Si-particle distribution were reported very non-uniform at the cell boundaries. At low strains, the dislocations are localized within the cell, and with the further increase in strain, some dislocations started transmitting through the thin cell boundary with low Si segregation and discrete Si particles. However, no apparent signs of transmission of dislocations through the thick cell boundaries were seen. In another work, a dramatic drop in strength is noted in the heat-treated SLM processed CoCrFeMnNi HEA parts. The absence of cellular dislocation structure after heat treatment results in the strength drop [109].

Wang et al. [89] analyzed the strengthening of the SLM processed 316L by assuming Hall–Petch type strengthening behavior, considering cell size Eq. (2). The calculated yield strength is ~ 88% of the measured yield strength, suggesting that the sub-grain cellular structure contributes to the higher strength in the SLM processed 316L. The conventional Hall–Petch relation was modified by superposing various strengthening contributions, i.e., dislocation density (ρ) and microstructural partitioning dimensions (Δ) considering phase dimension, cell size, and twin spacing [88, 95]: the yield strength σ_y of the SLM processed 316L is expressed as:

$$\sigma_y = \sigma_o + K(d)^{-\frac{1}{2}} + K'(\rho)^{\frac{1}{2}} + K''(\Delta)^{-n}, \quad (6)$$

where K, K', K'', and n are material constants ($0.5 < n < 1.0$).

It is established from many independent works that MAM parts contain a high dislocation density at the cellular walls, which are identified as the primary source for

enhanced strength in the SLM samples [109]. Many FCC metals subjected to plastic deformation, form dislocation cell substructures. An empirical relationship between the bulk dislocation density (ρ) and the dislocation cell diameter (d) is given by Kocks and Mecking, Eq. (7) [111].

$$\rho = \frac{200}{\pi d^2}. \tag{7}$$

Smith et al. [83] used Bailey-Hirsch relation Eq. (8) to estimate the effect of dislocation density on yield strength (σ_y) of the DED processed 316SS.

$$\Delta\sigma_y = M\alpha Gb\sqrt{\rho}, \tag{8}$$

where G is shear modulus, b is Burgers vector, M is the mean orientation factor, α is constant, dislocation density ρ comprised of both statistically stored dislocations and GNDs. Smith et al. [83] reported that the dislocation density obtained from the Eq. (8) closely matched the GND density measured from the EBSD in DED processed 304L material. It implies that the total dislocation population in the DED 304L represents the GNDs, as expressed in Eq. (9) [112].

$$\rho_{GND} = \frac{2}{b}\left(\frac{d\theta}{du}\right), \tag{9}$$

where u is the unit length, b is the Burgers vector, and θ is the dislocation-induced crystallographic misorientation.

4.4 Compositional Heterogeneity

The extremely high cooling rates during MAM result in significant solute supersaturation. During SLM, high cooling rates of the order of ~ 10^4–10^5 °C/s are measured [113]. Such rapid cooling rates would significantly reduce atomic diffusion, leading to solute trapping and resulting in supersaturation of α-matrix compared to the as-cast counterparts. Supersaturation of the matrix was reported in several alloys, e.g., SLMed Al–12Si [40], SLMed Al–10Si–Mg [114], DEDed Al–1Sc–0.4Zr [115], SLMed Al–9Si–3Cu–1Fe [116], SLMed Cu–13Sn [30], and DEDed Cu–3.4Cr–0.6Nb [117]. In the DED processed $AlCrFeMoV_x$ alloy, increased solubility of V was reported up to 18.5 at% [67].

The supersaturation of the α-matrix resulted in a reduced volume fraction and size of the equilibrium second-phase in the as-built MAM parts compared to the as-cast counterparts. The as-built Al–12Si alloy SLM samples revealed a novel eutectic microstructure with very fine spherical Si particles, unlike the eutectic microstructure with large rod- or needle-like Si particles in the as-cast samples [40]. Karthik et al. [30] reported finer δ-phase (~ 0.2 ± 0.12 µm) in the as-built Cu-13Sn SLM samples compared to the as-cast samples (~ 7 ± 5 µm). Further, in the SLM samples, the δ-phase appeared more discrete and with lower volume fraction (~ 9 ± 1%) than the as-cast counterparts with continuous inter-dendritic network and high volume fraction (~ 14 ± 1%) (Fig. 12). The higher degree of supersaturation of the α-Cu with Sn (~ 6.2 wt%) in the SLM samples resulted in a refined second-phases.

The degree of supersaturation in the as-built samples was sufficiently high enough to respond well to the direct aging heat treatment without a need for solution annealing step. Direct aging of the DED processed 300-Ni maraging steel resulted in uniform precipitation of Ni_3Ti, Ni_3Mo, and Fe_7Mo_6 phases [118]. In Cu alloys, significant supersaturation of the α-Cu matrix allowed the as-built samples to respond well to direct aging without an intermediate solution annealing step [119–121].

The multiple reheating cycles during part building caused *in-situ* heat treatment and resulted in the formation of fine nano-size precipitates or clusters from the supersaturated matrix. Kürnsteiner et al. [115] reported high density (~ 10^{23} m^{-3}) of Al_3Sc nano-precipitates in the DED processed as-built Al–1Sc–0.4Zr samples. The absence of such precipitation on the topmost layer confirms that the precipitation occurred because of the in-situ heat treatment, not during solidification (Fig. 13a, c). Further, the authors reported the formation of Zr shells around the Al_3Sc precipitates in the regions closer to the base plate (Fig. 13b, d). This was attributed to a higher degree of the supersaturation of Sc and Zr in the α-Al matrix closer to the base plate

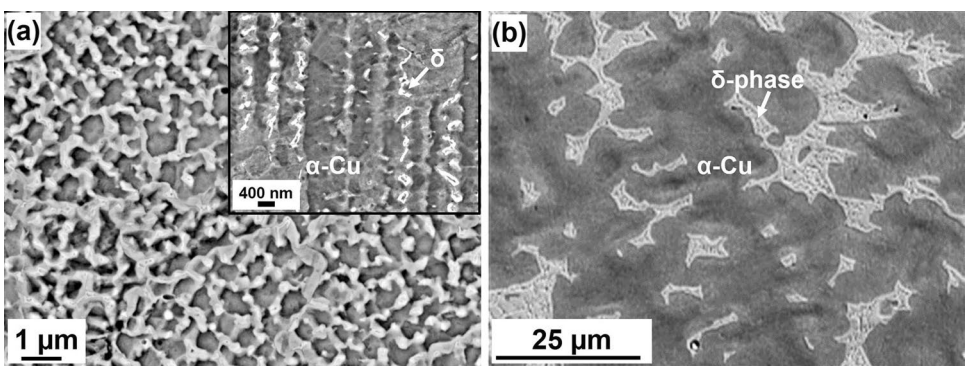

Fig. 12 SEM-BSE micrographs of the Cu-13Sn alloy **a** as-built SLM and **b** as-cast [30]. Reproduced with permission from Elsevier

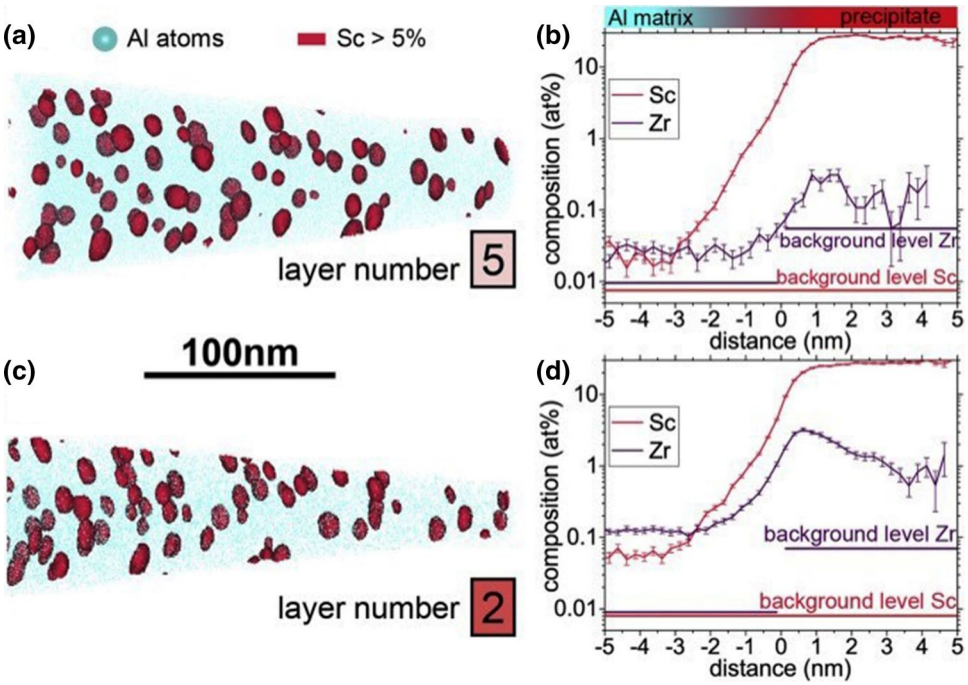

Fig. 13 Intrinsic heat treatment and precipitation of $Al_3(Sc, Zr)$ in the as-built DED processed Al–1Sc–0.4Zr samples. **a** and **c** show the APT isoconcentration surfaces taken from the 5th layer (top) and 2nd layer (bottom), respectively. The graphs in **b** and **d** show a proximity histograms that plot the chemical compositions as a function of the distance to the isoconcentration surface. The Al3(Sc, Zr) precipitates are highlighted in red [115]. Reproduced with permission from Elsevier. (Color figure online)

because of the much higher cooling rates near the baseplate. Similarly, Mg clusters and Mg–Si co-clusters are reported in the SLM processed as-built Al–10Si–Mg alloy samples [114]. In a more recent work on SLM of Cu–13Sn alloy, the as-built samples showed fine Cu-rich nano-precipitates in the supersaturated Cu–Sn matrix. It is speculated that the distinct microstructures developed during the SLM process can favor fine precipitation even in a sluggish system like Cu–13Sn [30].

In Al–12Si alloy, this spatially heterogeneous phenomenon is explained based on dissolution temperature (~ 1080 °C) and branching temperature (~ 1290 °C). Above the dissolution temperature, the Si particles start to melt, and above the branching temperature, the melt is homogeneous. The authors predicted the melt pool temperature to lie in between dissolution and branching temperatures (Fig. 14), which causes inhomogeneous molten metal composition. The faster cooling rates ~ 10^3 °C/s would freeze the inhomogeneous melt pool rapidly, resulting in a microstructure with a supersaturated Al matrix and fine nano-sized Sc particles [40].

Segregation of solute elements to the cellular boundaries is another feature of most MAM parts. Segregation is mainly due to the non-equilibrium solidification condition during MAM [92]. Because the MAM parts experience rapid cooling rates, they show relatively lower solute segregation than the as-cast counterparts. In high Mn steels (X30Mn22), while the as-cast alloys showed profound segregation (± 3.5 wt% from the nominal Mn composition), the SLM samples showed low Mn segregation (± 2 wt% from the nominal Mn composition) [122]. Unlike in castings that show segregation at the inter-dendritic regions, the segregation of solute elements in MAM parts predominantly occurs at the cellular boundaries. The exact reason why segregation is observed only at the cellular walls and not at the inter-dendritic regions is still not fully understood.

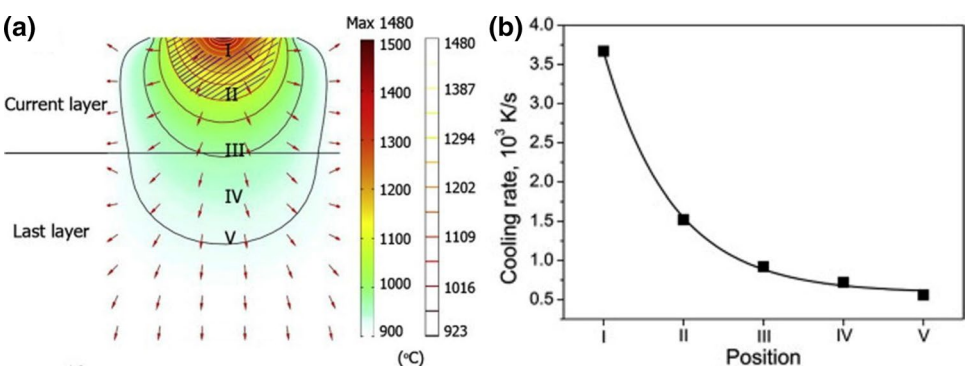

Fig. 14 **a** Temperature distribution in the molten pool of the Al–12Si alloy during SLM, based on COMSOL™ modeling. **b** Estimated cooling rates at the positions marked I–V in **a** [40]. Reproduced with permission from Elsevier

For the same alloy system, while a few report solute segregation at the cellular walls [89], many did not see them [76]. Interestingly, the cellular structure formation and the elemental segregation at the cell walls are closely related to the laser processing parameters. Wang et al. [89] produced 316L SS samples using two SLM machines (Fraunhofer and Concept laser). While the samples produced by the Concept laser machine showed strong elemental segregation of Cr and Mo to the cell walls, the Fraunhofer sample revealed a little segregation at the cell walls. The use of a higher energy density in the Fraunhofer samples with larger beam size, slower laser speed, and higher-layer thickness, significantly reduced the cooling rates and promoted elemental diffusion.

Depending on the processing parameters and protective atmosphere, there can be a loss in high-vapor pressure elements and pickup of gases such as nitrogen and oxygen [31, 123, 124]. The EBM processed Ti–6Al–4V showed lower Al ~ 5.1 wt% in the as-built samples [124]. The higher melt pool temperatures in Ti–6Al–4V, because of its low thermal conductivity and density, resulted in the vaporization of low melting Al. Mukherjee et al. [31] have presented a scale to rank the composition change during laser interaction, as shown in Fig. 15. As can be seen, IN 625 experiences the smallest, and Ti–6Al–4V experiences the most significant composition changes among the alloys considered. The loss of alloying elements was also reported in several other alloys, e.g., Mg and Zn evaporation in Al alloys [123], and Mn evaporation in 2.25Cr–1Mo steel, Alloy 800H, and SS316 [31]. The composition change, in turn, causes degradation in corrosion resistance and mechanical properties. Therefore, care should be taken during the processing of alloys with volatile alloying elements (e.g., Mn, Mg, Zn) by adjusting processing parameters such as laser power density and scanning speed.

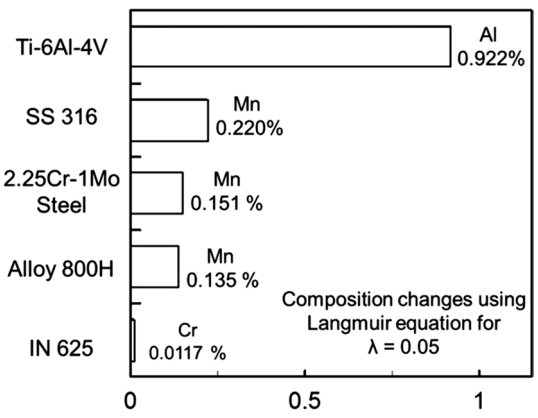

Fig. 15 Composition change (in wt%) by volatile elements due to vaporization during MAM processing of alloys [31]. Reproduced under the terms of the Creative Common License

The weight fraction W_f of the alloying element i after vaporization can be obtained using Eq. (10).

$$W_f = \frac{V\rho W_i - \Delta m_i}{V\rho - \sum_i \Delta m_i}, \tag{10}$$

where v is scanning speed, W_i is the initial weight percentage of element i in the powders. The amount of material vaporized, m_i can be estimated as:

$$\Delta m_i = \frac{LA_s J_i}{v}, \tag{11}$$

where L is track length, A_s is the surface area of the molten pool. The vaporization flux of alloying element J_i can be obtained from the Langmuir equation as follows:

$$J_i = \frac{\lambda P_i}{\sqrt{2\pi M_i T}}. \tag{12}$$

The deposited volume $V = A_t L$, where A_t is the melt pool cross-sectional area in the transverse direction, P_t is the vapor pressure of the alloy, M_t is the molecular weight of element i, T is the temperature, and λ is the positive fraction accounting for condensation of some vaporized atoms.

The cover gas used (Ar or N_2 gas) during the gas atomization and MAM processing influenced the phase stability of the MAM parts. In the SLM processed 17-4 PH martensitic stainless steel, the use of Ar/Ar, Ar/N_2, and N_2/Ar cover gas resulted in a fully martensitic microstructure. However, N_2/N_2 cover gas samples showed a high amount of retained austenite ~ 85%. The high thermal conductivity (~ 40% greater than the Ar gas) and strong austenite stabilizing ability of N_2 resulted in the higher retained austenite [125]. In another work on martensitic stainless steel AISI 420, small quantities of α-Fe and retained austenite γ were reported in the as-built samples. The higher oxygen content in the build chamber led to significant decarburization of the alloy [48].

Composition effects, including supersaturation of the matrix and solute micro-segregation, contribute to strengthening in MAM parts. The coherent internal stresses at the cellular walls or boundaries developed by the segregation of solute atoms can impede dislocation motion because there exists a spatial variation of the elastic modulus between the cell wall and interior. The local compositional differences are comparable to the typical early-stage of spinodal decomposed materials. Cahn hardening equations [126] for dislocation bowing describe the microsegregation strengthening effect, Eq. (13).

$$\Delta\sigma_y = 0.57M(A\eta Y)^{\frac{1}{3}}\left(\frac{2\pi Gb}{d}\right)^{\frac{2}{3}}, \tag{13}$$

where G is shear modulus, b is Burgers vector, M is mean orientation factor, d is approximated as the mean cell size,

$Y = \frac{2G(1+v)}{(1-v)}$ (assuming isotropic elasticity), and v is the Poisson ratio. A describes the amplitude of compositional microsegregation between the maximum solute composition at the cell boundary (c_b) and the minimum solute composition at the cell core (c_c), and $\eta = \frac{d \ln a}{dc}$ describes the lattice misfit caused by the increase in lattice parameter (a). The possibility of composition variations or fluctuation within the macroscopic samples and preferential segregation of trace elements are ignored, considering their effects to be small.

4.5 Phase Transformation

In this session, the solid-state phase transformations in MAM parts during cooling to room temperature are discussed. Further, the effect of multiple-reheating cycles on the phase transformation in the deposited layers is also discussed.

4.5.1 Steels

MAM steel parts exhibit unique microstructures because they are subjected to complex thermal cycles during MAM, see Fig. 16. The formation of metastable phases was reported in MAM processed steels. Conventional austenitic stainless steels typically exhibit a completely austenitic microstructure. However, the as-built SLM [105] and DED [56] processed AISI 316L samples showed small fractions of the δ-ferrite phase. It is attributed to the local increase in Cr-equivalent because of the segregation of Cr (ferrite stabilizer) to the cellular walls, which would shift the composition to the right in a dual-phase composition and favor small amounts of δ-ferrite precipitates. The SLM processed 2207 duplex stainless steel showed a fully ferritic microstructure with small amounts of austenite and nitrides (Cr_2N) at the grain boundaries. During solidification of duplex stainless steels, ferrite forms first and austenite forms subsequently during cooling. The rapid cooling in the SLM processing has completely suppressed the austenite transformation and resulted in a fully ferritic structure [127]. In an SLM processed martensitic stainless steel (AISI 420), a small amount of retained austenite ~ 2% was reported [128].

Several theories were proposed for the formation of retained austenite in steel parts during MAM, such as segregation of alloying elements to the cellular boundaries [129], solid-state diffusion of carbon during the reheating cycle [130], and solidification as γ-phase [131].

In the DED processed Ni-bearing maraging steel (18Ni-300 and Fe–19Ni–*x*Al), unique microstructures with cellular walls had retained austenite and the core of the cells with martensite (Fig. 17). The segregation of austenite stabilizing elements to the cellular walls was attributed to the presence of retained austenite [129, 132]. The SLM processed 17-4 PH martensitic stainless steel revealed a high fraction of

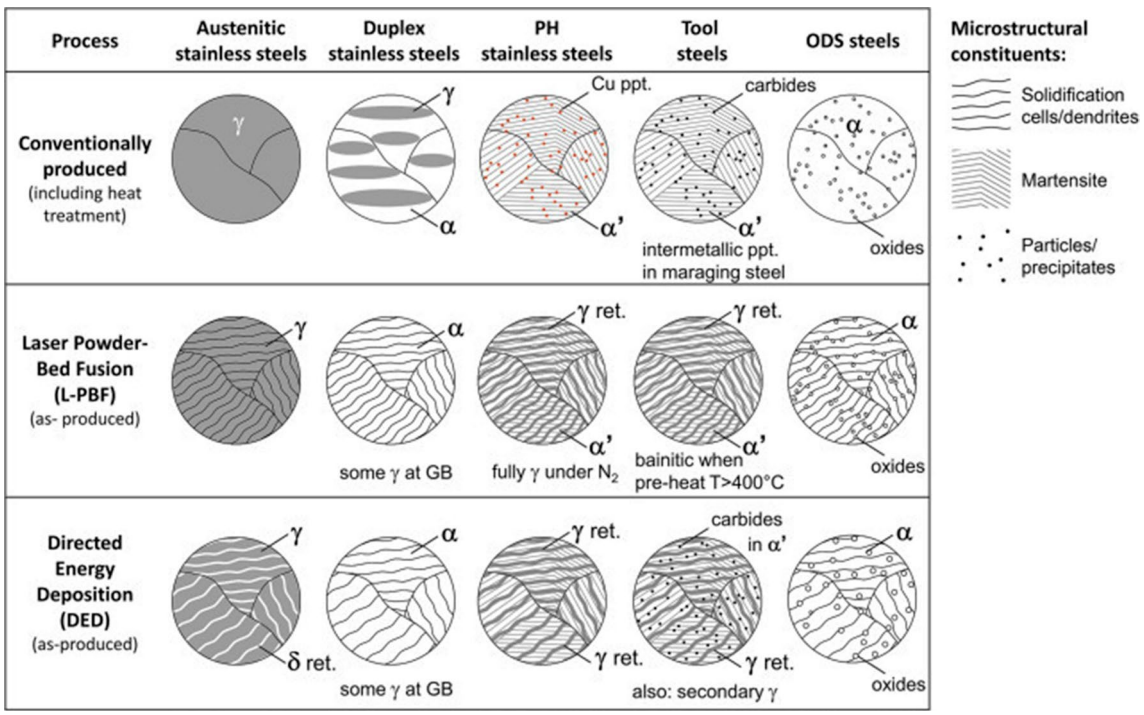

Fig. 16 Summary of typical microstructures of various steels produced by conventionally processing and by MAM [135]. Reproduced with permission from Elsevier

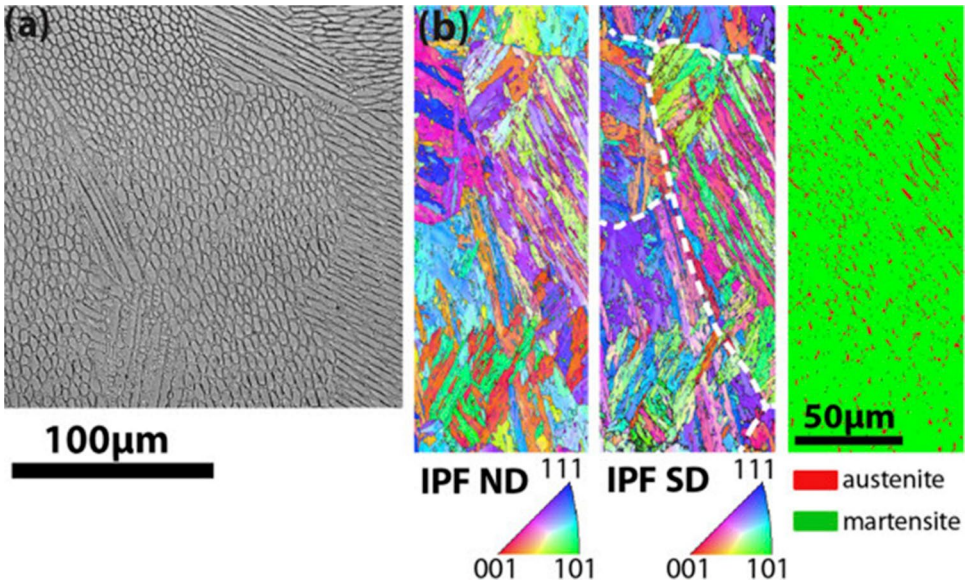

Fig. 17 Optical **a** and EBSD **b** micrographs of the as-built DED processed maraging steel (Fe-19Ni-*x*Al), showing the cellular/dendritic solidification structure and martensitic microstructure with the spatial distribution of austenite (red) around the cellular boundaries in both normal direction (ND) and laser scan direction (SD) [132]. Reproduced with permission from Elsevier. (Color figure online)

metastable austenite ~ 72% in the as-fabricated state, unlike the fully martensitic microstructure in the wrought processed specimen [133]. This was attributed to the segregation of austenite stabilizing element Ni to the growing solid–liquid interface, which would facilitate austenite formation at the late stages of solidification and it would also locally drop the M_f temperature to below room temperature. LeBrun et al. [134] also observed predominantly austenitic microstructures in 17-4 PH samples. The fine cellular structure and very high residual stresses in the SLM samples caused mechanical stabilization of the metastable austenitic phase.

Austenite reversion is another phenomenon reported in MAM steel parts. Holzweissig et al. [130] attributed this phenomenon to the quenching and partitioning (Q&P) process. The continuous heat flow during layer deposition would not allow the part to reach below M_f temperature, and some austenite remains untransformed. The solid-state diffusion of carbon from the supersaturated martensite into the austenite during reheating would result in austenite reversion [130]. In martensitic stainless steel AISI 420 produced by SLM, heterogeneous microstructures were reported with a fully martensitic structure on the top few layers and a high fraction of retained austenite (~ 58%) in the remaining bulk of the sample [136]. The multiple re-heating thermal cycles that the bulk of the sample experiences during part building between M_s and A_{c1} led to partitioning and diffusion of C from the supersaturated martensite to the phase interfaces (α'/α', α'/γ) and cellular boundaries. The carbon partitioning would cause austenite reversion and growth of retained austenite. The fully martensitic structure in the top few layers is because they experience less reheating cycles.

Although a large volume fraction of austenite in martensitic steels is not desirable because it lowers the overall strength, it has a beneficial effect on ductility via transformation-induced plasticity (TRIP). Facchini et al. [133] reported excellent strain hardening behavior in the as-built 17-4 PH martensitic stainless steel SLM samples. The presence of metastable austenite ~ 72% and martensite ~ 28% led to a two-stage strain hardening. The first stage of strain hardening is caused by the accumulation of stacking faults, and the second stage of strain hardening was dominated by twinning in both phases. The nucleation of martensite from the highly twinned austenite further contributed to the strain hardening of the as-built samples. In another work, the transitions in work hardening rates and enhanced ductility of the as-built and 900 °C heat-treated samples are attributed to the stress-induced transformation of the metastable austenite. The samples heat-treated at 1025 °C and 1150 °C did not show the transformation induced strengthening because the microstructure is predominantly martensitic [134].

The as-built high carbon tool steels (H13) samples showed ~ 19% retained austenite with fine carbides [137]. The segregation of the alloying elements (C, Co, Mo, and V) to the cellular walls stabilized the austenite at the cellular walls. Further, the authors reported relatively high secondary hardening temperatures (500–550 °C) in the SLM parts than the conventionally processed samples (450–500 °C). It was attributed to the presence of supersaturated austenite with most carbide forming elements. Similar observations were reported in other tool steels H11 [138] and M2 alloys [139]. Co-bearing maraging steel (Fe–18Ni–9Co–3.4Mo–1.2Ti) produced by SLM showed a martensitic matrix with some retained austenite and no precipitates. Upon aging at 480 °C/5 h, in addition to regular Mo- and Ti-rich Ni_3X precipitates, a μ-phase $(Fe, Ni, Co)_7Mo_6$ was reported. Austenite reversion was also observed around the retained austenite regions because of Ni partitioning [140].

In-situ tempering in MAM part fabrication was inevitable during the processing of high strength steels. Dilip et al. [43] reported auto-tempering in the SLM of high strength low alloy steel (HY100). The as-fabricated samples showed a fully martensitic structure with alternate layers of tempered martensite at the MPBs and untempered martensite within the melt pool. The high carbon equivalent of HY100 alloy results in a fully martensitic structure in the deposited layer. During a new layer deposition, at least a part of the previously deposited gets reheated to the high temperatures and gets auto tempered. Similar observations were reported in the SLM processed tool steels (H13) [137]. In Ni-bearing maraging steels (18Ni-300), the high cooling rates during SLM suppressed the formation of the strengthening precipitates Ni_3X (X = Ti, Mo, Al-rich) [129]. However, careful alloy design with Al above 3–5 at% formed Ni_3Al precipitates in the as-built samples [124], where the intrinsic heat treatment of the already deposited material because of the multiple reheating cycles would induce precipitation of fine Ni_3Al particles from the supersaturated matrix. Deirmina et al. [137] proposed *in-situ* low-temperature tempering of tool steel (H13) during the SLM and achieved high fracture toughness because of the absence of transition carbides (MC, M_2C, and M_6C carbides).

Krell et al. [131] reported preheating above the M_s temperature ~ 300 °C did not result in any microstructure difference in the SLM processed tool steel (H13) sample. The samples showed ~ 80% martensite and ~ 25% retained austenite with and without preheating. The segregation of alloying elements resulted in a local change in the M_s and M_f temperatures. Preheating at ~ 400 °C produced a full bainite microstructure [141]. The samples have responded well to the post-deposition heat treatment [131, 137, 142]. Post-deposition tempering at ~ 500 °C caused complete decomposition of the retained austenite and tempering of martensite. A slightly higher temperature tempering at ~ 600–700 °C eliminated the cellular structure. A fully martensitic structure was obtained by full austenitization followed by quenching.

Murr et al. [125] shown that the gas atomization environment and SLM cover gas (Ar or N_2 gas) have a strong influence on the phase transformation of the SLM processed 17-4 PH martensitic stainless steel. With Ar-cover gas, the as-fabricated SLM samples showed a fully martensitic microstructure. However, with N_2-cover gas, a high fraction of retained austenite ~ 85% was reported with N_2-atomized powders. The high thermal conductivity (40% greater than the Ar gas) and strong austenite stability of N_2 are proposed as responsible factors. In another work on SLM processed AISI 420, a small quantity of α-Fe and retained austenite γ were detected. This was attributed to the presence of high oxygen in the build chamber, which led to decarburization during SLM [48]. Wang et al. [82] reported lower tensile strength and elongation in the DED processed 304L samples compared to the annealed baseplate. This is attributed to the absence of strain-induced martensitic transformation during tensile testing in the DED samples. The higher nitrogen content in the gas-atomized powder stabilized the austenite phase in the DED samples, and no strain-induced martensitic transformation occurred during the tensile deformation.

4.5.2 High Entropy Alloys

The as-built SLM CoCrFeMnNi (called 'Cantor alloy') samples revealed epitaxial columnar grains with cellular sub-structure and high dislocation density. Interestingly, the as-built Cantor alloy samples also showed fine σ-phase particles and nano-twins (Fig. 18). Twins usually start forming in a deformed HEA alloy with true strain above 6%. However, this work reveals twins in as-built samples without plastic deformation. The high residual strain in the SLM parts and the low stacking fault energy of the CoCrFeMnNi (~ 29.7 ± 1.2 mJ/m^2) result in the formation of nano-twins in the as-built samples [143]. In another work, Mn-rich nano-oxides ~ 50 nm were reported in SLM processed CoCrFeMnNi [144]. The EBM processed CoCrFeMnNi samples showed relatively coarse columnar grains and cellular substructure with Mn and Ni segregations to the inter-dendritic regions [145]. CoCrFeNi SLM samples revealed a single-phase BCC structures with no elemental segregation [146]. The C-containing (1–2 at%) CoCrFeNi SLM samples showed uniform distribution of carbon in the matrix, and no carbides were reported [147]. However, in SLM processed as-built 1%C-Cantor alloy, $Cr_{23}C_6$-type carbides were reported at the cellular boundaries [148].

Karlsson et al. [149] compared the microstructures of the SLM processed and the induction melted AlCoCrFeNi HEAs. While both the samples show a combination of B2 and BCC phases, the microstructures were finer in the SLM samples with an average grain size of ~ 20 µm and BCC/B2 domain size 20–30 nm. The finer microstructure in the SLM samples was attributed to the faster cooling rates. In another work, in addition to the dual-phase microstructure, the as-built AlCoCrFeNi HEA SLM samples showed fine σ precipitates [150]. σ-phase was also reported in the as-built SLM CoCrFeMnNi HEA samples [143]. The presence of σ-phase was because of the multiple reheating cycle during the MAM part fabrication, which would reheat the material to the σ-phase formation temperature range (600–800 °C). Although the re-heating cycle periods are short, the high dislocation density in the material would accelerate diffusion and result in σ-phase formation in the as-built samples.

In AlCoCrFeNi HEA, while the as-cast samples showed B2/BCC phases, the EBM processed samples showed an additional FCC phase at the boundaries of the B2/BCC phases (Fig. 19) [151]. The high pre-heating temperature ~ 950 °C and reduced cooling rates during EBM

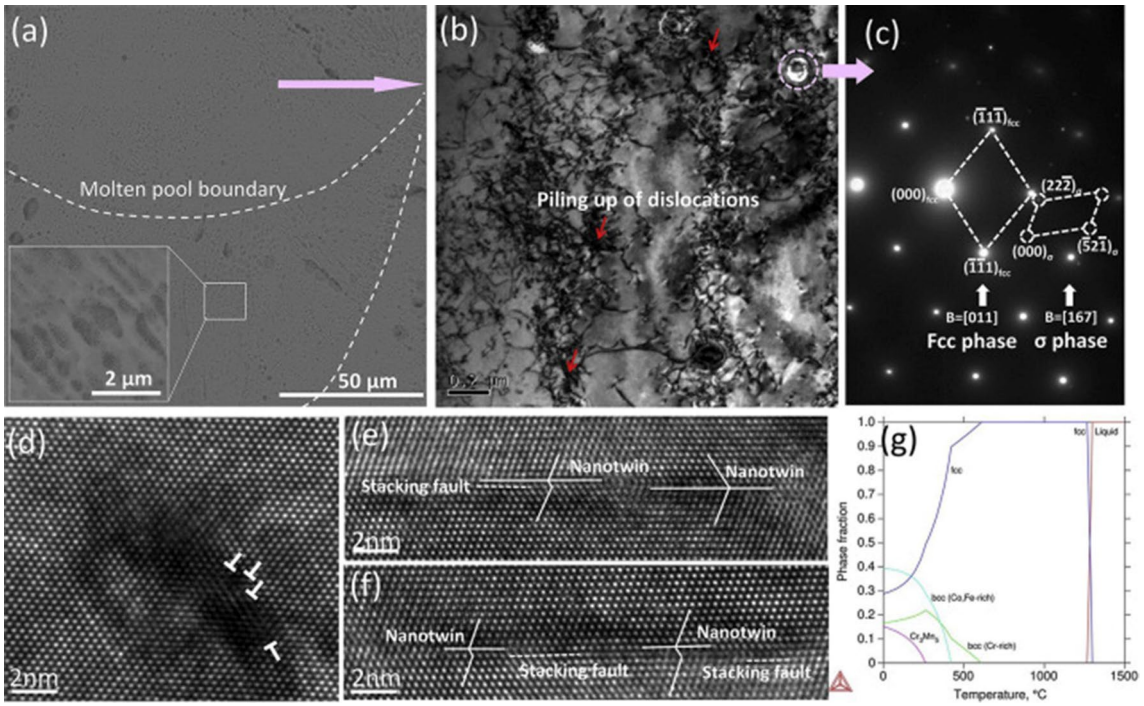

Fig. 18 Microstructures of the as-built SLM processed CoCrFeMnNi HEA. **a** SEM image showing sub-grain cellular structure. **b** TEM bright-field micrograph showing high dislocation density. **c** SAED pattern showing the existence of a $[011]_{fcc}//[167]_{\sigma}$ orientation relationship between the FCC phase and σ precipitate, **d** HR-TEM micrographs showing dislocations and **e**, **f** nano-twins with stacking faults. **g** Calculated equilibrium phase fractions of CoCrFeMnNi alloy [143]. Reproduced with permission from Elsevier

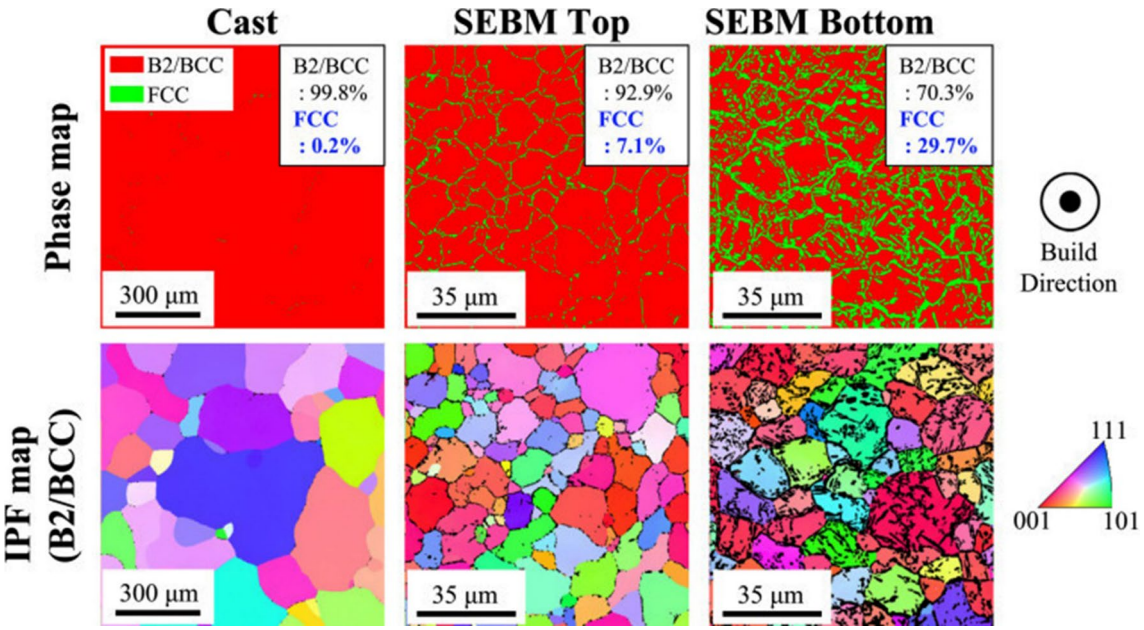

Fig. 19 Inverse pole figure (IPF) maps and phase maps of the cast processed and EBM processed AlCoCrFeNi samples [151]. Reproduced with permission from Elsevier

facilitated the FCC precipitation. Further, the authors have observed a difference in FCC volume fraction across the sample height. Close to the bottom of the sample, ~ 29.7% FCC phase, near the equilibrium volume percentage ~ 20%, was reported; however, the top regions showed only a ~ 7%

FCC phase. The long time above the preheat temperature resulted in more FCC phase in the bottom regions.

Fujieda et al. [80] has compared the microstructures of the CoCrFeNiTi HEA processed by the SLM and EBM processes. While the SLM samples presented a single FCC-phase, the EBM samples showed the FCC phase with fine intermetallic Ni_3Ti particles. Unlike the EBM samples, the absence of high-preheating temperature ~ 950 °C in the SLM samples resulted in rapid solidification and suppression of precipitation of Ni_3Ti intermetallic phase.

Cracking was reported in a few HEAs, AlCoCrFeNi [149], WTaMoNb [152], and CoCrFeNi [153], during SLM processing. Sun et al. [153] reported intergranular hot cracks throughout the builds. The cracking was attributed to the long columnar grains and high residual stress in the SLM samples. However, a few reports have shown successful MAM part fabrication without any cracking [146, 150]. Indeed, careful processing parameter optimization is the key to realize sound parts in high strength HEAs.

Kunce et al. [154] demonstrated that the cooling rate played a significant role in the phase transformation of the DED processed TiZrNbMoV HEA. The samples processed with a high laser power (1 kW) produced primary BCC structures, whereas that with low laser power (300 W) showed a two-phase structure composed of BCC and $NbTi_4$-type phases with some Zr-rich precipitates. The high cooling rate and associated supersaturation of the matrix with many alloying elements under the low laser power induced precipitation [154]. In the SLM processed CoCrFeMnNi HEA parts, an increase in energy density from 37 to 185 J/mm^3 reduced its lattice parameter because of the vaporization of volatile element Mn [143]. Reduced lattice parameters were also reported in the SLM processed AlCoCrFeNi HEA due to the vaporization of Al [150]. In the DED processed functionally graded $AlCrFeMoV_x$ samples, an increased solid-solubility (~ 18.5 at%) of V was reported. Further, even after a high-temperature heat treatment at 1100 °C for 30 min, the samples showed a single-phase BCC microstructure without any second-phase formation [67].

4.5.3 Titanium Alloys

Rapid solidification during MAM changes the microstructures of Ti–6Al–4V. While the conventional processed wrought Ti–6Al–4V samples had an equiaxed α + β microstructure at room temperature [155], the DED processed Ti–6Al–4V samples showed coarse prior-β columnar grains strongly oriented along the build direction. Depending on the cooling rate, which is predominantly affected by the process parameters, a basket-weave Widmanstatten α or acicular α or α′ martensite structure was observed. The grain boundary α-phase along the prior-β grain boundaries is also reported (Fig. 20a) [32, 156]. The microstructures of the SLM processed Ti–6Al–4V samples consisted of coarse prior-β columnar grains and acicular α or α′ martensite (Fig. 20b) [39, 102, 157]. The as-built Ti–6Al–4V EBM samples showed columnar prior-β grains with grain boundary α and near-equilibrium (α + β) structure having β-phase as discrete flat rods in the α phase [78, 158]. The high powder-bed temperatures above the M_s temperature (~ 575 °C) lead to the formation of near-equilibrium lamellar (α + β) instead of α′ martensitic structure as observed in the DED and SLM processed samples (Fig. 20c) [78, 95, 159].

The microstructural evolution in Ti–6Al–4V alloy starts with nucleation and growth of the prior-β grains. The slower cooling rate would facilitate the diffusional transformation of β to α, and a faster cooling rate would cause the diffusionless transformation to α′ martensite. If the powder-bed is preheated below the M_s temperature (M_s temperature ~ 800 °C and > 410 °C/s critical cooling rate), β-phase may transform diffusionless to α′ martensite and then transform diffusional to α + β microstructure during isothermal holding at the preheat temperature. If the pre-heat temperature is above the M_s temperature, β-phase may transform diffusional into α.

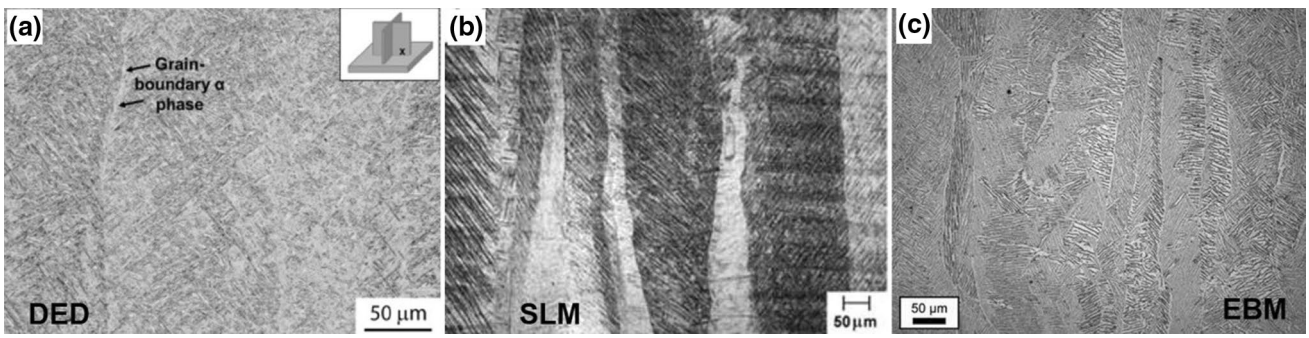

Fig. 20 Optical micrographs of the as-built Ti–6Al–4V fabricated by **a** DED [32], **b** SLM [39], and **c** EBM [78] processes. Reproduced with permission from Elsevier and Springer Nature

The EBM processed as-built β-Ti alloys, Ti–24Nb–4Zr–8Sn showed fine α-phase at the columnar β grain boundaries [160]. However, the parts produced by the SLM process showed a full β structure [161]. The high pre-heat temperature ~ 500 °C in EBM results in the α-precipitation. Full β microstructures were generated during SLM of Ti–6Al–4V with small additions of Mo (10%); it was attributed to the suppression of β to α transformation because of the lowered β-transus temperature to 900 °C [162].

The MAM processing parameters have a significant impact on the phase transformation in Ti and its alloy because of their allotropic behavior [163–168]. A lower scan speed (100 mm/s) in SLM of commercially pure Ti resulted in coarse α laths, and an increase in the scan speed to 400 mm/s formed fine α′ martensite. The higher cooling rates with the higher scan speed resulted in an α′ martensitic structure [169]. Xu et al. [170] demonstrated ultrafine lamellar (α + β) microstructure in the as-built SLM processed Ti–6Al–4V samples (Fig. 21). As discussed before, during layer deposition, the previously deposited material would get reheated to high temperatures, and the reheating temperature depends on the processing parameters used for deposition. The authors reported that with a smaller laser beam diameter (0 or 2), thinner layer thickness (~ 60 µm), and optimized energy density (50.62 J/mm^3), the previously deposited layer would reheat to ~ 400 °C. Reheating to ~ 400 °C would heat the previously deposited material to the α + β phase field, and result in *in-situ* decomposition of α′ martensite formed during solidification to ultrafine lamellar (α + β).

In another effort to understand the effect of SLM processing parameters on the *in-situ* decomposition of α′ martensite, Xu et al. [102, 170] reported that the short inter-layer time (~ 1 s) and larger samples dimension (> 4 mm) facilitate decomposition of α′ martensite to ultrafine lamellar (α + β) microstructure during part building. The attainment of the ultrafine lamellar (α + β) structure in the as-built SLM samples not only lead to superior properties but also eliminated the need for post-deposition heat treatment.

4.5.4 Aluminum Alloys

MAM of Al alloys is challenging and rather limited only to a few alloy compositions that are easy to cast. The majority of research is focused on eutectic Al–Si alloys, owing to its excellent castability and lower shrinkage due to the high fraction of Si particles [40, 171]. Although a few attempts to fabricate the part of high strength Al alloys, e.g., 2xxx series [37] and 7xxx series [75, 86], are made, the success is still limited because of the problem of hot cracking [172–174]. The limitations or difficulties in MAM of Al alloys include many, such as high laser reflectivity, low laser absorptivity, poor weldability, high solidification shrinkage, high thermal conductivity, the low viscosity of molten Al, and the presence of highly volatile alloying elements (Zn, Li, Mg) [175].

The high oxygen potential of Al alloys makes them react with oxygen very quickly. Therefore, during the processing of Al alloys, the build chamber oxygen content is maintained at the lowest level, possibly below 0.1 wt%, and processing is carried out in an inert gas atmosphere [175, 176]. The inter-gas type (Ar, N_2, He) used in the build chamber has a minimal effect on the microstructures of Al parts. However, He gas induced brittleness of the sample because of high porosity [176].

The supersaturation of the Al matrix with the solute elements has been observed in most laser processed Al alloys [37, 40, 41]. The maximum solubility of Si in Al is ~ 1.6 wt%; however, the SLM processed parts revealed a supersaturated Al matrix with ~ 7 wt% [40]. Dinda et al. [41] reported a more hypo-eutectic microstructure fraction in DED processed Al–11.3Si alloys. The inter-dendritic regions revealed fine-fibrous Si, unlike the equilibrium eutectic microstructure. These microstructures are attributed to the rapid cooling rates associated with the DED process, which allow less time for the coarsening of Si particles and increase the solid-solubility of Si in Al, which shifts the eutectic composition (~ 12.6 wt%) to higher Si concentrations. Similar observations were reported in as-built SLM

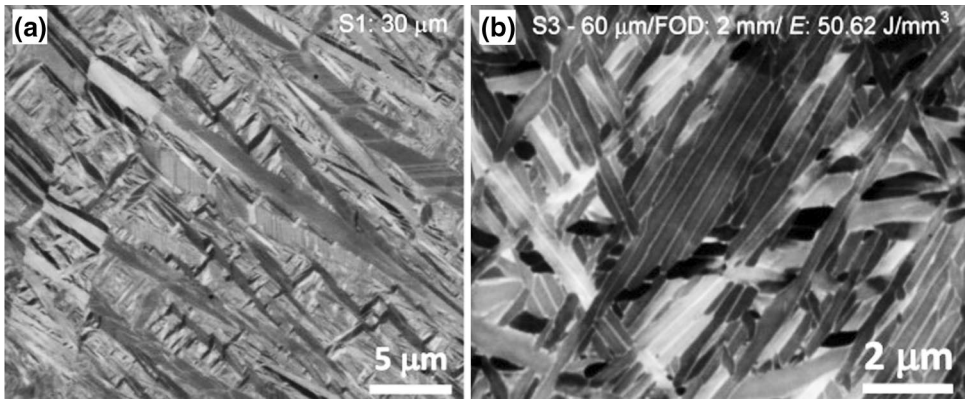

Fig. 21 SEM-BSE micrographs of the as-built Ti–6Al–4V SLM samples produced using varying parameters, **a** columnar prior-β grains with acicular α' martensitic structure, **b** Columnar prior-β grains with ultrafine lamellar (α + β) structure [170]. Reproduced with permission from Elsevier

Al–Cu–Mg alloy (AA2024) samples with extended solubility of Cu and Mg [37].

Most Al alloys have been reported to solidify with cellular-dendritic structure. In DED processed Al-10Si-Mg alloy, varying cell sizes were reported within a melt pool. The regions closer to the melt pool surface showed finer cell size (0.4 µm) and relatively coarse cells close to the MPBs (0.7 µm). These differences are attributed to the spatial difference in the growth rate (G) and thermal gradient (R) within the melt pool [38]. Further, the authors reported coarse Si particles devoid of cell structure below the MPBs, which was attributed to the HAZ effects in the previous layer. In another work on SLM of Al–12Si [171], a coarse cellular structure was reported at the MPBs compared to the bulk of the layer. Interestingly, even after the post-deposition heat treatment (500 °C for 6 h), the microstructure is still inhomogeneous with a higher number of larger Si-particles at the MPBs than the melt pool center. The lower ductility in the as-built and heat-treated samples was attributed to these coarse structures at the MPBs.

Talata et al. [177] studied the effect of specimen size on the microstructures of Al-10Si-Mg alloy and reported in-situ heat treatment of the Al matrix during SLM processing. While the grain size and texture were found independent of the sample dimension, the low angle grain boundary fraction and Si concentration in the Al matrix were dependent on sample dimensions. Thin samples ~ 0.3 mm thickness showed lower Si concentration and low angle grain boundary in the α-Al matrix than the centimeter-wide samples. Further, the thin samples, in addition to the coarse eutectic Si at the inter-dendritic regions, showed fine Si precipitates within the columnar grains. The reduced cooling rate and heat build-up in the thin samples, as it is sandwiched between loose powders, caused *in-situ* heat treatment and resulted in precipitation of fine Si particles from the supersaturated Al matrix.

The unique thermal history of MAM parts during part building results in heterogeneous precipitation of the second phase. In a recent attempt in processing and developing high strength Al parts using MAM, a new Sc-modified Al–Mg alloy (Scalmalloy) was attempted using SLM [178]. The as-built SLM samples showed a spatially heterogeneous grain structure with very fine equiaxed grains (150 nm–1 µm) at the melt pool boundaries and columnar grains in the center of the melt pool (2–5 µm), as shown in Fig. 22a, b. Further, the equiaxed grain regions revealed a high fraction of Al_3(Sc, Zr) and Al–Mg-oxides at the grain boundaries compared to the columnar regions, see Fig. 22c. From the thermal simulations, the authors reported a relatively lower temperature at the MPBs ~ 800 °C. At this temperature, both Al_3(Sc, Zr) and Al–Mg-oxides are stable and can act as inoculants during solidification, leading to the formation of equiaxed grains close to the MPBs. However, at the center of the melt pool, temperatures higher than 800 °C are reported, leading to the dissolution of Al_3(Sc, Zr) particles. While Al–Mg-oxides are stable at this temperature because of their less volume fraction and strong Marangoni convection in the melt pool, they could not promote heterogeneous nucleation, and columnar growth occurred.

Martin et al. [86] introduced lattice-matched nanoparticles (ZrH_2) as inoculants in high-strength Al alloys AA7075 and AA6061 to overcome the problem of hot cracking during SLM processing. The inoculants effectively refined the grain size and crack-free, equiaxed fine-grained microstructures with properties comparable to wrought materials were achieved (Fig. 23). The authors proposed that this approach can be universally applied to all non-weldable alloys and in all MAM processes. In another attempt, it was shown that the keyhole mode of melting is beneficial in reducing the solidification cracking in AA7050 SLM samples compared to the conduction mode. The deeper melt pools in the keyhole mode developed a heterogeneous grain structure with columnar and equiaxed grains, which generated an irregular path for the crack to propagate and, therefore, less density of cracks [75].

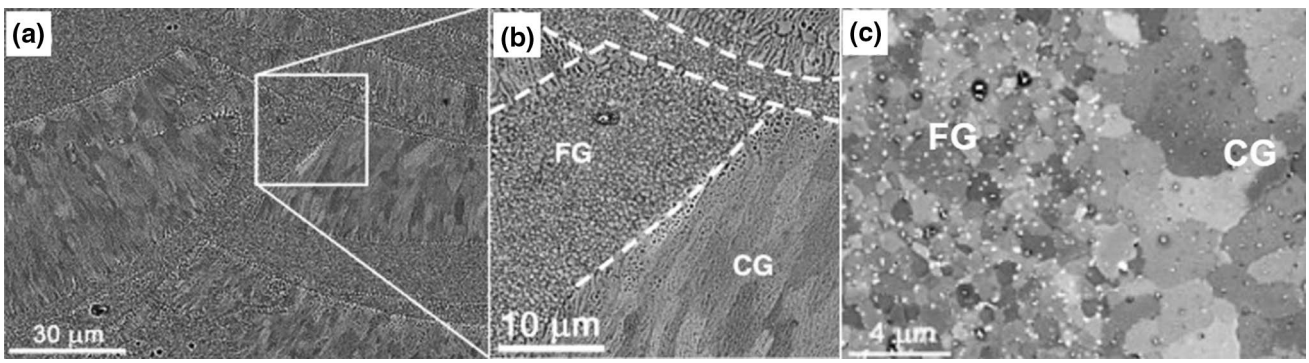

Fig. 22 **a–c** SEM-BSE micrographs taken at different magnifications close to the MPBs, showing heterogeneous grain structure in the SLM processed Sc-modified Al–Mg alloy [178]. Reproduced with permission from Elsevier

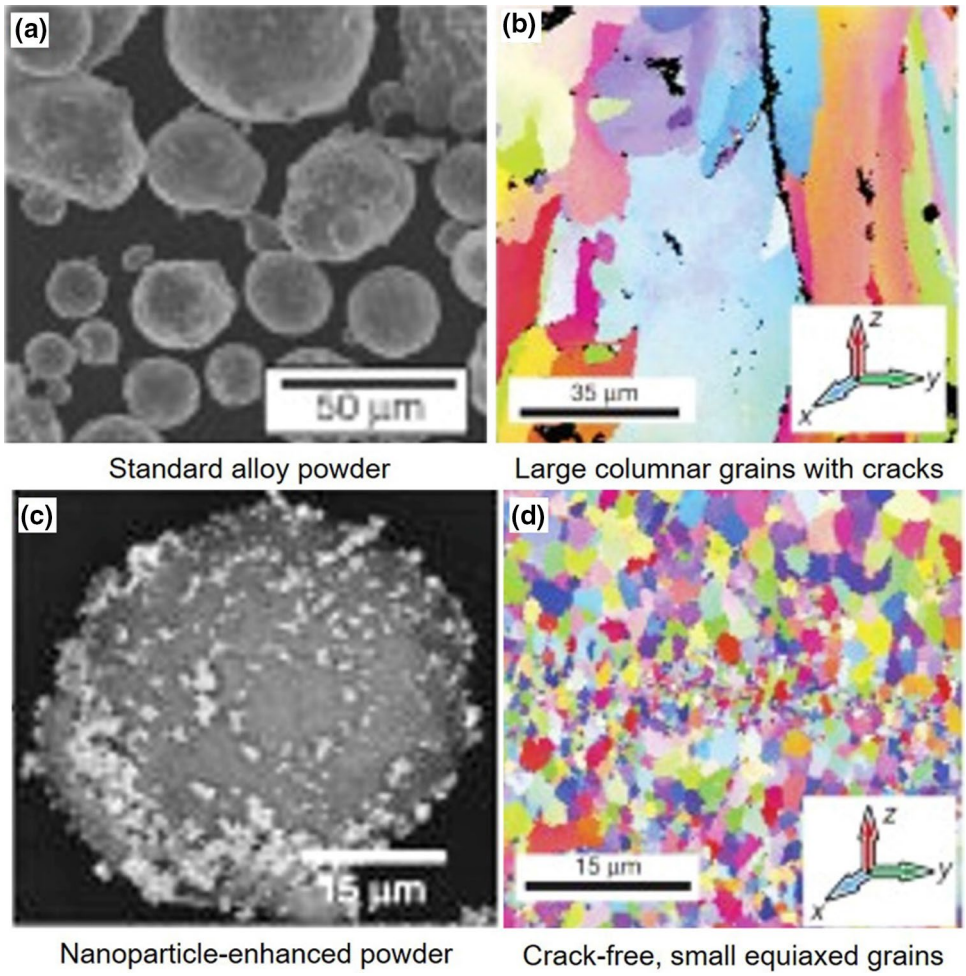

Fig. 23 SEM micrograph of powder feedstock, **a** AA7075 alloy and **c** AA7075 alloy functionalized with nano ZrH_2. EBSD micrographs of the SLM sample produced with **b** conventional and **d** functionalized powder feedstocks [86]. Reproduced with permission from Springer Nature

4.6 Oxide Formation

The primary source for the oxide inclusions in the MAM parts was identified as the large oxide inclusions present in the precursor powder. The dissolution/re-precipitation of these oxide inclusions during MAM processing results in nano-scale inclusions in the MAM parts [179]. Ramirez et al. [180] used low purity high-oxygen containing Cu powder with ~ 99.5% purity. The EBM processed samples showed a unique Cu_2O precipitation and dislocation architecture within the columnar grains, which led to an increase in hardness by 54% compared to the wrought pure Cu. In the SLM processed 316L SS, Li et al. [181] showed that the parts produced using gas-atomized powders showed lower oxides, higher density, and superior mechanical properties when compared to the water-atomized powder. The spherical morphology and the lower oxygen content in the gas atomized powder increased the wettability and packing density leading to higher densification behavior.

It is speculated that the fine oxides in the SLM and DED samples could be due to the reaction of high oxygen-affinity elements in the material with the atomic oxygen present in the build chamber. Most MAM parts might have some fractions of oxide inclusions, but only a few report them; some examples include Si- and Mn-rich oxides in 316L [182, 183], TiO_2 in maraging steels [184], Fe_3O_4 in Invar36 [185], and Mn_2O_3 in CoCrFeMnNi HEA [144]. In SLM processed 316L SS [179], an increase in the build chamber oxygen level to ~ 1% increases the fraction of oxides in part. The authors attributed it to the remelting of the oxidized spattered powder particles during a new layer deposition, as shown in Fig. 24. In SLM processed 316L [107], the local oxidation of active elements Si yielded spherical nano-oxides of Cr-containing silicates. To study the effect of alloying elements on the oxide inclusions, Deng et al. [179] used 316L powders with no high oxidizing elements, Si and Mn, for SLM part fabrication. Although Si and Mn oxides are not present in the SLM part, Cr and Fe rich oxides were observed. Therefore, irrespective of the elements present, if the build chamber oxygen content is not controlled, the presence of oxides persists. Processes like EBM, which take place under vacuum, may not be influenced by the atmospheric oxygen. Nevertheless, the purity of the precursor powder needs to be considered [180].

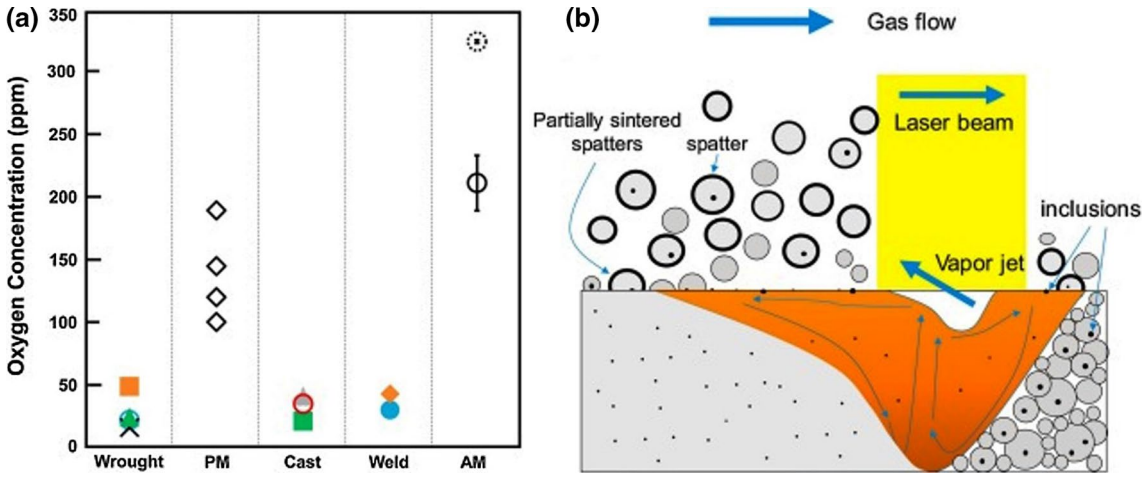

Fig. 24 **a** Comparison of oxygen concentration in the final products with different processing techniques. **b** Schematic showing the interaction between environmental oxygen and melt pool, resulting in oxide inclusion [179]. Reproduced with permission from Elsevier

Likewise, the storage of the powder feedstock can be a source of moisture in the powder feedstock. Elemental powders, which are highly susceptible to oxidation, such as Ti and Al, need to be stored in a vacuum or inert and dry atmosphere. The moisture in the powder feedstock can decompose during powder/beam interaction and releases hydrogen and oxygen. The presence of hydrogen can cause problems such as hydrogen embrittlement in high-strength steels and porosity in aluminum alloys. To study the effect of humidity on the oxide inclusion formation, Deng et al. [179] exposed 316L powders to a high humidity environment before SLM processing. The powder flowability degraded significantly, and the parts showed a high volume fraction of oxide inclusions and lower yield strength.

The oxide layer on the powder precursor surface can also be a source for oxide inclusions in the MAM parts. In the case of 316L SS, the oxide layer on the powder surface has shown a little contribution to the oxide inclusion formation [179]. However, the oxide layer on the pure Fe powder influenced porosity and densification. It increased the CO_2 laser absorptivity and greatly affected the surface tension with decreased wetting angle, causing melt pool agglomeration and porosity [186]. MAM powders demand tight controls not only in residual gases but also in trace elements. Small variations in trace elements, such as S, O, and Si, changed the melt pool dynamics and surface tension [179, 186]. Fine sulfide inclusions (~50 nm in size) were reported in the DED processed 304L SS [83]. High-quality powder feedstock with a controlled specification is required to obtain sound MAM parts without any inconsistency [187].

In SLM processed 316L SS, metastable Rhodonite nanoscale oxides ($MnSiO_3$) were reported in the as-built samples. The metastable oxides converted to stable $MnCr_2O_4$ Spinel particles during heat treatment at 1200 °C and acted as Zener-pinning particles and retarded grain growth during high-temperature heat treatment [183]. The oxides can be useful in promoting new phases morphologies and nucleating new phases. For instance, in low-alloy steels, the presence of oxides resulted in acicular ferrite [188]. In titanium alloys, oxygen is an effective solid-solution strengthener [189]. Therefore, greater control of oxygen content is required throughout the process for realizing consistent mechanical properties across the parts.

In 316L stainless steel, Cr-containing silicate non-oxide inclusions ~ 50 nm with a volume fraction of ~ 6 vol% was reported. The samples showed improved mechanical properties than oxide-dispersion strengthened 316L stainless steel [190]. In the DED processed 316L SS, Smith et al. [83] have estimated the contribution of oxide inclusion on the tensile strength. An Orowan strengthening model, Eq. (14), was used to describe the contribution to strength due to these oxide inclusions. Assuming oxide inclusions maintain an incoherent interface with the matrix and dislocations cannot bypass these obstacles by the shearing mechanism. Instead, they bow around the obstacle to proceed deformation, enhancing strength $\Delta\sigma_y$.

$$\Delta\sigma_y = M\frac{0.4Gb}{\pi\sqrt{1-\nu}}\frac{\ln\left(\frac{2\bar{r}_c}{b}\right)}{\lambda}, \tag{14}$$

where shear modulus (G), Burgers vector (b), mean orientation factor (M), and Poisson ratio (ν). λ describes the average spacing of inclusions $\lambda = 2\bar{r}_c\left(\sqrt{\frac{\pi}{4f}} - 1\right)$, mean radius $\bar{r}_c$ of a random cross-section $\bar{r}_c = \sqrt{\frac{2}{3}}r$, r is the mean radius of the precipitates, and volume fraction (f).

The oxide inclusions are reported to contribute marginally and are less effective in strengthening because of their relatively larger diameter (30–100 nm), less volume fraction, and larger spacing between oxide particles [83, 183]. In the as-built SLM processed 316L SS, silicates (Si, Mn oxides) in the size range of ~ 10–150 nm have a negligible contribution to strengthening [191].

4.7 Texture

The origin of texture in the MAM parts is due to the directional solidification within the melt pool [51, 73, 192]. When a layer of material is deposited, because the crystal structure and the composition of the melt pool are similar to the already deposited layer, grains grow spontaneously from the partially melted grains at the MPB without any nucleation barrier. The grain growth direction is a function of the solidification front and temperature gradient. The solidification front is always perpendicular to the MPB, and the temperature gradient is either perpendicular or radial to the build direction based on the melt pool shape. These conditions create a morphological texture, with elongated columnar grains either aligned towards the build direction or slanted towards the melt pool center. The crystallographic texture accompanies the morphological texture, in which columnar grains would favor growing along the easy growth direction (Table 1). The combination of crystallographic and morphological textures during solidification would result in texture in the MAM parts. The easy growth direction for cubic systems <100> is approximately parallel to build direction. Therefore, most cubic materials show <100> fiber texture along the build direction [37].

The melt pool shape strongly affects the texture in MAM parts. In DED processed Fe-23Mn-Al alloy, <110> fiber texture was reported in the build directions. The deep and curved melt pool led to vertical columnar grains from the bottom and ~ 25° inclined grains from the sides of the melt pool. These microstructures resulted in a <110> texture, unlike the most favorable <100> direction in the cubic systems. [45]. A similar <110> texture was demonstrated by Sun et al. [76] in 316L SLM parts by changing the melt pool shape using an appropriate scan strategy and hatch spacing. In recent work on SLM of 316 SS, a unique crystallographic lamellar texture with <100> and <110> was reported along the build direction. The shallow melt pool with conduction mode resulted in crystallographic lamellar <100> and <110> texture, and a deeper melt pool with keyhole mode resulted in a single crystalline-like <110> texture (Fig. 25) [51].

The presence of <110> texture was also reported in SLMed CoCrMo [193] and SLMed stainless steel 316L [76]. In the as-built SLM processed CoCrMo alloy, <110> texture was seen only in the top few layers, and a predominant <100> texture was reported in the bulk of the sample. Suggesting that <110> texture forms during solidification, subsequent layer deposition without any laser rotation led to preferential growth along the <100> direction [193]. The processing parameters and the thermophysical properties of the material significantly affect the melt pool shape, heat flow direction, and solidification rate. Therefore, the reported intensity of the texture varies considerably from work to work [129]. In the SLM processed AlCoCrFeNi HEA alloy, Niu et al. [150] have shown <001> texture at lower energy density (~ 68 J/mm^3), and it gradually transformed into the <111> crystallographic direction with an increase in the energy density (~ 111 J/mm^3). The transition of the texture was attributed to the formation of a deeper melt pool at higher energy density. In Al-12Si alloy, while lowering the hatch spacing and layer thickness intensify the texture, a bidirectional laser scan path with a 90° laser rotation for each layer weakens the cubic texture along the building direction [38]. The SLM processed 316 SS produced with high heat input (1000 W laser power) showed a coarse grain structure with strong <100> texture; in contrast, the samples produced with lower heat input (400 W laser power) had a fine-grained structure with weak texture along the build direction [194]. Strategies to increase the nucleation rate and promote equiaxed grains by adding inoculates are found effective in weakening the texture in Al alloys, Al–Cu–Mg + Zr [85], Al–Mg–Zr + Sc [195], AA-7075 + Si [84], and AA-7075 + Zr [86], and in Ti alloys, Ti–Mo + B [196] and Ti–6Al–4V + Cu [197].

The solid-state phase transformation during cooling would affect the texture. In Ni-bearing maraging steel, during solidification, austenite grains form preferably along the <100> direction. However, during subsequent solid-state phase transformation, the austenite grains transform to martensite through several possible crystallographic orientations, resulting in a random texture. The retained austenite in the samples still shows <10> texture [198, 199]. Similar observations were also reported in high carbon tool steels (H13) [200].

Compared to the SLM and DED processed materials, the EBM processed samples exhibited high texture intensity [159]. The EBM processed as-built CoCrFeNiTi samples showed higher texture intensity than the SLM samples. The high preheating temperatures (~ 950 °C) in the EBM process greatly reduces the temperature gradient during solidification and promotes preferential columnar growth, resulting in a microstructure with long columnar grains in the build direction with a strong <100> texture [80]. The EBM processed CoCrFeMnNi alloy also showed similar microstructures with columnar grains a few millimeters in length and a strong <100> texture [145]. In the SLM processed CoCrFeMnNi HEA, single track deposits showed fine columnar grains and <100> texture; however,

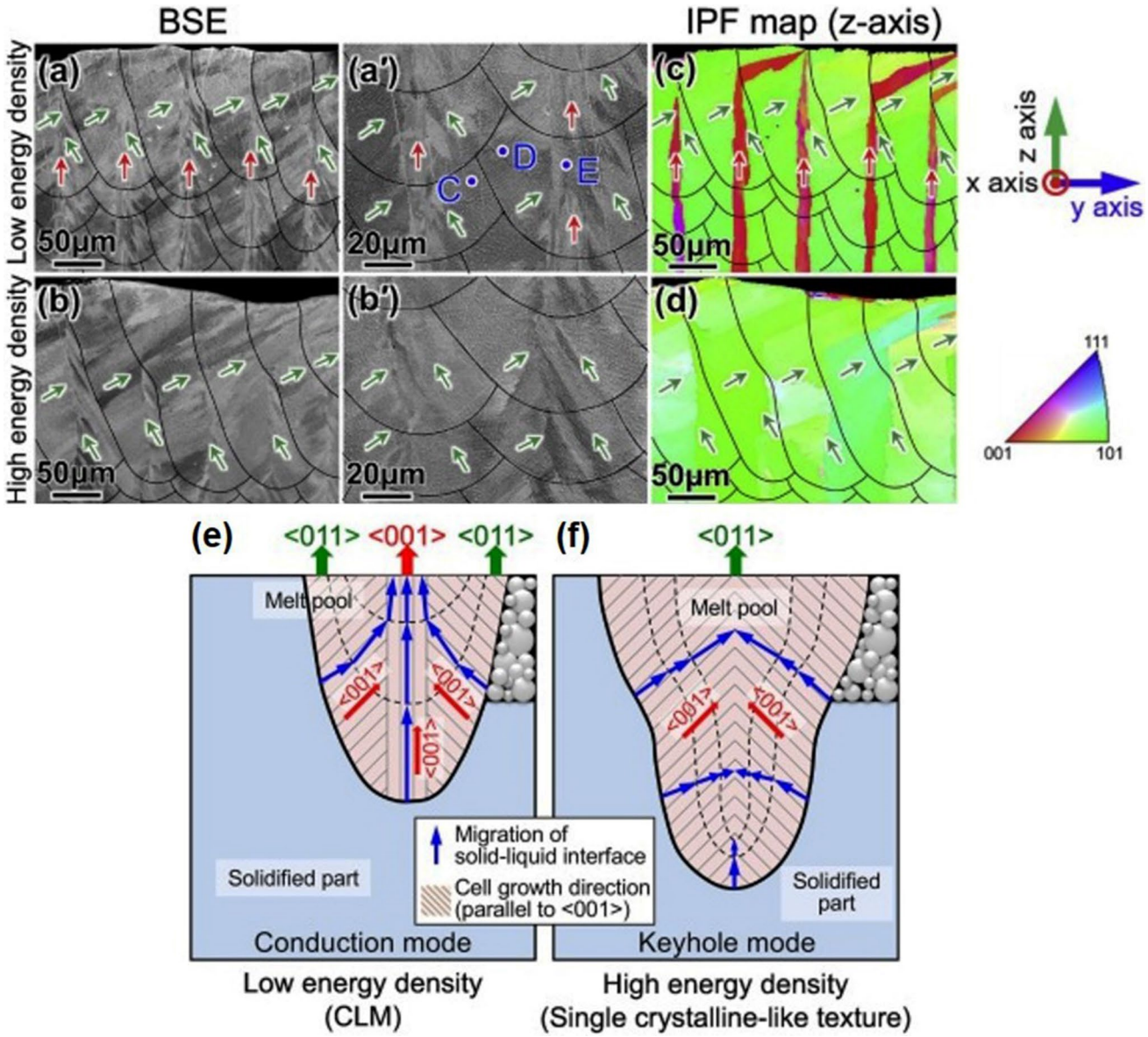

Fig. 25 **a**, **b** SEM-BSE micrographs show the shape of the MPBs and the columnar grains in the specimens produced with low energy density (**a**, **a′**, **c**), and high energy density (**b**, **b′**, **d**). Schematic illustration showing the growth direction of the solid–liquid interface during solidification under low energy density conduction mode **e**, and high energy density keyhole mode **f** [51]. Reproduced under the terms of the Creative Common License

multi-layer deposits showed relatively coarse columnar grains with <100> and <110> texture. The multiple re-melting cycles in the multi-layer deposits facilitate competitive growth and varied textures [201].

In a recent study, Sun et al. [76] demonstrated an approach to achieve high strength and ductility in as-built 316L SLM samples by modifying the crystallographic texture from <001> to <110> directions. As <110> oriented grains promote twinning, the samples showed higher strain hardening rates and superior mechanical properties. In another work, Sun et al. [51] demonstrated a crystallographic lamellar texture with <100> and <110> . The boundaries between the <100> and <110> oriented grains effectively hindered the dislocation motion and resulted in an excellent combination of strength and ductility (Fig. 25).

The studies on the crystallographic texture of the post-heat treated samples are rare. Takata et al. [202] compared the texture of the Al-10Si-Mg in the as-built and solution-treated conditions. Besides the difference in sub-structure (recovery effects), no significant differences in terms of grain shape, morphology, and texture were reported [202]. The HIP treatment does not alter the <001> texture in the

as-built SLM processed CoCrFeMnNi samples because the columnar grains remain unchanged [143].

4.8 Residual Stress

During MAM, the manufactured parts experience unique thermal cycles involving (1) rapid heating with steep thermal gradients due to the use of a high energy density source (laser or electron beam), (2) rapid cooling with high solidification rates because the melt pool volume is very small, and (3) re-melting during new layer deposition. These thermal cycles are experienced in a localized region, resulting in high shrinkage stresses, because the adjacent un-melted regions restrict the shrinkage of solidifying material. Further, it also results in an uneven distribution of inelastic strain because of the heterogeneity in local thermal expansion and contraction of the material [203, 204]. The localized melting with high shrinkage stresses, and heterogeneous inelastic strain, are reported as the primary sources of residual stresses in MAM parts. The source of residual stresses in the MAM parts is similar to multi-pass fusion welds [205]. However, the inherent strain fields are more complicated in MAM part because it consists of a large number of melt-passes. The factors that influence the residual stress in MAM parts are shown in Fig. 26 [206].

The residual stresses are classified into three categories according to the scale at which they occur: Type I macro-residual stress, type II mesoscale residual stress, and type III micro-scale residual stress. Type-I residual stresses significantly influence the material properties, and any change in the equilibrium would result in a change in part dimensions. Most destructive type residual stress measuring techniques are designed to measure type I residual stress [207].

The residual stresses in MAM parts are studied by numerical simulations, as well as experimental techniques. In SLM processed 316L, Mercelis and Kruth [208] measured the type I residual stresses for the samples before and after removal from the base plate using a crack compliance method and an X-ray diffraction method. The parts that are connected to the base plate showed a very high residual stress close to its yield strength. However, much lower residual stresses were reported in the samples after removal from the base plate. Yadroitsev et al. [204] reported higher tensile residual stresses along the laser scanning direction using numerical simulations and X-ray diffraction. Further, the residual stresses were shown to vary across the sample height, with the regions closer to the build platform showed the highest residual stresses than on the top surface. In SLM processed AISI 300 maraging steel, the maximum tensile stress of ~ 0.7 yield stress was reported near the free surface (0.1 mm hole depth), and a sharp drop in tensile residual stress by ~ 85% was reported at a depth 0.5 mm from the free surface [209]. The heterogeneous residual stress distribution in the SLM parts is attributed to the heterogeneous shrinkage associated with the rapid cooling rates and steep temperature gradients.

The sample height, stiffness of the material, and base plate thickness affect the magnitude of the residual stress significantly. In the SLM processed Ti–6Al–4V and IN718, the central region of the samples showed compressive residual stress, and the free edges of the samples showed high tensile residual stress [210]. Similarly, in the SLM processed 316L, a heterogeneous residual stress distribution was reported across the length of the sample. The top and bottom sections of the sample showed tensile residual stress, whereas the center portion of the sample showed compressive residual stresses [208]. The difference in the heat dissipation for the samples closer to the center and at the ends or edges generates a different residual stress pattern.

MAM processing parameters significantly affect the residual stresses. The samples built with smaller scan vector 3 mm × 3 mm islands showed lower tensile residual stresses than the samples produced with bigger scan vector 5 mm × 5

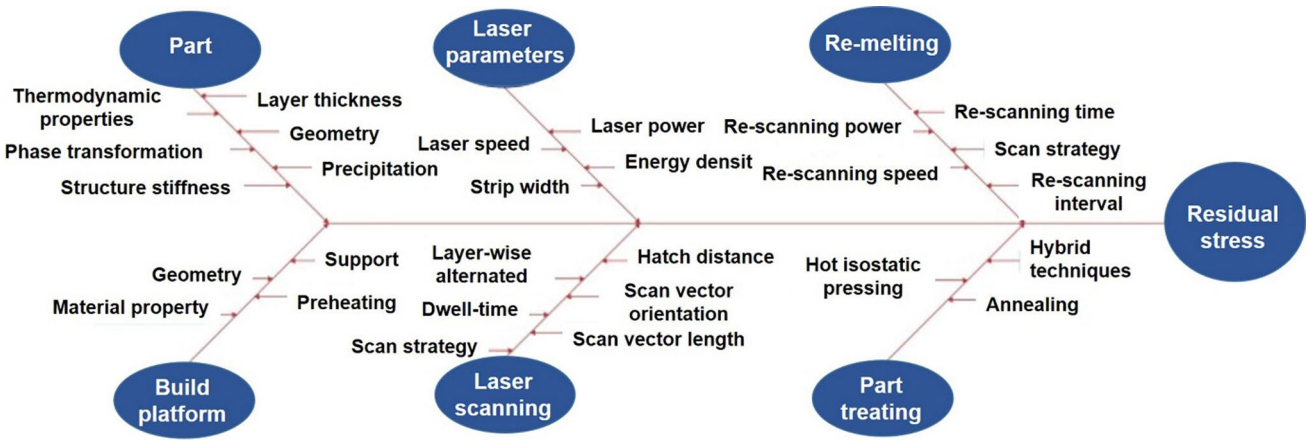

Fig. 26 The factors that influence the residual stress during SLM processing [206]. Reproduced with permission from Elsevier

mm islands. The laser rotation by 45° affected the in-plane residual stresses; however, axial residual stresses remain unchanged [211]. Similar observations were also reported in as-built SLM processed IN718 samples. Further, it was shown that the samples produced with higher energy density have lower residual stresses because it lowers the cooling rate [212]. Mishurova et al. [213] have studied the effect of the SLM process parameters on the sub-surface residual stresses in Ti–6Al–4V. Small hatch spacing ~ 40 µm reduced the sub-surface residual stress from ~ 600 to ~ 150 MPa, because of the higher heat buildup and slower cooling rates. Further, it was shown that the porosity level < 1% has a negligible influence on the subsurface residual stresses.

In another work on DED processed IN718, the hatch spacing, which determines the adjacent track overlap area, strongly influences the residual stress generation. The overlap regions showed higher residual stresses compared to the rest of the melt-pool. An increase in the overlap area to ~ 50% increased the residual stress [214]. Liu et al. [215] studied the effect of energy input and shorter scanning vector length on the residual stress evolution in different build directions using X-ray diffraction-based measurements. Relatively, higher tensile residual stresses are reported along the laser scanning direction compared to the build direction. Further, the magnitude of residual stresses at the free edges is reduced with lower energy input and shorter scanning vector length.

The high thermal strain signifies lower printability of the alloy as the material experiences higher distortion. Mukherjee et al. [31] have calculated the thermal strain of several engineering materials and showed that alloy Ti–6Al–4V suffers higher thermal distortion than the other materials studied because of its lower thermal diffusivity and density (Fig. 27). Further, with sample height (number of deposited layers), the thermal strain increased irrespective of the alloy system. In DED processed thin-walled hollow and solid samples of H13 steel, a very low tensile residual stresses (~ 0.5 yield stress) was measured along the build direction, and compressive residual stresses were measured perpendicular to the build direction. The austenite to martensite transformation led to reduced residual stresses [216].

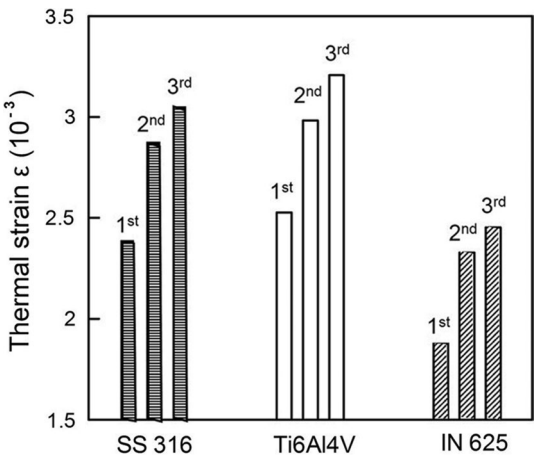

Fig. 27 Variation of maximum thermal strain with the increase in the number of deposited layers during SLM fabrication of SS316, Ti–6Al–4V, and IN625 materials [31]. Reproduced under the terms of the Creative Common License

Several approaches have been proposed to lower the residual stresses in MAM parts. Preheating is one of the strategies used to control residual stress. Preheating the bed to 550 °C was shown to reduce the residual stresses by 46% in SLM of Ti–6Al–4V [217]. Heating above 570 °C eliminated the residual stresses and improved the mechanical properties because of the decomposition of α′-martensite to equilibrium α + β microstructure [218]. In the as-built SLM processed H13 tool steel samples, compressive residual stresses ~ − 324 MPa without preheating and tensile stresses ~ 371 MPa with preheating at 400 °C were reported. The variation in residual stress pattern with preheating is due to the presence of the martensitic structure in the former and bainitic structure in the later [141]. The EBM processed samples showed lower residual stress than the SLM and DED samples because of high powder-bed preheat temperatures [219]. Although preheating reduces the residual stresses, it affected the microstructures and mechanical properties in some cases [220, 221]. Therefore, approaches, e.g., laser shot pinning [222] and ultrasonic shot pinning [223] as post-MAM processes, were instrumental in changing the surface tensile residual stress to compressive to depths exceeding 1 mm.

4.9 Anisotropy

Most studies report the reasons for mechanical anisotropy in the MAM parts to, heterogeneous microstructures [32, 43, 157], epitaxial grain orientation [29, 32, 88, 224], processing defects [34, 44, 225], and texture [29, 34, 88].

The tensile properties of the MAM parts typically show lower strength and ductility along the build direction compared to the other two spatial directions. In SLM processed 316L, the samples tested in the build direction showed lower tensile properties and strain hardening rate compared to the samples tested perpendicular to the build direction (Fig. 28) [88]. In the build direction samples, the epitaxial columnar grains are oriented parallel to the loading axis. Therefore, the dislocation motion is along the longer dimension of the grain, as shown in Fig. 28d. However, in the samples tested perpendicular to the build direction, since the grains are oriented perpendicular to the loading direction, the dislocation motion is along the shorter dimension of the grain Fig. 28c. Therefore, higher grain boundary strengthening in the samples tested perpendicular to the build direction. The strain

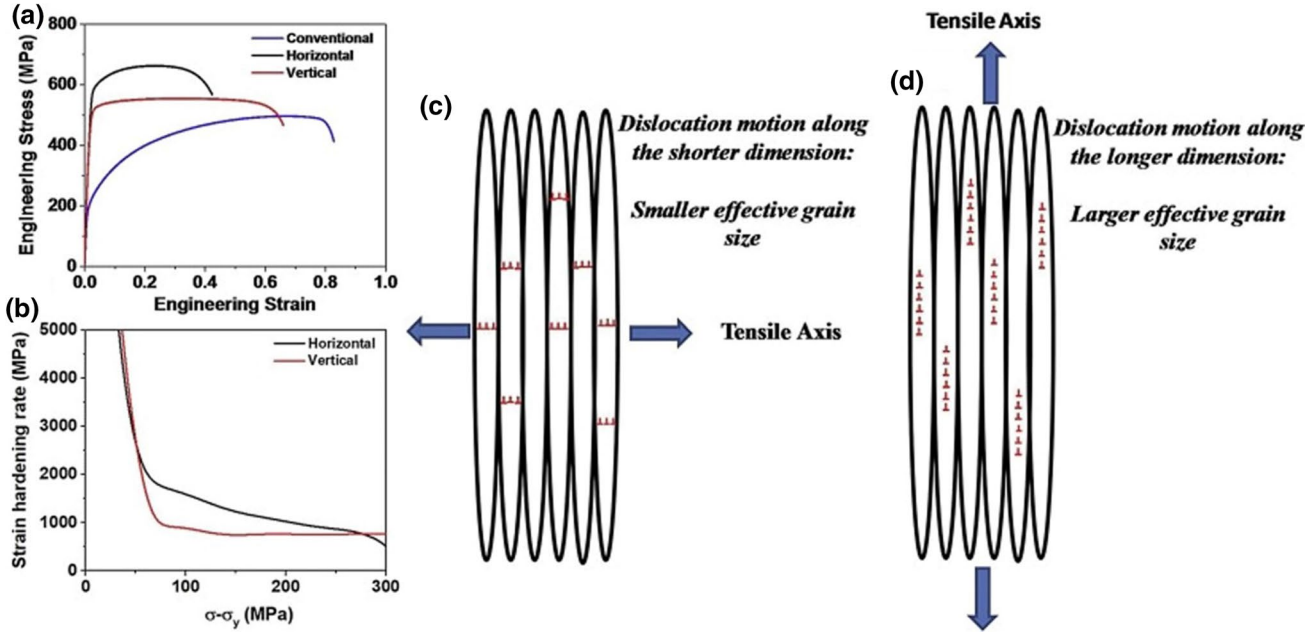

Fig. 28 Typical tensile stress–strain **a** and strain hardening rate curves **b** of the SLM processed 316L SS in different build directions. Schematic showing the variation in dislocation motion within the columnar grains depending upon the loading axis, **c** samples tested perpendicular to the build direction, **d** samples tested along the build direction [88]. Reproduced with permission from Elsevier

hardening difference between the samples is attributed to the texture differences (Fig. 28b). The presence of <111> texture in the horizontal build sample has promoted twinning and higher strain hardening.

Similar observations with lower tensile strength and higher ductility along the build direction are reported in SLM processed Ti–6Al–4V [32] and Co–Cr–Mo alloys [224]. Recently, the anisotropy in tensile properties of the SLM processed C-$(CoCrFeMnNi)_{99}$ HEA is attributed to the grain structure and texture. At the early stages of plastic deformation, the anisotropy is from the grain structure (size and morphology) differences across the build directions. At the late stages of plastic deformation, the increase in the strain hardening rate in the Y direction sample was attributed to the <110> crystallographic texture, which changed the deformation mode from slip to twinning [29].

The MAM process type also affects anisotropic behavior. Kok et al. [16], in their recent review, noted that the EBM and DED processed Ti–6Al–4V samples exhibited no yield strength anisotropy. However, the SLM processed Ti–6Al–4V samples showed higher yield strength anisotropy between the different build orientations because of the smaller melt pools and higher temperature gradients. The higher ductility in the EBM samples compared to the SLM [157] and DED [32] processed Ti–6Al–4V samples was attributed to the presence of equilibrium α + β microstructure in the former and brittle α′ martensite in the latter.

The microstructural heterogeneities within the MAM part also result in anisotropy. In the EBM processed Ti–6Al–4V parts, the top few layers of the samples showed brittle α′ martensitic microstructure, whereas the bulk of the sample showed equilibrium α + β microstructure. Therefore the samples tested close to the top surface showed very low ductility than the bulk [158]. Smith et al. [83] studied the effects of tensile specimen location and orientation on the yield strength in the DED processed 316L. The distance from the baseplate showed a more significant role in the yield strength anisotropy than the specimen orientation. In the SLM processed high strength low alloy steel HY100, interestingly, the samples tested along the build direction showed higher elongation than in the laser scan direction [43]. The elongation difference was attributed to the orientation of the auto-tempered layer at the MPBs to the loading axis. In the vertical build samples, the soft auto-tempered regions are oriented perpendicular to the loading direction and deform independently. In the horizontal built specimens, the soft auto-tempered regions are oriented parallel to the loading direction and are constrained by harder martensite, so lower elongation. The specimen size dependency on the anisotropy was investigated in the SLM processed Al-10Si-Mg alloy [177]. The samples with a smaller width of ~ 0.3 mm reported lower hardness ~ 107 HV than the centimeter size samples ~ 120 HV. The difference in cooling rates, and the solid-solution hardening of the Al matrix, are attributed to the hardness difference. In the thin samples, as the loose powder surrounds both sides during SLM processing, it dramatically reduces the cooling rate, and results in heat build-up and *in-situ* precipitation of Si particles from the

supersaturated Al matrix, leading to the softening of the matrix.

In another work, the anisotropy in the as-built Al–10Si–Mg alloy SLM samples was attributed to the MPBs fraction and orientation to the loading direction [44]. In the horizontal build samples, because the fraction of MPBs is lower than the vertical build samples, they showed higher strength and ductility [44]. The authors feature the MPBs as the weakest regions in the SLM parts because of the inhomogeneous microstructure and processing defects at the MPBs. Shifeng et al. [34] reported that the MPBs are one of the main reasons for the anisotropy and low ductility in SLM parts. The preferential presence of defects and heterogeneous microstructures at the MPBs significantly affects the plastic deformation and fracture mode in 316L SS [225]. While processing parameter optimization to overcome the defects is an ongoing work, post-deposition treatments, e.g., HIP processing, effectively reduce the processing defects in the MAM parts [157].

4.10 Post-processing

The post-deposition heat treatments have been carried out either to improve the mechanical properties of the parts, to relieve the residual stress, or to close the internal defects such as porosity and cracks. In many alloy systems such as high-strength steels, Ni-base superalloys, precipitation-hardenable alloys, a post-deposition heat treatment is a mandatory step to achieve the desired properties. Therefore, understanding how the heterogeneous microstructures in the MAM parts influence the post-heat treatment microstructure would help fine-tune the mechanical properties.

In SLM processed pure iron samples, stress-relieving heat treatment at 640 °C for 2.5 h followed by furnace cooling (FC) resulted in a fully recrystallized microstructure. Although the SLM processed samples did not undergo any cold working, the likely driving force for the recrystallization (RX) is attributed to the presence of residual stress in the as-fabricated samples [226]. The SLM processed IN718 heat-treated at 1160 °C for 4 h, followed by furnace cooling, revealed a partially recrystallized microstructure with a heterogeneous grain structure [227]. In another work by Cho et al. [214] in DED processed IN718, post-deposition heat-treatment at 1100 °C for various times, showed grain nucleation from the overlap regions, and the samples with a higher overlap area ~ 50% showed a finer and more evenly distributed RX grains compared to lower overlap area samples. The above difference in the RX is attributed to the different residual stress levels with different overlap areas. The overlap regions showed higher residual stresses compared to the rest of the melt-pool.

Brandl et al. [49] noted recrystallization in wire-fed DED processed Ti–6Al–4V samples during solution treatment (ST) above the β-transus temperature (1200 °C/2 h/FC). The ST samples showed a fully recrystallized microstructure with equiaxed prior β-grains decorated by grain boundary α and α-colonies (Fig. 29). In the EBM processed Ti–6Al–4V, solution treatment just at the β transus temperature (1030 °C/2 h/AC) revealed semi-equiaxed β grains with some grain boundary α and finer α colonies. Although the residual stresses in EBM samples are relatively low, they show recrystallization [219]. Therefore, the driving force for the RX in the MAM may not be entirely from the residual stress in the samples. No recrystallization but some coarsening of as-built α + β microstructure was reported in HIP processed (915 °C/2 h/100 MPa) Ti–6Al–4V EBM samples. Interestingly, the authors reported recrystallization in the mechanically strained EBM samples [228]. The EBM processed IN718 did not show recrystallization during ST (1066 °C/1 h/argon quench) and after HIP (1200 °C/4 h/120 MPa) [229]. Significant grain coarsening is reported during the standard HIP cycle (1120 °C/4 h/100 MPa) in EBM processed IN718 [230]. Whether RX precedes the observed grain growth in the above samples is not clear.

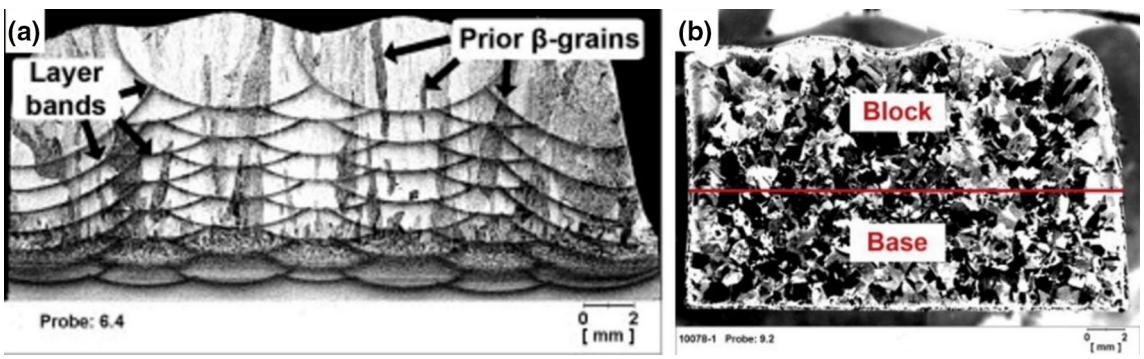

Fig. 29 Optical microstructures of the wire-fed DED processed Ti–6Al–4V sample in **a** as-built and **b** heat-treated (1200 °C/2 h/FC) [49]. Reproduced with permission from Elsevier

The standard post-processing procedures used for wrought or cast samples may not be ideal for MAM processed alloys because of their unique microstructures, such as segregation at the cellular walls, high dislocation density, coarse columnar grains, and supersaturated matrix. The kinetics in MAM parts can be different compared to the conventionally processed equiaxed or heavily deformed microstructures. Consequently, an optimized heat treatment cycle needs to be derived for MAM parts to achieve the desired microstructures and properties.

Smith et al. [231] observed a different annealing behavior in DED deposited 304L and forged 304L parts. In the forged 304L, the onset of RX occurred at ~ 727 °C/30 min and completed at ~ 950 °C/30 min. In comparison, in the DED 304L sample, the onset and completion of RX were delayed to ~ 950 °C/30 min and ~ 1075 °C/30 min, respectively. Further, the forged 304L samples showed decreases in dislocation density and hardness with annealing temperature. However, in the DED samples, the dislocation density did not reduce until the onset of RX, and after that, it behaved similarly to the forged samples. It was concluded that the presence of cellular structure with Cr segregation to the cellular walls and higher N content in the DED processed 304L has effectively increased the temperature required to RX when compared with forged 304L. Vrancken et al. [232] proposed an optimum heat treatment to improve the ductility of as-built Ti–6Al–4V SLM parts (presence of α′ martensitic microstructure). Heat treating below the β transus (995 °C) ~ 850 °C/2 h followed by furnace cooling resulted in a columnar β-grains with fine lamellar (α + β). Xu et al. [170] has shown a near-complete α′ martensite decomposition to very fine (α + β) at temperatures as low as ~ 400 °C/2 h.

The post-deposition heat treatment of duplex stainless steel S31803 SLM samples is shown to recover to the desired duplex austenite/ferrite microstructure partially in the range of 900–1200 °C. Maximum γ-fraction (~ 24%) is obtained with heat treatment at 1000 °C for 5 min [233]. Saeidi et al. [105] conducted post-deposition heat treatment of 316L SS at various temperatures for 6 min, followed by furnace cooling. While the as-built samples showed coarse columnar grains (10–100 µm) with cellular structure (0.5 µm) and Mo segregation to the cell walls, the samples heat-treated above 1100 °C revealed a dual-phase structure with austenite grains and fine acicular ferrite. The formation of the acicular ferrite was attributed to a local increase in Cr-equivalent because of the segregation of ferrite stabilizers and the presence of a small amount of BCC ferrite in the as-built sample, which would have acted as a nucleation site for the ferrite during post-heat treatment. In contrast, the post-deposition heat-treated (1150 °C/2 h/AC) DEDed 316L samples revealed a fully austenitic microstructure, while the as-built samples showed a ferrite fraction ~ 10% [56].

In the SLM processed Al-12Si alloy, a post solution heat treatment at 500 °C has removed the heterogeneous interdendritic Al-Si eutectic microstructures and showed uniform precipitation of Si particles (Fig. 30). The supersaturated Al matrix in the as-built samples with ~ 7 wt% Si has dropped rapidly to ~ 2 wt% upon solution treatment after just 15 min and to ~ 1.6 wt% an equilibrium concentration after 30 min. The brief solution treatment at 500 °C for 30 min helped realize very high ductility ~ 25%. The presence of numerous dislocations and boundaries (nano-sized Si particles and ultrafine Al matrix) in the as-built samples have substantially enhanced the diffusivity and benefit in faster precipitation and growth of Si particles [40].

In another work on SLM processed IN718, STA heat treatment (960 °C/1 h/AC) below the δ-solvus temperature developed a fully RXed microstructure with coarse grains at the MPBs [47]. These coarse-grained MPBs were devoid of δ-phase. This phenomenon is attributed to the non-uniform distribution of Nb in the samples. Since the δ-solvus temperature is proportional to the Nb concentration, the regions closer to the MPBs with lower Nb content showed complete dissolution of δ and grain coarsening. Post-deposition heat treatment was considered mandatory for SLM processed high strength low alloy steel HY100 because it developed a unique microstructure with alternate layers of tempered and untempered martensite [43]. While direct tempering resulted in over tempering of the already tempered regions, quench (900 °C/1 h/water quench) and temper (620 °C/2 h/furnace cooling) heat treatment resulted in the homogeneous tempered martensitic microstructure similar to a conventionally processed material. Similar observations were reported in the SLM processed tool steel H13 [137].

The as-fabricated SLM processed 17-4 PH martensitic stainless steel did not respond to direct aging treatment because of a higher fraction of retained austenite in the samples, which has higher solubility of precipitating element Cu. The solution treated and aged samples showed uniform precipitation of Cu and improved mechanical properties [134]. In SLM processed tool steel H13, the cellular structure completely disappeared with tempering above 600 °C, and a fully martensitic microstructure without any retained austenite was obtained with austenitization followed by quenching and tempering at 400 °C. Further, the direct tempered samples showed secondary hardening at a relatively high temperature because of supersaturated retained austenite with carbide forming elements (C, Cr, Mo). The fully austenitized and tempered samples showed secondary hardening at the same temperature as the conventional alloy [137, 141].

HIPing is one of the widely used post-deposition techniques to relieve stress and to reduce any processing defects such as remaining porosity and cracks. Ti–6Al–4V parts HIP processed at 920 °C for 4 h, at a pressure of 103 MPa

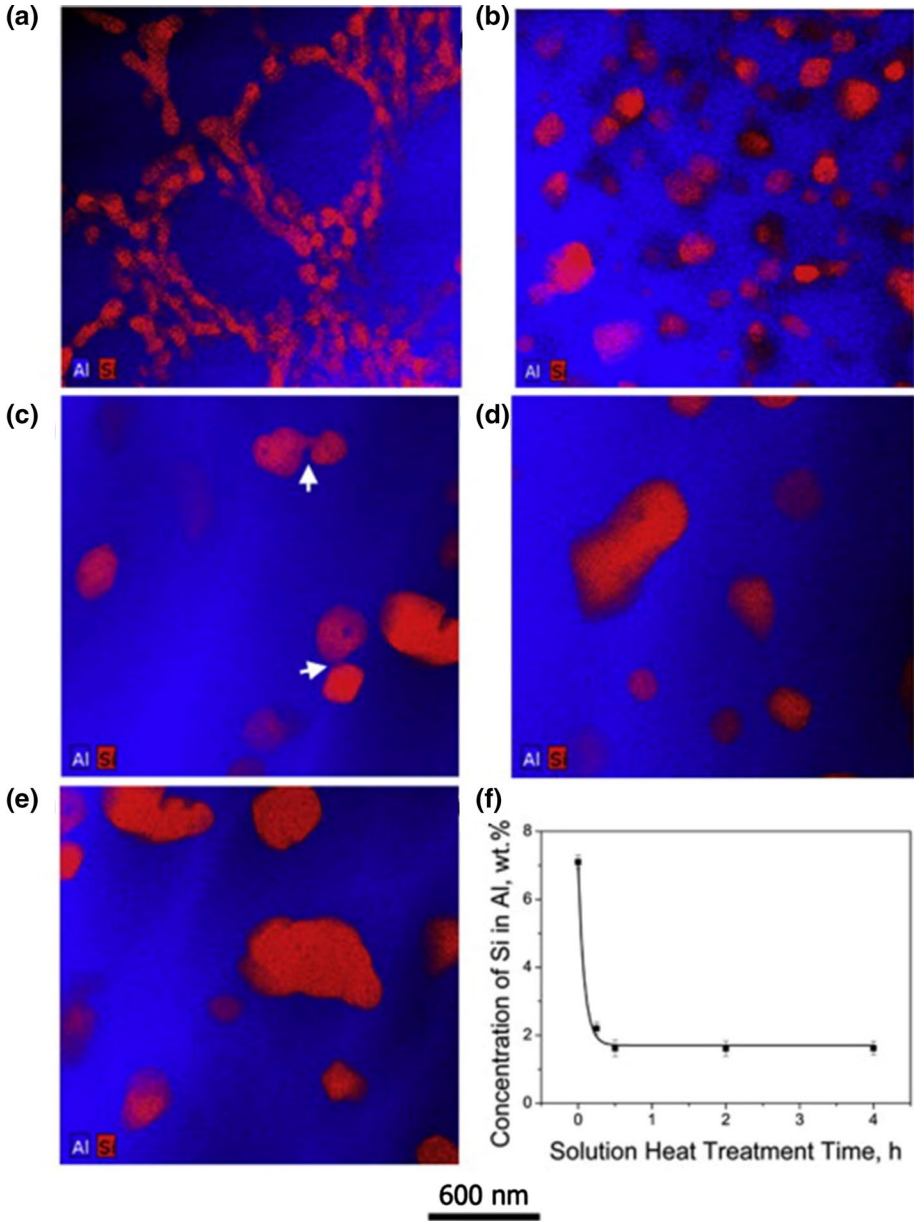

Fig. 30 TEM-EDS maps of the Al (blue) and Si (red) distributions in the Al–12Si alloy in the as-built condition **a**, and after solution treatment at 500 °C for 15 min **b**, 30 min **c**, 2 h **d**, and **e** 4 h. **f** Si concentration in Al with varying solution heat treatment times [40]. Reproduced with permission from Elsevier. (Color figure online)

showed the complete transformation of α′ martensite to coarse equilibrium (α + β) microstructures with α-lath thickness ~ 4 µm. The columnar prior-β grains are still present in the samples, and the porosity fraction was significantly reduced after HIPing. The SLM processed IN718 samples showed a fully RX microstructure after HIPing at 1160 °C for 3 h, at a pressure of 100 MPa pressure. Interestingly, the post-HIP processed SLM samples revealed a finer grain structure compared to the wrought processed HIP samples. It was speculated that the undissolved fine oxides or carbides in the SLM samples would have inhibited grain growth during HIPing [234]. Processing high strength Ni-base superalloys, CM247LC with high Al content, is a challenge because they are highly susceptible to ductility-dip cracking and solidification cracking during SLM. The precipitation of γ′ in the previous layers during the reheating cycle is inevitable and results in a drastic drop in ductility and cracking. Post-deposition HIPing of the samples effectively eliminated the micro-cracks generated during SLM processing [235].

In SLM processed maraging steels (18Ni-300), a modified heat treatment cycle from the recommend cycle (6 h at 490 °C) offered an optimal strength-ductility combination. Optimal strength (YS > 1900 MPa) was realized by aging at 490 °C for 8 h, and an excellent combination of strength (YS > 1700 MPa) and ductility (~ 10%) was realized with a 525 °C aging for 8 h [236]. Post-deposition heat treatment of the EBM processed Ti–6Al–4V significantly improved the ductility with a marginal strength drop. Heat treatment

at 920 °C for 2 h followed by air cooling led to an increase in ductility by 25%, whereas heat treatment at 1030 °C resulted in a 125% increase in ductility [237].

5 Summary and Future Direction

This review summarizes the scientific understanding of the microstructural aspect for most studied engineering materials developed with various MAM processes. The microstructures of MAM parts are significantly different from those of the conventional cast processed parts. These differences include the presence of several MPBs, heterogeneous grain structure with competitive epitaxial columnar grains and equiaxed grains, fine sub-grain cellular structures with cell walls segregated with alloying elements and decorated with dislocations, very high dislocation density similar to that of a severely plastic deformed material, supersaturated matrix with extended solute solubility and refined second-phases (in size, distribution, and fraction), metastable phases and fine nano-scale oxides, in-situ heat-treated microstructures, and high residual stresses. The primary reason for the unique microstructures in the MAM parts is the complex thermal history they experience during part fabrication, involving rapid heating and cooling rates, high solidification rates and temperature gradients, multiple reheating cycles, and heterogeneous heat transfer. Therefore, treating the MAM microstructures as homogeneous is not appropriate for understanding the behavior of MAM parts.

The MPBs are considered the weakest regions in MAM parts because of the presence of heterogeneous microstructures and processing defects [34, 44, 55]. A great deal of work needs to be carried out in developing processing maps by sustainable models. Various approaches to strengthen the MPBs through post-processing need to be established.

The MAM parts are characterized by heterogeneous grain structures with competitively grown long epitaxial columnar grains and equiaxed grains. The typical columnar grain structure in the MAM parts is due to the high thermal gradients and absence of the constitutive undercooling zone at the growth front [62]. Tailoring the grain structure in MAM parts is an important research direction, e.g., alloy design with higher solute content to achieve constitutive undercooling, the addition of inoculates to achieve heterogeneous nucleation, and mechanical attenuation using ultrasound to break the growing dendrites [238].

The sub-grain cellular structures with the cell walls segregated with alloying elements and dislocations are unique microstructures of MAM parts. This unique cellular structure is considered the primary contributor to enhanced mechanical properties in MAM parts [89, 110]. The origin of the sub-grain cellular structure is still a debatable subject and needs to be established to utilize the cellular structures effectively. Numerical simulations and models considering the aspects of crystal structure, solidification phenomena, MAM thermal history, and residual stresses would be of great help.

The supersaturated matrix with higher solute solubility is another unique microstructural aspect in MAM parts. It helps remove a solution annealing heat treatment step because the parts responded well to direct aging [119–121]. Also, the in-situ heat treatment of the previously deposited layer initiates fine precipitation from the supersaturated matrix during part fabrication and reduces the overall aging time and temperature [115]. The matrix supersaturation has refined the equilibrium second-phases significantly and improved the mechanical properties [30, 40]. These impressive attributes of the MAM parts can be effectively utilized by careful alloy design with an increased fraction of the precipitate forming elements to facilitate direct aging.

The complex thermal cycles during MAM affects the phase transformation and result in unique microstructures. In particular, it would result in metastable phases [129, 132] and new phases [140] with the heterogeneous distribution. The presence of these microstructures would affect the mechanical property. Optimizing the post-deposition heat treatment cycles for MAM parts and alloy design considering the MAM process cycles is the need of the hour.

Residual stress and anisotropy in MAM parts continue to be serious problems during the processing of high strength material. Standardized approaches and models to lower the residual stresses and anisotropy need to be established. Post-deposition heat treatment cycles used for cast and wrought alloys cannot be directly applied to MAM parts as the kinetics in MAM parts are different [232, 239]. Recrystallization is a known phenomenon in wrought processed materials; however, the recrystallization and grain growth during the post-deposition heat treatments of the MAM parts are not clearly understood yet [214, 226–230]. Detailed investigations in these directions are required.

Acknowledgements This work was supported by Fundamental Research Program "Development of High Performance Materials and Processes for Metal 3D Printing (PNK5520)" of the Korean Institute of Materials Science (KIMS), and by the Creative Materials Discovery Program of the National Research Foundation of Korea (NRF) funded by the Ministry of Science and ICT (2016M3D1A1023384 and 2017R1A2A1A18069427). This work was also supported by Korea Atomic Energy Research Institute (20171510102030). Dr. G.M. Karthik is supported by the Korea Research Fellowship Program through the National Research Foundation of Korea (NRF) funded by the Ministry of Science and ICT (2019H1D3A1A01102866). The authors acknowledge the contribution of Dr. Praveen Sathiyamoorthi at POSTECH.

References

1. ISO/ASTM52900, *Standard Terminology for Additive Manufacturing – General Principles – Terminology*, ASTM International, (West Conshohocken, PA 2015)
2. N. Guo, M.C. Leu, Front. Mech. Eng. **8**, 215–243 (2013)
3. T. Catts, *GE turns to 3D printers for plane parts,* https://www.bloomberg.com/news/articles/2013-11-27/general-electric-turns-to-3d-printers-for-plane-parts (2013)
4. J.Y. Lee, J. An, C.K. Chua, Appl. Mater. Today **7**, 120–133 (2017)
5. E. Atzeni, A. Salmi, Int. J. Adv. Manuf. Tech. **62**, 1147–1155 (2012)
6. A. Koptyug, L.-E. Rännar, M. Bäckström, S. Fager Franzén, P. Dérand, Int. J. Life Sci. **3**, 15–24 (2013)
7. T. DebRoy, T. Mukherjee, J.O. Milewski, J.W. Elmer, B. Ribic, J.J. Blecher, W. Zhang, Nat. Mater. **18**, 1026–1032 (2019)
8. W.J. Sames, F.A. List, S. Pannala, R.R. Dehoff, S.S. Babu, Int. Mater. Rev. **61**, 315–360 (2016)
9. M.Q. Zafar, H. Zhao, Met. Mater. Int. **26**, 564–585 (2019)
10. B.E. Stucker, G.D. Janaki Ram, *Materials Processing Handbook* (CRC Press, Boca Raton, 2007).
11. S. Palanivel, H. Sidhar, R.S. Mishra, JOM **67**, 616–621 (2015)
12. G.M. Karthik, S. Panikar, G.D.J. Ram, R.S. Kottada, Mater. Sci. Eng. A **679**, 193–203 (2017)
13. G.M. Karthik, G.D.J. Ram, R.S. Kottada, Mater. Sci. Eng. A **653**, 71–83 (2016)
14. I. Gibson, D.W. Rosen, B. Stucker, *Additive Manufacturing Technologies* (Springer, New York, 2014).
15. V.K. Nadimpalli, G.M. Karthik, G.D. Janakiram, P.B. Nagy, Int. J. Adv. Manuf. **108**, 1793–1810 (2020)
16. Y. Kok, X.P. Tan, P. Wang, M.L.S. Nai, N.H. Loh, E. Liu, S.B. Tor, Mater. Des. **139**, 565–586 (2018)
17. R.R. Mudge, N.R. Wald, Weld. J. **86**, 44–48 (2007)
18. M.L. Griffith, D.L. Keicher, J. Romero, C. Atwood, L. Harwell, D. Greene, J. Smugeresky *Laser Engineered Net Shaping (LENS) for the fabrication of metallic components*, Sandia National Labs, Albuquerque, New Mexico, USA (1996)
19. H. Dobbelstein, E.L. Gurevich, E.P. George, A. Ostendorf, G. Laplanche, Addit. Manuf. **25**, 252–262 (2019)
20. S. Lee, J. Kim, D.-S. Shim, S.-H. Park, Y.S. Choi, Met. Mater. Int. **26**, 708–718 (2020)
21. J.P. Kruth, X. Wang, T. Laoui, L. Froyen, Assembly Autom. **23**, 357–371 (2003)
22. Y. Zhang, J. Li, S. Che, Y. Tian, Met. Mater. Int. **26**, 783–792 (2020)
23. T. Pasang, A. Kirchner, U. Jehring, M. Aziziderouei, Y. Tao, C.P. Jiang, J.C. Wang, I.S. Aisyah, Met. Mater. Int. **25**, 1278–1286 (2019)
24. W. Cong, F. Ning, Int. J. Mach. Tool. Manu. **121**, 61–69 (2017)
25. C. Han, Q. Fang, Y. Shi, S.B. Tor, C.K. Chua, K. Zhou, Adv. Mater. **32**, e1903855 (2020)
26. M. Galati, L. Iuliano, Addit. Manuf. **19**, 1–20 (2018)
27. Y. Zhu, K. Ameyama, P.M. Anderson, I.J. Beyerlein, H. Gao, H.S. Kim, E. Lavernia, S. Mathaudhu, H. Mughrabi, R.O. Ritchie, N. Tsuji, X. Zhang, X. Wu, Mater. Res. Lett. **9**, 1–31 (2021)
28. X.L. Wu, Y.T. Zhu, Mater. Res. Lett. **5**, 527–532 (2017)
29. J.M. Park, J. Choe, H.K. Park, S. Son, J. Jung, T.-S. Kim, J.-H. Yu, J.G. Kim, H.S. Kim, Addit. Manuf. **35**, 101333 (2020)
30. G.M. Karthik, P. Sathiyamoorthi, A. Zargaran, J.M. Park, P. Asghari-Rad, S. Son, S.H. Park, H.S. Kim, Materialia **13**, 100861 (2020)
31. T. Mukherjee, J.S. Zuback, A. De, T. DebRoy, Sci. Rep. **6**, 19717 (2016)
32. B.E. Carroll, T.A. Palmer, A.M. Beese, Acta Mater. **87**, 309–320 (2015)
33. L. Johnson, M. Mahmoudi, B. Zhang, R. Seede, X.Q. Huang, J.T. Maier, H.J. Maier, I. Karaman, A. Elwany, R. Arroyave, Acta Mater. **176**, 199–210 (2019)
34. W. Shifeng, L. Shuai, W. Qingsong, C. Yan, Z. Sheng, S. Yusheng, J. Mater. Process. Technol. **214**, 2660–2667 (2014)
35. J.M. Jeon, J.M. Park, J.-H. Yu, J.G. Kim, Y. Seong, S.H. Park, H.S. Kim, Mater. Sci. Eng. A **763**, 138152 (2019)
36. G.P. Dinda, A.K. Dasgupta, J. Mazumder, Surf. Coat. Technol. **206**, 2152–2160 (2012)
37. H. Zhang, H.H. Zhu, T. Qi, Z.H. Hu, X.Y. Zeng, Mater. Sci. Eng. A **656**, 47–54 (2016)
38. L. Thijs, K. Kempen, J.P. Kruth, J. Van Humbeeck, Acta Mater. **61**, 1809–1819 (2013)
39. J.J.S. Dilip, S. Zhang, C. Teng, K. Zeng, C. Robinson, D. Pal, B. Stucker, Prog. Addit. Manuf. **2**, 157–167 (2017)
40. X.P. Li, X.J. Wang, M. Saunders, A. Suvorova, L.C. Zhang, Y.J. Liu, M.H. Fang, Z.H. Huang, T.B. Sercombe, Acta Mater. **95**, 74–82 (2015)
41. G.P. Dinda, A.K. Dasgupta, S. Bhattacharya, H. Natu, B. Dutta, J. Mazumder, Metall. Mater. Trans. A **44**, 2233–2242 (2013)
42. J.D. Majumdar, A. Pinkerton, Z. Liu, I. Manna, L. Li, Appl. Surf. Sci. **247**, 320–327 (2005)
43. J.J.S. Dilip, G.D.J. Ram, T.L. Starr, B. Stucker, Addit. Manuf. **13**, 49–60 (2017)
44. Z.H. Xiong, S.L. Liu, S.F. Li, Y. Shi, Y.F. Yang, R.D.K. Misra, Mater. Sci. Eng. A **740**, 148–156 (2019)
45. F. Kies, P. Kohnen, M.B. Wilms, F. Brasche, K.G. Pradeep, A. Schwedt, S. Richter, A. Weisheit, J.H. Schleifenbaum, C. Haase, Mater. Des. **160**, 1250–1264 (2018)
46. L. Thijs, F. Verhaeghe, T. Craeghs, J.V. Humbeeck, J.-P. Kruth, Acta Mater. **58**, 3303–3312 (2010)
47. H. Qi, M. Azer, A. Ritter, Metall. Mater. Trans. A **40**, 2410–2422 (2009)
48. X. Zhao, B. Song, Y.J. Zhang, X.M. Zhu, Q.S. Wei, Y.S. Shi, Mater. Sci. Eng. A **647**, 58–61 (2015)
49. E. Brandl, A. Schoberth, C. Leyens, Mater. Sci. Eng. A **532**, 295–307 (2012)
50. G.S. Sankar, G.M. Karthik, A. Mohammad, R. Kumar, G.D. Janaki Ram, Trans. Indian Inst. Met. **72**, 35–46 (2018)
51. S.H. Sun, T. Ishimoto, K. Hagihara, Y. Tsutsumi, T. Hanawa, T. Nakano, Scr. Mater. **159**, 89–93 (2019)
52. H.L. Wei, J.W. Elmer, T. DebRoy, Acta Mater. **115**, 123–131 (2016)
53. T.G. Holesinger, J.S. Carpenter, T.J. Lienert, B.M. Patterson, P.A. Papin, H. Swenson, N.L. Cordes, JOM **68**, 1000–1011 (2016)
54. T. DebRoy, H.L. Wei, J.S. Zuback, T. Mukherjee, J.W. Elmer, J.O. Milewski, A.M. Beese, A. Wilson-Heid, A. De, W. Zhang, Prog. Mater Sci. **92**, 112–224 (2018)
55. M. Tang, P.C. Pistorius, J.L. Beuth, Addit. Manuf. **14**, 39–48 (2017)
56. A. Yadollahi, N. Shamsaei, S.M. Thompson, D.W. Seely, Mater. Sci. Eng. A **644**, 171–183 (2015)
57. S. Kou, *Welding Metallurgy* (Wiley, Hoboken, 2003).
58. J.C. Lippold, *Welding Metallurgy and Weldability* (Wiley Online Library, Hoboken, 2015).
59. S.A. David, J.M. Vitek, Int. Mater. Rev. **34**, 213–245 (1989)
60. A.A. Antonysamy, J. Meyer, P.B. Prangnell, Mater. Charact. **84**, 153–168 (2013)
61. M. Gäumann, C. Bezençon, P. Canalis, W. Kurz, Acta Mater. **49**, 1051–1062 (2001)
62. P.W. Liu, Z. Wang, Y.H. Xiao, M.F. Horstemeyer, X.Y. Cui, L. Chen, Addit. Manuf. **26**, 22–29 (2019)
63. V. Manvatkar, A. De, T. DebRoy, Mater. Sci. Technol. **31**, 924–930 (2015)

64. L.L. Parimi, G.A. Ravi, D. Clark, M.M. Attallah, Mater. Charact. **89**, 102–111 (2014)
65. T. Wang, Y.Y. Zhu, S.Q. Zhang, H.B. Tang, H.M. Wang, J. Alloy. Compd. **632**, 505–513 (2015)
66. R.J. Moat, A.J. Pinkerton, L. Li, P.J. Withers, M. Preuss, Acta Mater. **57**, 1220–1229 (2009)
67. B. Gwalani, V. Soni, O.A. Waseem, S.A. Mantri, R. Banerjee, Opt. Laser Technol. **113**, 330–337 (2019)
68. L. Thivillon, P. Bertrand, B. Laget, I. Smurov, J. Nucl. Mater. **385**, 236–241 (2009)
69. G.P. Dinda, A.K. Dasgupta, J. Mazumder, Mater. Sci. Eng. A **509**, 98–104 (2009)
70. G.P. Dinda, A.K. Dasgupta, J. Mazumder, Scr. Mater. **67**, 503–506 (2012)
71. M. Garibaldi, I. Ashcroft, M. Simonelli, R. Hague, Acta Mater. **110**, 207–216 (2016)
72. H.L. Wei, H.K.D.H. Bhadeshia, S.A. David, T. DebRoy, Sci. Technol. Weld. Join. **24**, 361–366 (2019)
73. H.L. Wei, J. Mazumder, T. DebRoy, Sci. Rep. **5**, 16446 (2015)
74. J. Akram, P. Chalavadi, D. Pal, B. Stucker, Addit. Manuf. **21**, 255–268 (2018)
75. T. Qi, H.H. Zhu, H. Zhang, J. Yin, L.D. Ke, X.Y. Zeng, Mater. Des. **135**, 257–266 (2017)
76. Z.J. Sun, X.P. Tan, S.B. Tor, C.K. Chua, NPG Asia Mater. **10**, 127–136 (2018)
77. A.M. Beese, B.E. Carroll, JOM **68**, 724–734 (2016)
78. S.S. Al-Bermani, M.L. Blackmore, W. Zhang, I. Todd, Metall. Mater. Trans. A **41**, 3422–3434 (2010)
79. X.P. Tan, S. Chandra, Y. Kok, S.B. Tor, G. Seet, N.H. Loh, E. Liu, Materialia **7**, 100365 (2019)
80. T. Fujieda, M.C. Chen, H. Shiratori, K. Kuwabara, K. Yamanaka, Y. Koizumi, A. Chiba, S. Watanabe, Addit. Manuf. **25**, 412–420 (2019)
81. I. Kunce, M. Polanski, K. Karczewski, T. Plocinski, K.J. Kurzydlowski, J. Alloy. Compd. **648**, 751–758 (2015)
82. Z.Q. Wang, T.A. Palmer, A.M. Beese, Acta Mater. **110**, 226–235 (2016)
83. T.R. Smith, J.D. Sugar, C.S. Marchi, J.M. Schoenung, Acta Mater. **164**, 728–740 (2019)
84. M.L. Montero-Sistiaga, R. Mertens, B. Vrancken, X. Wang, B. Van Hooreweder, J.-P. Kruth, J. Van Humbeeck, J. Mater. Process. Technol. **238**, 437–445 (2016)
85. H. Zhang, H.H. Zhu, X.J. Nie, J. Yin, Z.H. Hu, X.Y. Zeng, Scr. Mater. **134**, 6–10 (2017)
86. J.H. Martin, B.D. Yahata, J.M. Hundley, J.A. Mayer, T.A. Schaedler, T.M. Pollock, Nature **549**, 365–369 (2017)
87. M. Mukherjee, Materialia **7**, 100359 (2019)
88. S. Bahl, S. Mishra, K.U. Yazar, I.R. Kola, K. Chatterjee, S. Suwas, Addit. Manuf. **28**, 65–77 (2019)
89. Y.M. Wang, T. Voisin, J.T. McKeown, J. Ye, N.P. Calta, Z. Li, Z. Zeng, Y. Zhang, W. Chen, T.T. Roehling, R.T. Ott, M.K. Santala, P.J. Depond, M.J. Matthews, A.V. Hamza, T. Zhu, Nat. Mater. **17**, 63–71 (2018)
90. Y. Zhong, L.F. Liu, S. Wikman, D.Q. Cui, Z.J. Shen, J. Nucl. Mater. **470**, 170–178 (2016)
91. C. Qiu, M.A. Kindi, A.S. Aladawi, I.A. Hatmi, Sci. Rep. **8**, 7785 (2018)
92. K.G. Prashanth, J. Eckert, J. Alloy. Compd. **707**, 27–34 (2017)
93. A.J. Birnbaum, J.C. Steuben, E.J. Barrick, A.P. Iliopoulos, J.G. Michopoulos, Addit. Manuf. **29**, 100784 (2019)
94. G. Wang, H. Ouyang, C. Fan, Q. Guo, Z.Q. Li, W.T. Yan, Z. Li, Mater. Res. Lett. **8**, 283–290 (2020)
95. L.E. Murr, E.V. Esquivel, S.A. Quinones, S.M. Gaytan, M.I. Lopez, E.Y. Martinez, F. Medina, D.H. Hernandez, E. Martinez, J.L. Martinez, S.W. Stafford, D.K. Brown, T. Hoppe, W. Meyers, U. Lindhe, R.B. Wicker, Mater. Charact. **60**, 96–105 (2009)
96. Y. Zhong, L.E. Rannar, S. Wikaman, A. Koptyug, L.F. Liu, D.Q. Cui, Z.J. Shen, Fusion Eng. Des. **116**, 24–33 (2017)
97. Y. Zhong, L.E. Rannar, L.F. Liu, A. Koptyug, S. Wikman, J. Olsen, D.Q. Cui, Z.J. Shen, J. Nucl. Mater. **486**, 234–245 (2017)
98. H.Y. Wan, Z.J. Zhou, C.P. Li, G.F. Chen, G.P. Zhang, J. Mater. Sci. Technol. **34**, 1799–1804 (2018)
99. P. Tao, H.X. Li, B.Y. Huang, Q.D. Hu, S.L. Gong, Q.Y. Xu, Vacuum **159**, 382–390 (2019)
100. Y.T. Zhu, J.Y. Huang, J. Gubicza, T. Ungar, Y.M. Wang, E. Ma, R.Z. Valiev, J. Mater. Res. **18**, 1908–1917 (2003)
101. W. Kurz, D.J. Fisher, *Fundamentals of Solidification* (Trans Tech Publications, Stafa-Zurich, 1984).
102. W. Xu, E.W. Lui, A. Pateras, M. Qian, M. Brandt, Acta Mater. **125**, 390–400 (2017)
103. F.S.H.B. Freeman, J. Sharp, J.W. Xi, I. Todd, Addit. Manuf. **30**, 100917 (2019)
104. V.D. Divya, R. Munoz-Moreno, O.M.D.M. Messe, J.S. Barnard, S. Baker, T. Illston, H.J. Stone, Mater. Charact. **114**, 62–74 (2016)
105. K. Saeidi, X. Gao, F. Lofaj, L. Kvetkova, Z.J. Shen, J. Alloy. Compd. **633**, 463–469 (2015)
106. D. Wang, C.H. Song, Y.Q. Yang, Y.C. Bai, Mater. Des. **100**, 291–299 (2016)
107. K. Saeidi, X. Gao, Y. Zhong, Z.J. Shen, Mater. Sci. Eng. A **625**, 221–229 (2015)
108. R.V. Mises, Bull. Am. Math. Soc. **51**, 555–562 (1945)
109. Z.G. Zhu, Q.B. Nguyen, F.L. Ng, X.H. An, X.Z. Liao, P.K. Liaw, S.M.L. Nai, J. Wei, Scr. Mater. **154**, 20–24 (2018)
110. J. Wu, X.Q. Wang, W. Wang, M.M. Attallah, M.H. Loretto, Acta Mater. **117**, 311–320 (2016)
111. U.F. Kocks, H. Mecking, Prog. Mater Sci. **48**, 171–273 (2003)
112. L.P. Kubin, A. Mortensen, Scr. Mater. **48**, 119–125 (2003)
113. P.A. Hooper, Addit. Manuf. **22**, 548–559 (2018)
114. T. Maeshima, K. Oh-Ishi, Heliyon **5**, 01186 (2019)
115. P. Kürnsteiner, P. Bajaj, A. Gupta, M.B. Wilms, A. Weisheit, X. Li, C. Leinenbach, B. Gault, E.A. Jägle, D. Raabe, Addit. Manuf. **32**, 100910 (2020)
116. M. Roudnická, O. Molnárová, D. Dvorský, L. Křivský, D. Vojtěch, Met. Mater. Int. **26**, 1168–1181 (2020)
117. A.R. Kini, *Laser Additive Manufacturing of Oxide Dispersion Strengthened Steels and Cu–Cr–Nb Alloys* (RWTH Aachen, Aachen, 2019).
118. E.A. Jägle, Z. Sheng, L. Wu, L. Lu, J. Risse, A. Weisheit, D. Raabe, JOM **68**, 943–949 (2016)
119. A.P. Ventura, C.J. Marvel, G. Pawlikowski, M. Bayes, M. Watanabe, R.P. Vinci, W.Z. Misiolek, Metall. Mater. Trans. A **48**, 6070–6082 (2017)
120. S. Uchida, T. Kimura, T. Nakamoto, T. Ozaki, T. Miki, M. Takemura, Y. Oka, R. Tsubota, Mater. Des. **175**, 107815 (2019)
121. J.B. Wang, X.L. Zhou, J.H. Li, M. Brochu, Y.F. Zhao, Addit. Manuf. **31**, 100921 (2020)
122. C. Haase, J. Bultmann, J. Hof, S. Ziegler, S. Bremen, C. Hinke, A. Schwedt, U. Prahl, W. Bleck, Materials (Basel) **10**, 56 (2017)
123. T. Debroy, S.A. David, Rev. Mod. Phys. **67**, 85–112 (1995)
124. V. Juechter, T. Scharowsky, R.F. Singer, C. Korner, Acta Mater. **76**, 252–258 (2014)
125. L.E. Murr, E. Martinez, J. Hernandez, S. Collins, K.N. Amato, S.M. Gaytan, P.W. Shindo, J. Mater. Res. Technol. **1**, 167–177 (2012)
126. J.W. Cahn, Acta Metall. **11**, 1275–1282 (1963)
127. K. Davidson, S. Singamneni, Mater. Manuf. Process. **31**, 1543–1555 (2016)
128. X. Zhao, Q.S. Wei, B. Song, Y. Liu, X.W. Luo, S.F. Wen, Y.S. Shi, Mater. Manuf. Process. **30**, 1283–1289 (2015)
129. E.A. Jägle, Z. Sheng, P. Kürnsteiner, S. Ocylok, A. Weisheit, D. Raabe, Materials **10**, 8 (2017)

130. M.J. Holzweissig, A. Taube, F. Brenne, M. Schaper, T. Niendorf, Metall. Mater. Trans. B **46**, 545–549 (2015)
131. J. Krell, A. Rottger, K. Geenen, W. Theisen, J. Mater. Process. Technol. **255**, 679–688 (2018)
132. P. Kürnsteiner, M.B. Wilms, A. Weisheit, P. Barriobero-Vila, E.A. Jägle, D. Raabe, Acta Mater. **129**, 52–60 (2017)
133. L. Facchini, N. Vicente, I. Lonardelli, E. Magalini, P. Robotti, A. Molinari, Adv. Eng. Mater. **12**, 184–188 (2010)
134. T. LeBrun, T. Nakamoto, K. Horikawa, H. Kobayashi, Mater. Des. **81**, 44–53 (2015)
135. P. Bajaj, A. Hariharan, A. Kini, P. Kurnsteiner, D. Raabe, E.A. Jagle, Mater. Sci. Eng. A **772**, 138633 (2020)
136. P. Krakhmalev, I. Yadroitsava, G. Fredriksson, I. Yadroitsev, Mater. Des. **87**, 380–385 (2015)
137. F. Deirmina, N. Peghini, B. AlMangour, D. Grzesiak, M. Pellizzari, Mater. Sci. Eng. A **753**, 109–121 (2019)
138. R. Casati, M. Coduri, N. Lecis, C. Andrianopoli, M. Vedani, Mater. Charact. **137**, 50–57 (2018)
139. H.J. Niu, I.T.H. Chang, Scr. Mater. **41**, 25–30 (1999)
140. E.A. Jägle, P.-P. Choi, J. Van Humbeeck, D. Raabe, J. Mater. Res. **29**, 2072 (2014)
141. R. Mertens, B. Vrancken, N. Holmstock, Y. Kinds, J.P. Kruth, J. Van Humbeeck, Phys. Procedia **83**, 882–890 (2016)
142. M. Åsberg, G. Fredriksson, S. Hatami, W. Fredriksson, P. Krakhmalev, Mater. Sci. Eng. A **742**, 584–589 (2019)
143. R.D. Li, P.D. Niu, T.C. Yuan, P. Cao, C. Chen, K.C. Zhou, J. Alloy. Compd. **746**, 125–134 (2018)
144. Y.K. Kim, J. Cho, K.A. Lee, J. Alloy. Compd. **805**, 680–691 (2019)
145. P. Wang, P.F. Huang, F.L. Ng, W.J. Sin, S.L. Lu, M.L.S.R. Nai, Z.L. Dong, J. Wei, Mater. Des. **168**, 107576 (2019)
146. Y. Brif, M. Thomas, I. Todd, Scr. Mater. **99**, 93–96 (2015)
147. R. Zhou, Y. Liu, C.S. Zhou, S.Q. Li, W.Q. Wu, M. Song, B. Liu, X.P. Liang, P.K. Liaw, Intermetallics **94**, 165–171 (2018)
148. J.M. Park, J. Choe, J.G. Kim, J.W. Bae, J. Moon, S. Yang, K.T. Kim, J.-H. Yu, H.S. Kim, Mater. Res. Lett. **8**, 1–7 (2020)
149. D. Karlsson, A. Marshal, F. Johansson, M. Schuisky, M. Sahlberg, J.M. Schneider, U. Jansson, J. Alloy. Compd. **784**, 195–203 (2019)
150. P.D. Niu, R.D. Li, T.C. Yuan, S.Y. Zhu, C. Chen, M.B. Wang, L. Huang, Intermetallics **104**, 24–32 (2019)
151. H. Shiratori, T. Fujieda, K. Yamanaka, Y. Koizumi, K. Kuwabara, T. Kato, A. Chiba, Mater. Sci. Eng. A **656**, 39–46 (2016)
152. H. Zhang, W. Xu, Y.J. Xu, Z.L. Lu, D.C. Li, Int. J. Adv. Manuf. Technol. **96**, 461–474 (2018)
153. Z. Sun, X.P. Tan, M. Descoins, D. Mangelinck, S.B. Tor, C.S. Lim, Scr. Mater. **168**, 129–133 (2019)
154. I. Kunce, M. Polanski, J. Bystrzycki, Int. J. Hydrog. Energy **39**, 9904–9910 (2014)
155. C. Leyens, M. Peters, *Titanium and Titanium Alloys: Fundamentals and Applications* (Wiley, Hoboken, 2003).
156. S.M. Kelly, S.L. Kampe, Metall. Mater. Trans. A **35**, 1861–1867 (2004)
157. C.L. Qiu, N.J.E. Adkins, M.M. Attallah, Mater. Sci. Eng. A **578**, 230–239 (2013)
158. X.P. Tan, Y.H. Kok, Y.J. Tan, M. Descoins, D. Mangelinck, S.B. Tor, K.F. Leong, C.K. Chua, Acta Mater. **97**, 1–16 (2015)
159. L.E. Murr, S.M. Gaytan, D.A. Ramirez, E. Martinez, J. Hernandez, K.N. Amato, P.W. Shindo, F.R. Medina, R.B. Wicker, J. Mater. Sci. Technol. **28**, 1–14 (2012)
160. Y.J. Liu, S.J. Li, W.T. Hou, S.G. Wang, Y.L. Hao, R. Yang, T.B. Sercombe, L.C. Zhang, J. Mater. Sci. Technol. **32**, 505–508 (2016)
161. L.C. Zhang, D. Klemm, J. Eckert, Y.L. Hao, T.B. Sercombe, Scr. Mater. **65**, 21–24 (2011)
162. B. Vrancken, L. Thijs, J.P. Kruth, J. Van Humbeeck, Acta Mater. **68**, 150–158 (2014)
163. H.-J. Yi, J.-W. Kim, Y.-L. Kim, S. Shin, Met. Mater. Int. **26**, 1235–1246 (2020)
164. T. Bhardwaj, M. Shukla, N.K. Prasad, C. Paul, K. Bindra, Met. Mater. Int. **26**, 1015–1029 (2020)
165. Y. Byun, S. Lee, S.-M. Seo, J.-T. Yeom, S.E. Kim, N. Kang, J. Hong, Met. Mater. Int. **24**, 1213–1220 (2018)
166. F. Arias-González, J. del Val, R. Comesaña, J. Penide, F. Lusquiños, F. Quintero, A. Riveiro, M. Boutinguiza, F.J. Gil, J. Pou, Met. Mater. Int. **24**, 231–239 (2018)
167. G. Suprobo, A.A. Ammar, N. Park, E.R. Baek, S. Kim, Met. Mater. Int. **25**, 1428–1435 (2019)
168. J.-B. Lee, D.-I. Seo, H.Y. Chang, Met. Mater. Int. **26**, 39–45 (2020)
169. D.D. Gu, Y.C. Hagedorn, W. Meiners, G.B. Meng, R.J.S. Batista, K. Wissenbach, R. Poprawe, Acta Mater. **60**, 3849–3860 (2012)
170. W. Xu, M. Brandt, S. Sun, J. Elambasseril, Q. Liu, K. Latham, K. Xia, M. Qian, Acta Mater. **85**, 74–84 (2015)
171. K.G. Prashanth, S. Scudino, H.J. Klauss, K.B. Surreddi, L. Löber, Z. Wang, A.K. Chaubey, U. Kühn, J. Eckert, Mater. Sci. Eng. A **590**, 153–160 (2014)
172. G. Karthik, P. Mastanaiah, G.J. Ram, R.S. Kottada, Metall. Mater. Trans. B **48**, 1416–1422 (2017)
173. G. Karthik, G.J. Ram, R.S. Kottada, Metall. Mater. Trans. B **48**, 1158–1173 (2017)
174. D.R. Manca, A.Y. Churyumov, A.V. Pozdniakov, A.S. Prosviryakov, D.K. Ryabov, A.Y. Krokhin, V.A. Korolev, D.K. Daubarayte, Met. Mater. Int. **25**, 633–640 (2019)
175. N.T. Aboulkhair, M. Simonelli, L. Parry, I. Ashcroft, C. Tuck, R. Hague, Prog. Mater. Sci. **106**, 100578 (2019)
176. X.J. Wang, L.C. Zhang, M.H. Fang, T.B. Sercombe, Mater. Sci. Eng. A **597**, 370–375 (2014)
177. N. Takata, H. Kodaira, A. Suzuki, M. Kobashi, Mater. Charact. **143**, 18–26 (2018)
178. A.B. Spierings, K. Dawson, T. Heeling, P.J. Uggowitzer, R. Schaublin, F. Palm, K. Wegener, Mater. Des. **115**, 52–63 (2017)
179. P. Deng, M. Karadge, R.B. Rebak, V.K. Gupta, B.C. Prorok, X. Lou, Addit. Manuf. **35**, 101334 (2020)
180. D.A. Ramirez, L.E. Murr, E. Martinez, D.H. Hernandez, J.L. Martinez, B.I. Machado, F. Medina, P. Frigola, R.B. Wicker, Acta Mater. **59**, 4088–4099 (2011)
181. R.D. Li, Y.S. Shi, Z.G. Wang, L. Wang, J.H. Liu, W. Jiang, Appl. Surf. Sci. **256**, 4350–4356 (2010)
182. X.Y. Lou, P.L. Andresen, R.B. Rebak, J. Nucl. Mater. **499**, 182–190 (2018)
183. F.Y. Yan, W. Xiong, E. Faierson, G.B. Olson, Scr. Mater. **155**, 104–108 (2018)
184. S. Bodziak, K.S. Al-Rubaie, L. Dalla Valentina, F.H. Lafratta, E.C. Santos, A.M. Zanatta, Y.M. Chen, Mater. Charact. **151**, 73–83 (2019)
185. C.L. Qiu, J. Alloy. Compd. **790**, 1023–1033 (2019)
186. A. Simchi, Metall. Mater. Trans. B **35**, 937–948 (2004)
187. M. Marya, V. Singh, S. Marya, J.Y. Hascoet, Metall. Mater. Trans. B **46**, 1654–1665 (2015)
188. F.J. Barbaro, P. Krauklis, K.E. Easterling, Mater. Sci. Technol. **5**, 1057–1068 (1989)
189. M. Yan, W. Xu, M.S. Dargusch, H.P. Tang, M. Brandt, M. Qian, Powder Metall. **57**, 251–257 (2014)
190. K. Saeidi, L. Kvetkova, F. Lofajc, Z.J. Shen, RSC Adv. **5**, 20747–20750 (2015)
191. P. Krakhmalev, G. Fredriksson, K. Svensson, I. Yadroitsev, I. Yadroitsava, M. Thuvander, R. Peng, Metals **8**, 1–18 (2018)
192. J. Liu, R.L. Davidchack, H.B. Dong, Comput. Mater. Sci. **74**, 92–100 (2013)

193. X. Zhou, K.L. Li, D.D. Zhang, X.H. Liu, J. Ma, W. Liu, Z.J. Shen, J. Alloy. Compd. **631**, 153–164 (2015)
194. T. Niendorf, S. Leuders, A. Riemer, H.A. Richard, T. Troster, D. Schwarze, Metall. Mater. Trans. B **44**, 794–796 (2013)
195. K.V. Yang, Y.J. Shi, F. Palm, X.H. Wu, P. Rometsch, Scr. Mater. **145**, 113–117 (2018)
196. S.A. Mantri, T. Alam, D. Choudhuri, C.J. Yannetta, C.V. Mikler, P.C. Collins, R. Banerjee, J. Mater. Sci. **52**, 12455–12466 (2017)
197. D. Zhang, D. Qiu, M.A. Gibson, Y. Zheng, H.L. Fraser, D.H. StJohn, M.A. Easton, Nature **576**, 91–95 (2019)
198. N. Takata, R. Nishida, A. Suzuki, M. Kobashi, M. Kato, Metals **8**, 440 (2018)
199. C.L. Tan, K.S. Zhou, M. Kuang, W.Y. Ma, T.C. Kuang, Sci. Technol. Adv. Mater. **19**, 746–758 (2018)
200. B. Ren, D.H. Lu, R. Zhou, Z.H. Li, J.R. Guan, J. Mater. Res. **34**, 1415–1425 (2019)
201. A. Piglione, B. Dovgyy, C. Liu, C.M. Gourlay, P.A. Hooper, M.S. Pham, Mater. Lett. **224**, 22–25 (2018)
202. N. Takata, H. Kodaira, K. Sekizawa, A. Suzuki, M. Kobashi, Mater. Sci. Eng. A **704**, 218–228 (2017)
203. C. Li, Z. Y. Liu, X.Y. Fang, Y.B. Guo, Procedia CIRP **71**, 348–353 (2018)
204. I. Yadroitsev, I. Yadroitsava, Virtual Phys. Prototyp. **10**, 67–76 (2015)
205. R. Martukanitz, P. Michaleris, T. Palmer, T. DebRoy, Z.-K. Liu, R. Otis, T.W. Heo, L.-Q. Chen, Addit. Manuf. **1–4**, 52–63 (2014)
206. Z.C. Fang, Z.L. Wu, C.G. Huang, C.W. Wu, Opt. Laser Technol. **129**, 106283 (2020)
207. P.J. Withers, H.K.D.H. Bhadeshia, Mater. Sci. Technol. **17**, 355–365 (2001)
208. P. Mercelis, J.P. Kruth, Rapid Prototyp. J. **12**, 254–265 (2006)
209. C. Casavola, S.L. Carnpanelli, C. Pappalettere, J. Strain Anal. Eng. **44**, 93–104 (2009)
210. B. Ahmad, S.O. van der Veen, M.E. Fitzpatrick, H. Guo, Addit. Manuf. **22**, 571–582 (2018)
211. A.S. Wu, D.W. Brown, M. Kumar, G.F. Gallegos, W.E. King, Metall. Mater. Trans. A **45**, 6260–6270 (2014)
212. Y.J. Lu, S.Q. Wu, Y.L. Gan, T.T. Huang, C.G. Yang, J.J. Lin, J.X. Lin, Opt. Laser Technol. **75**, 197–206 (2015)
213. T. Mishurova, K. Artzt, J. Haubrich, G. Requena, G. Bruno, Addit. Manuf. **25**, 325–334 (2019)
214. J. Cao, F.C. Liu, X. Lin, C.P. Huang, J. Chen, W.D. Huang, Opt. Laser Technol. **45**, 228–235 (2013)
215. Y. Liu, Y.Q. Yang, D. Wang, Int. J. Adv. Manuf. Technol. **87**, 647–656 (2016)
216. M.L. Griffith, M.E. Schlienger, L.D. Harwell, M.S. Oliver, M.D. Baldwin, M.T. Ensz, M. Essien, J. Brooks, C.V. Robino, J.E. Smugeresky, W.H. Hofmeister, M.J. Wert, D.V. Nelson, Mater. Des. **20**, 107–113 (1999)
217. M. Maly, C. Holler, M. Skalon, B. Meier, D. Koutny, R. Pichler, C. Sommitsch, D. Palousek, Materials (Basel) **12**, 930 (2019)
218. H. Ali, L. Ma, H. Ghadbeigi, K. Mumtaz, Mater. Sci. Eng. A **695**, 211–220 (2017)
219. L.M. Sochalski-Kolbus, E.A. Payzant, P.A. Cornwell, T.R. Watkins, S.S. Babu, R.R. Dehoff, M. Lorenz, O. Ovchinnikova, C. Duty, Metall. Mater. Trans. A **46**, 1419–1432 (2015)
220. D. Buchbinder, W. Meiners, N. Pirch, K. Wissenbach, J. Schrage, J. Laser Appl. **26**, 012004 (2014)
221. R. Mertens, S. Dadbakhsh, J. Van Humbeeck, J.P. Kruth, *10th Cirp Conference on Photonic Technologies*, vol. 74, pp. 5–11 (2018)
222. N. Kalentics, E. Boillat, P. Peyre, S. Ciric-Kostic, N. Bogojevic, R.E. Loge, Addit. Manuf. **16**, 90–97 (2017)
223. X.D. Xing, X.M. Duan, T.T. Jiang, J.D. Wang, F.C. Jiang, Metals **9**, 103 (2019)
224. A. Takaichi, Suyalatu, T. Nakamoto, N. Joko, N. Nomura, Y. Tsutsumi, S. Migita, H. Doi, S. Kurosu, A. Chiba, N. Wakabayashi, Y. Igarashi, T. Hanawa, J. Mech. Behav. Biomed. Mater. **21**, 67–76 (2013)
225. M.W. Wu, P.H. Lai, J.K. Chen, Mater. Sci. Eng. A **650**, 295–299 (2016)
226. B. Song, S.J. Dong, Q. Liu, H.L. Liao, C. Coddet, Mater. Des. **54**, 727–733 (2014)
227. K.N. Amato, S.M. Gaytan, L.E. Murr, E. Martinez, P.W. Shindo, J. Hernandez, S. Collins, F. Medina, Acta Mater. **60**, 2229–2239 (2012)
228. L. Facchini, E. Magalini, P. Robotti, A. Molinari, Rapid Prototyp. J. **15**, 171–178 (2009)
229. A.R. Balachandramurthi, J. Moverare, S. Mahade, R. Pederson, Materials (Basel) **12**, 68 (2018)
230. L.E. Murr, E. Martinez, S.M. Gaytan, D.A. Ramirez, B.I. Machado, P.W. Shindo, J.L. Martinez, F. Medina, J. Wooten, D. Ciscel, U. Ackelid, R.B. Wicker, Metall. Mater. Trans. A **42**, 3491–3508 (2011)
231. T.R. Smith, J.D. Sugar, J.M. Schoenung, C. San Marchi, JOM **70**, 358–363 (2018)
232. B. Vrancken, L. Thijs, J.P. Kruth, J. Van Humbeeck, J. Alloy. Compd. **541**, 177–185 (2012)
233. K. Saeidi, S. Alvi, F. Lofaj, V.I. Petkov, F. Akhtar, Metals **9**, 199 (2019)
234. P.L. Blackwell, J. Mater. Process. Technol. **170**, 240–246 (2005)
235. L.N. Carter, M.M. Attallah, R.C. Reed, Superalloys **2012**, 577–586 (2012)
236. B. Mooney, K.I. Kourousis, R. Raghavendra, Addit. Manuf. **25**, 19–31 (2019)
237. A.K. Syed, M. Awd, F. Walther, X. Zhang, Mater. Sci. Technol. **35**, 653–660 (2019)
238. D. Zhang, A. Prasad, M.J. Bermingham, C.J. Todaro, M.J. Benoit, M.N. Patel, D. Qiu, D.H. StJohn, M. Qian, M.A. Easton, Metall. Mater. Trans. A **51**, 4341–4359 (2020)
239. J.W. Lin, F.D. Chen, X.B. Tang, J. Liu, S.K. Shen, G.J. Ge, Vacuum **174**, 109183 (2020)